

Pursuing the Precision Study for Color Glass Condensate in Forward Hadron Productions

Yu Shi,^{1,2,*} Lei Wang,^{2,†} Shu-Yi Wei,^{1,3,‡} and Bo-Wen Xiao^{4,§}

¹*Key Laboratory of Particle Physics and Particle Irradiation (MOE),
Institute of frontier and interdisciplinary science,
Shandong University, Qingdao, Shandong 266237, China*

²*Key Laboratory of Quark and Lepton Physics (MOE) and Institute of Particle Physics,
Central China Normal University, Wuhan 430079, China*

³*European Centre for Theoretical Studies in Nuclear Physics and Related Areas (ECT*) and Fondazione Bruno Kessler,
Strada delle Tabarelle 286, I-38123 Villazzano (TN), Italy*

⁴*School of Science and Engineering, The Chinese University of Hong Kong, Shenzhen 518172, China*

With the tremendous accomplishments of RHIC and the LHC experiments and the advent of the future Electron-Ion Collider on the horizon, the quest for compelling evidence of the color glass condensate (CGC) has become one of the most aspiring goals in the high energy Quantum Chromodynamics research. Pursuing this question requires developing the precision test of the CGC formalism. By systematically implementing the threshold resummation, we significantly improve the stability of the next-to-leading-order calculation in CGC for forward rapidity hadron productions in pp and pA collisions, especially in the high p_T region, and obtain reliable descriptions of all existing data measured at RHIC and the LHC across all p_T regions. Consequently, this technique can pave the way for the precision studies of the CGC next-to-leading-order predictions by confronting them with a large amount of precise data.

Introduction The gluon saturation phenomenon[1–6], predicted by the small- x framework, which is also known as the color glass condensate (CGC) formalism, has been an intriguing forefront research topic. A lot of experimental and theoretical research efforts around the globe have been devoted to this cutting-edge research frontier. Besides, in the upcoming era of the Electron-Ion Collider (EIC)[7–10], probing the emergent properties of ultra-dense gluon has become one of the key fundamental questions that the EIC sets out to address.

CGC is an effective formalism in Quantum Chromodynamics (QCD) which describes the novel non-linear dynamics of low-momentum gluons inside a hadron. These low momentum gluon degrees of freedom are generally referred to as the small- x gluons, with x being the longitudinal momentum fraction. First, color sources such as large- x quarks and gluons inside fast-moving hadrons emit a large number of small- x gluons[11, 12]. In the meantime, when its occupation number inside the hadron becomes sufficiently large, small- x gluons start to overlap, recombine and then compress each other, eventually saturate. Usually, we introduce the saturation momentum $Q_s(x)$ at given x to characterize the typical size of soft gluons. Due to the rise of the gluon density, $Q_s(x)$ increases at low- x so that the corresponding gluon size becomes smaller in the transverse space and more gluons can fit into a confined transverse region. This non-linear dynamics can be captured by the evolution equation known as the BK-JIMWLK equation[13–18].

In high-energy collisions, small- x gluon degrees of freedom are unlocked and measured in terms of final state hadrons. To search for the experimental evidence of gluon saturation among existing data[19–28] and prepare for the future EIC precision studies, it is important to develop next-to-leading order (NLO) computations in the CGC formalism and achieve an accurate description of data collected from various kinematic regions.

Among many different physical processes studied at RHIC and the LHC, the calculation and measurements of the single forward hadron production in proton-nucleus collisions (or deuteron-nucleus collisions at RHIC), $p(d) + A \rightarrow h(y, p_T) + X$, have attracted a great deal of attention[29–49]. In the forward region, the projectile proton (or deuteron) can be viewed as a relatively dilute object that probes the ultra-dense gluon fields in the nuclear target[30, 36, 37, 50, 51]. Experimentally, the evolution of the nuclear modification factor R_{dAu} [19, 20] from mid-rapidity to forward-rapidity regions is considered the evidence[39, 52–55] for the onset of gluon saturation. The measured R_{dAu} is computed from the hadron spectra in deuteron + gold collisions normalized by the spectra in pp collisions times the number of binary collisions, and R_{dAu} in forward rapidity regions is found to be suppressed. The physical interpretation is that the non-linear gluon dynamics can significantly reduce the gluon density at small- x in nuclei compared to the proton (or deuteron) baseline.

In terms of the perturbative expansion, the corresponding cross-section can be schematically cast into

$$\frac{d\sigma}{dyd^2p_T} = \int x_p f_a(x_p) \otimes D_a(z) \otimes \mathcal{F}_a^{xg}(k_\perp) \otimes \mathcal{H}^{(0)} + \frac{\alpha_s}{2\pi} \sum_{a,b=q,g} \int x f_a(x) \otimes D_b(z) \otimes \mathcal{F}_{ab}^{xg} \otimes \mathcal{H}_{ab}^{(1)}, \quad (1)$$

* yu.shi@sdu.edu.cn

† leiwang@mails.ccnuc.edu.cn

‡ shuyi@sdu.edu.cn

§ xiaobowen@cuhk.edu.cn

where the first term stands for the leading order (LO) contribution first computed in Refs. [30, 56] and the second term represents the NLO corrections derived from one-loop diagrams. In our framework, the full NLO contribution includes the contributions computed in Ref. [36, 37] and the additional kinematic constraint corrections given in Ref. [45]. The kinematic variables are defined as follows, $x_p = \frac{k_\perp}{\sqrt{s}}e^y$, $x_g = \frac{k_\perp}{\sqrt{s}}e^{-y}$, $p_T = zk_\perp$ with k_\perp and z being the parton transverse momentum and the longitudinal momentum fraction of produced hadron w.r.t. its original parton, respectively.

The LO production in various channels and the contribution together with running coupling effects have been calculated extensively in Refs. [32, 33, 35, 38, 41, 42, 57–59], and part of the NLO contributions are studied in Refs [34, 56]. To obtain the full analytical expressions of the NLO corrections, one needs to evaluate all of the real and virtual one-loop diagrams and remove various types of divergences, as demonstrated in Ref. [36, 37]. First, we subtract the so-called rapidity divergences and absorb them into the evolution of the dipole scattering amplitude associated with the dipole gluon distribution $\mathcal{F}^{x_g}(k_\perp)$. This procedure reproduces the well-known BK equation[13, 14] and allows us to resum the small- x large logarithms systematically. Second, one can gather all the residual collinear divergences and remove them through the redefinition of collinear parton distribution functions (PDFs) $xf(x)$ or/and fragmentation functions (FFs) $D(z)$. Eventually, the resulting finite NLO corrections, which are simplified in the large N_c limit and denoted as $\mathcal{H}_{ab}^{(1)}$ in Eq. (1), can be numerically evaluated.

The direct evaluation of the complete NLO cross-section yields a good agreement with experimental data[19, 20] from RHIC for forward rapidity hadron production in the low- p_T region. However, the NLO result drastically turns negative in the high p_T region[40]. When the kinematic constraint corrections are included [45], the negative NLO cross-section issue can be slightly mitigated but not entirely resolved. In usual perturbative QCD calculations in the collinear factorization, similar issues occur as well for various processes. It indicates that large (and mostly negative) logarithms hidden in $\mathcal{H}_{ab}^{(1)}$ become important in the high p_T region. In particular, in our case with the forward rapidity hadron production, the threshold logarithms cause the breakdown of the perturbative expansion, and they should be resummed in order to restore the predictive power of our calculation in the region of interest.

The quest for positivity in this NLO CGC calculation has sparked a lot of interest. Over the last seven years, there have been a lot of studies[43–49, 60–65] dedicated to addressing the issue caused by the large negative NLO corrections. We believe that the threshold resummation is one of the feasible solutions to this issue, and the resummation technique developed in this work can also be useful in the study of other NLO calculations[66–75] in CGC. In addition, there have been some further theoret-

ical efforts[76–79], which go beyond the eikonal approximation and compute the next-to-eikonal corrections for this process.

This paper is organized as follows. The following two sections are devoted to implementing the threshold resummation in the CGC framework for forward hadron productions and the corresponding numerical results, respectively. In the end, the conclusion and outlook are provided in Sec. 4. Finally, all the technical details are attached as the appendix.

2. *Implementation of the threshold resummation* To tackle the issue of the large negative corrections at NLO, we need to analytically extend the applicability of the NLO CGC calculation from the low- p_T region to the high- p_T region, thus obtain reliable numerical predictions for measurements at both RHIC and the LHC, and therefore better understand the transition from the ultradense regime to the dilute regime. First, to illustrate the origin of the threshold logarithms in the NLO corrections, let us discuss the appearance of the large NLO corrections that cause the issue in the sufficiently forward rapidity region when $p_T \gg Q_s$ [40, 45]. In fact, this indicates that the issue occurs when hard scatterings dominate in this region, where the corresponding events are approaching the kinematic threshold. Second, we identify and extract the large logarithms in the momentum space where the numerical computation of the NLO correction can be performed more efficiently. In the end, we introduce the resummation scheme, which allows us to take the higher-order large logarithms into account and restore the predictive power of the one-loop calculation for this process in the CGC framework.

To see this clearly and intuitively, let us recall the kinematics at NLO[36, 37] and define the hadron longitudinal momentum fraction $\tau = \frac{p_T}{\sqrt{s}}e^y$, which is equivalent to $\tau = x\xi z$ with ξ being the remaining momentum fraction of a parton after emitting one gluon. In the forward rapidity region ($y > 0$), as the hadron p_T increases, τ starts to approach 1. That is to say that we are approaching the threshold region where x , z , and ξ are all forced to approach 1. In this case, the phase space for the real gluon emission is severely limited since there is not much longitudinal momentum left for the radiation near the threshold. In contrast, there is no constraint imposed on the virtual graphs. As a result, after canceling singularities between real and virtual graphs, large logarithms appear in the NLO corrections. These large threshold logarithms are the culprits that upset the convergence of the α_s expansion in our NLO calculation. Two formulations of the threshold resummation within the CGC framework have been proposed earlier in Ref. [62] and Refs. [64, 65], respectively. In this paper, our study follows closely with the former approach.

Furthermore, let us describe the strategy used in our calculation to extract the above-mentioned threshold logarithms explicitly. Initially, the NLO corrections[36, 37] were derived in the coordinate space where the physics interpretation for gluon saturation is manifest. How-

ever, due to the oscillating behavior of the complex phase factor in the coordinate space expression, it is challenging to evaluate them numerically, especially in the high p_T region. Therefore, we later transform the complete NLO cross-sections, including the kinematic constraint corrections[45] into the momentum space, yielding much better numerical accuracy. In the coordinate space, we can identify two types of logarithms[62, 80]

$$\text{single log: } \ln \frac{k_\perp^2}{\mu_r^2}, \ln \frac{\mu^2}{\mu_r^2}; \quad \text{double log: } \ln^2 \frac{k_\perp^2}{\mu_r^2}, \quad (2)$$

where $\mu_r \equiv c_0/r_\perp$ with r_\perp being the dipole size and $c_0 = 2e^{-\gamma_E}$. After integrating over r_\perp in the coordinate space, these logarithms generate large contributions in the threshold region when k_\perp (or p_T) becomes much larger than typical value of μ_r . Therefore, in the momentum space, we need to introduce an auxiliary semi-hard scale Λ , much larger than the QCD scale Λ_{QCD} , to extract these large logarithms for the resummation purpose. In the momentum space, the single and double logarithmic terms can be correspondingly cast into[45, 81, 82]

$$\text{single log: } \ln \frac{k_\perp^2}{\Lambda^2} + I_1(\Lambda) \quad \text{and} \quad \ln \frac{\mu^2}{\Lambda^2} + I_1(\Lambda), \quad (3)$$

$$\text{double log: } \ln^2 \frac{k_\perp^2}{\Lambda^2} + I_2(\Lambda), \quad (4)$$

where $I_{1,2}(\Lambda)$ represent the residual matching functions. At one-loop order, our results are independent of the choice of the auxiliary scale Λ . The essential steps of the derivations can be found in the supplemental material.

Usually, in the collinear factorization, the threshold logarithms are resummed in terms of the resummation of the ‘‘plus’’ distributions in the Mellin moment space[83–86]. The technique employed in the CGC framework is slightly different since the relevant gluon distribution is transverse momentum dependent. The threshold logarithms in forward hadron productions can be cast into two parts: the soft and the collinear parts. The soft part such as single and double logs of $\ln \frac{k_\perp^2}{\Lambda^2}$, associated with the soft gluon emission, can be resummed by the Sudakov factor $S_{\text{Sud}}(k_\perp, \Lambda)$. As to the collinear part ($\ln \frac{\mu^2}{\Lambda^2}$), there are two similar approaches to deal with the corresponding resummation. The first method is to develop a renormalization group equation (whose solution is $\Delta(\Lambda^2, \mu^2, \omega \equiv \ln 1/\xi)$) in the momentum space to analytically resum logarithms of $\ln \frac{\mu^2}{\Lambda^2}$ combined with the above soft part in the threshold limit with $\xi \rightarrow 1$. This scheme is akin to the method first developed in the pioneering study[87–90] for the deep-inelastic structure function using the soft-collinear effective theory.

Alternatively, since the above collinear logarithms are associated with the DGLAP splitting functions, they can be resummed with the help of the DGLAP evolution of the PDFs and FFs by resetting the factorization scale[62] from μ to the auxiliary scale Λ in the LO resummed terms and then the resummed formula reads

$$\sigma = \int x f_a(x, \Lambda) \otimes D_a(z, \Lambda) \otimes \mathcal{F}_a^{xg}(k_\perp) \otimes \mathcal{H}^{(0)} \otimes e^{-S_{\text{Sud}}}$$

$$+ \frac{\alpha_s}{2\pi} \sum_{a,b=q,g} \int x f_a(x) \otimes D_b(z) \otimes \mathcal{F}_{ab}^{xg} \otimes \mathcal{H}_{ab}^{(1)}(\mu, \Lambda). \quad (5)$$

In fact, this choice of the factorization scale μ for LO cross-section is similar to the conventional practice of setting $\mu = \mu_b$ in the Collins-Soper-Sterman formalism[92]. These two resummation schemes are theoretically equivalent, and they yield similar numerical results. The resummation scheme is not unique, and one can certainly develop a similar scheme in the coordinate space as well.

Let us compare the resummed formulas as in Eq (5) to the original NLO results in Eq. (1). Essentially, we take out the logarithmic term hidden in $\mathcal{H}_{ab}^{(1)}$ from Eq. (1), and extract the threshold logarithms which are resummed in Eq (5). Then, the terms that are proportional to the residual matching functions $I_{1,2}(\Lambda)$ are put back into the new NLO coefficient $\mathcal{H}_{ab}^{(1)}(\mu, \Lambda)$. Initially, Eq. (1) only depends on the factorization scale μ . After the implementation of the threshold resummation, Eq (5) now depends on the choice of the factorization scale μ and the auxiliary scale Λ . Both scale dependences cancel to the one-loop order (NLO), and the residual scale dependences, which start from the two-loop order in this process, are due to the truncation of the perturbative expansions.

In principle, the cross-section would be independent of both μ and Λ if all-order results were included. In practice, we can estimate the size of higher-order corrections by varying these two scales. Furthermore, to minimize the higher-order corrections, the ‘‘natural’’ choice of these two scales should be adopted. In the collinear part, the hard scale Q ($\sim 2k_\perp$ when k_\perp is sufficiently large) sets the scale for the factorization scale μ . As to the semi-hard auxiliary scale Λ , the ‘‘natural’’ choice should be $\mu_r = c_0/r_\perp$, which depends on the typical value of r_\perp when r_\perp is integrated over. Following Refs. [91–93], we use the saddle point approximation to locate the dominant region of the r_\perp integral, thus estimate the physical value of Λ via the running coupling prescription

$$\Lambda^2 \approx \max \left\{ \Lambda_{\text{QCD}}^2 \left[\frac{(1-\xi)k_\perp^2}{\Lambda_{\text{QCD}}^2} \right]^{\frac{C_R}{C_R + N_c \beta_0}}, Q_s^2 \right\}, \quad (6)$$

where $\beta_0 = \frac{11}{12} - \frac{n_f}{6N_c}$. C_R is the Casimir factor, which gives C_F and C_A for the quark and gluon channel, respectively. In the gluon channel, the saturation momentum Q_s^2 is increased by a factor of N_c/C_F as compared to the quark channel. We set $\Lambda^2 = Q_s^2$ when the saturation effect is strong, while $(1-\xi)k_\perp^2 \sim (1-\tau)p_T^2$ becomes the dynamical scale near the threshold region[89, 90].

3. *Numerical results* In the numerical evaluation, we use the NLO MSTW PDFs [94] and NLO DEHSS FFs [95] together with the one-loop running coupling. For the dipole gluon distribution $\mathcal{F}_a^{xg}(k_\perp)$, we use the modified McLerran-Venugopalan model[4, 5, 96–99] with parameters given by the Set h in Table 1 of Ref. [100] as the initial condition, solve the running-coupling BK equation numerically in the coordinate space[100–109], and then

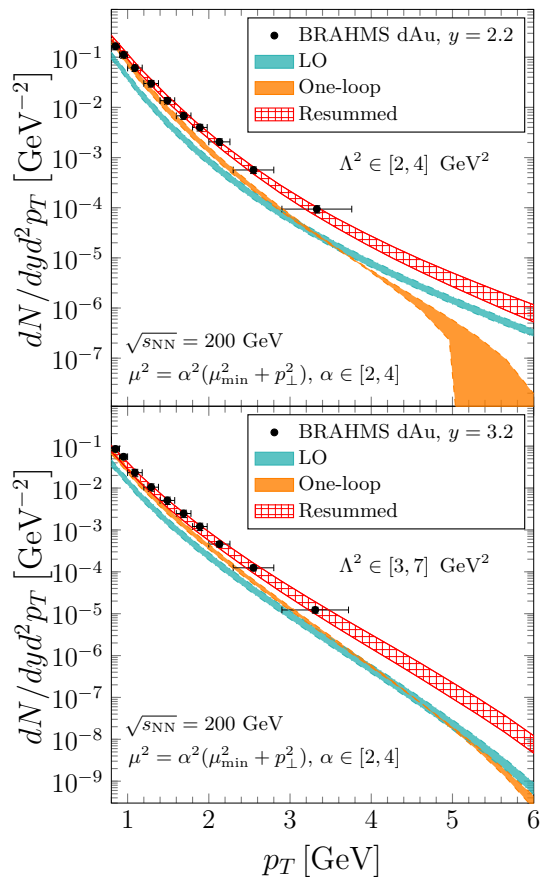


FIG. 1. Theoretical results computed in the CGC framework compared with the BRAHMS data [19]. Many additional plots are provided at the end of the appendix.

obtain the numerical inputs in the momentum space via Fourier transform. As shown in Ref. [41], the numerical results are sensitive to the above inputs especially the initial condition for $\mathcal{F}_a^{xg}(k_\perp)$. To universally describe the data from RHIC and the LHC, it is important to choose proper initial conditions, include the NLO corrections, and implement the threshold resummation near the kinematic threshold.

As shown in Fig. 1, with the proper choices of the Λ^2 scales, the improved NLO CGC calculations with the implementation of the threshold resummation, which are labeled in red gridded bands, agree with the data collected at RHIC and the LHC in both low and high p_T regions. Similar to Ref. [86], the edges of the various bands were computed by varying Λ^2 in the appropriate ranges and $\mu^2 = \alpha^2 (\mu_{\min}^2 + p_T^2)$ with $\alpha = 2 \sim 4$. To ensure that μ^2 is not too small in the low p_T region, a minimum value $\mu_{\min} = 2$ GeV is used. In the high p_T region, the factorization scale is set by the hard scale Q , which is estimated to be at least twice the parton transverse momentum k_T . Therefore, the proper value of μ should be larger than $2p_T$ in this region.

Compared to the one-loop results marked in orange bands, the resummed results, which are depicted in red

grids, are roughly unchanged in the low- p_T region. In fact, when Λ is set to the value around $\mu \sim k_\perp$, the resummation formulation naturally reduces to the one-loop result since the threshold logarithms become small in this limit. Meanwhile, the resummation significantly improves the stability of the NLO calculation for the high- p_T spectrum with the values of the auxiliary scale Λ^2 prescribed by Eq. (6).

In addition, we compare our calculation with the latest data measured by the LHCb collaboration[28] in Fig. 2. In the forward rapidity regions, LHCb measured the prompt charged particle production in pPb and pp collisions at 5 TeV in five rapidity ranges around $y = 2.25, 2.75, 3.25, 3.75$ and 4.2. Within the same framework, we obtain a good agreement with the hadron spectra measured in both pPb and pp collisions for all rapidity windows. The impact of the resummation at the LHCb regime is less pronounced than that at RHIC since the kinematic range of this measurement is still far away from the threshold boundary.

Strictly speaking, our NLO calculation can not be directly applied to forward pp collisions since we assume that the target is much larger than the proton projectile. This assumption allows us to integrate over the impact parameter and obtain the transverse area S_\perp of the target nucleus. For pp collisions, the above assumption is no longer justified, and thus S_\perp^{pp} becomes less under control. Interestingly, we find that our results agree with the hadron spectra measured in pp collisions if we choose $S_\perp^{pp} = 2\pi R_p^2$ with R_p the proton radius.

Eventually, this allows us to calculate the nuclear modification factor, which is defined as

$$R_{pPb} = \frac{1}{A} \frac{d^2\sigma_{pPb}/dp_T dy}{d^2\sigma_{pp}/dp_T dy}. \quad (7)$$

The suppression of this factor R_{pPb} as shown in Fig. 2 reflects the onset of the gluon saturation phenomenon. As we increase the rapidity or decrease the transverse momentum, more suppression in R_{pPb} can be observed as the indication of strengthening of the saturation effect. In the high p_T region, R_{pPb} approaches unity as the saturation effect attenuates.

4. Conclusion By incorporating the threshold resummation in the CGC formalism, we extend the applicability regime of the CGC NLO calculation for forward hadron productions to the large transverse momentum region. Furthermore, the resummation allows us to reliably compute the hadron spectra and corresponding nuclear modification factor from low p_T to high p_T regions, and thus enables us to quantitatively understand the transition from the gluon saturation regime to the dilute regime. This study, which may serve as a benchmark example for other NLO CGC calculations, demonstrates that the NLO phenomenology is essential to test the CGC formalism and collect compelling evidence for the onset of gluon saturation. Lastly, the resummation formulation developed in this paper can also shed light on other higher-order calculations in the CGC framework.

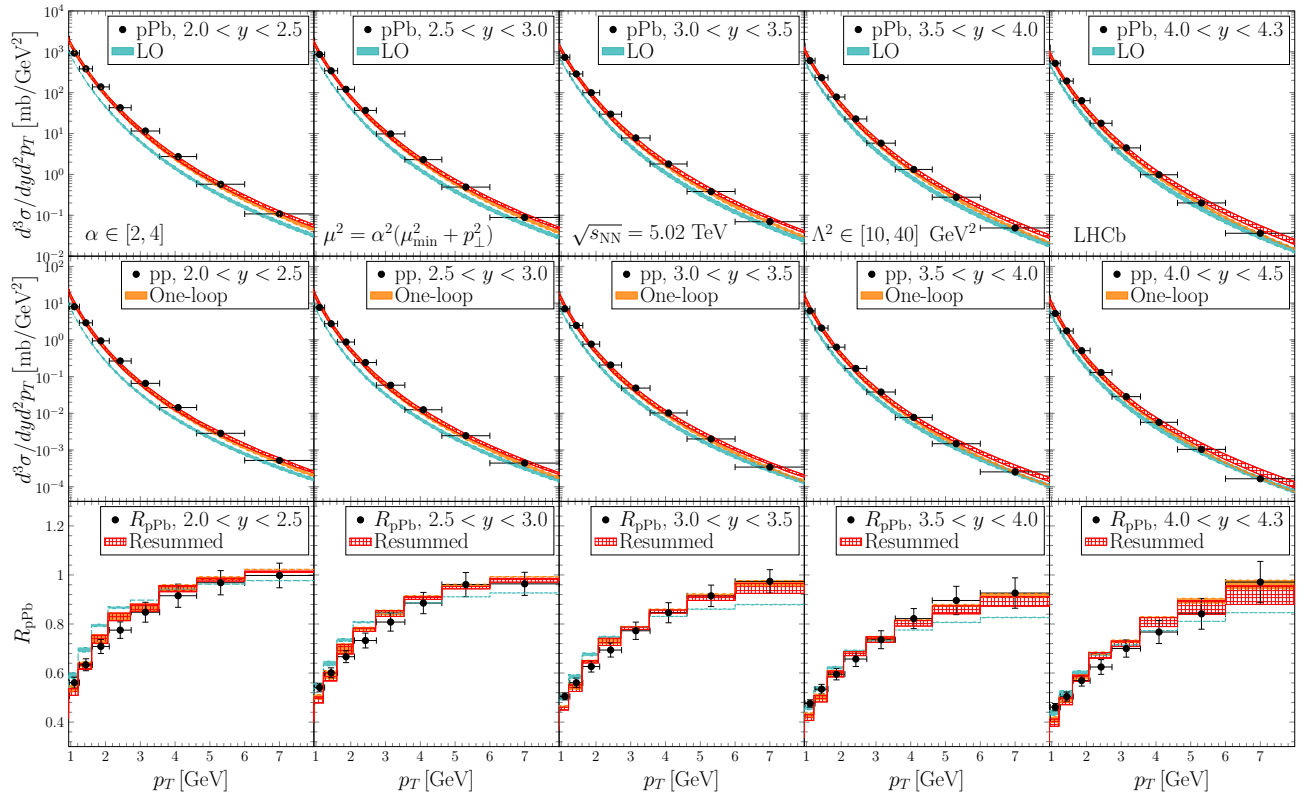


FIG. 2. Comparisons of the pPb , pp and R_{pPb} data[28] from LHCb with CGC calculations in five forward rapidity bins.

Acknowledgments We thank Tuomas Lappi, Xiaohui Liu, Feng Yuan and David Zaslavsky for useful inputs and discussions. This work is partly supported by the Natural Science Foundation of China (NSFC) un-

der Grant Nos. 11575070 and by the university development fund of CUHK-Shenzhen under Grant No. UDF01001859.

-
- [1] L. V. Gribov, E. M. Levin and M. G. Ryskin, Phys. Rept. **100** (1983), 1-150.
- [2] A. H. Mueller and J. w. Qiu, Nucl. Phys. B **268** (1986), 427-452.
- [3] A. H. Mueller, Nucl. Phys. B **335** (1990), 115-137.
- [4] L. D. McLerran and R. Venugopalan, Phys. Rev. D **49** (1994), 2233-2241 [arXiv:hep-ph/9309289 [hep-ph]].
- [5] L. D. McLerran and R. Venugopalan, Phys. Rev. D **49** (1994), 3352-3355 [arXiv:hep-ph/9311205 [hep-ph]].
- [6] F. Gelis, E. Iancu, J. Jalilian-Marian and R. Venugopalan, Ann. Rev. Nucl. Part. Sci. **60** (2010), 463-489 [arXiv:1002.0333 [hep-ph]].
- [7] D. Boer, M. Diehl, R. Milner, R. Venugopalan, W. Vogelsang, D. Kaplan, H. Montgomery, S. Vigdor, A. Accardi and E. C. Aschenauer, *et al.* [arXiv:1108.1713 [nucl-th]].
- [8] A. Accardi, J. L. Albacete, M. Anselmino, N. Armesto, E. C. Aschenauer, A. Bacchetta, D. Boer, W. K. Brooks, T. Burton and N. B. Chang, *et al.* Eur. Phys. J. A **52** (2016) no.9, 268 [arXiv:1212.1701 [nucl-ex]].
- [9] Y. Hatta, Y. V. Kovchegov, C. Marquet, A. Prokudin, E. Aschenauer, H. Avakian, A. Bacchetta, D. Boer, G. A. Chirilli and A. Dumitru, *et al.* [arXiv:2002.12333 [hep-ph]].
- [10] R. Abdul Khalek, A. Accardi, J. Adam, D. Adamiak, W. Akers, M. Albaladejo, A. Al-bataineh, M. G. Alexeev, F. Ameli and P. Antonioli, *et al.* [arXiv:2103.05419 [physics.ins-det]].
- [11] E. A. Kuraev, L. N. Lipatov and V. S. Fadin, Sov. Phys. JETP **45** (1977), 199-204.
- [12] I. I. Balitsky and L. N. Lipatov, Sov. J. Nucl. Phys. **28** (1978), 822-829.
- [13] I. Balitsky, Nucl. Phys. B **463** (1996), 99-160 [arXiv:hep-ph/9509348 [hep-ph]].
- [14] Y. V. Kovchegov, Phys. Rev. D **60** (1999), 034008 [arXiv:hep-ph/9901281 [hep-ph]].
- [15] J. Jalilian-Marian, A. Kovner, A. Leonidov and H. Weigert, Nucl. Phys. B **504** (1997), 415-431 [arXiv:hep-ph/9701284 [hep-ph]].
- [16] J. Jalilian-Marian, A. Kovner, A. Leonidov and H. Weigert, Phys. Rev. D **59** (1998), 014014 [arXiv:hep-ph/9706377 [hep-ph]].
- [17] E. Iancu, A. Leonidov and L. D. McLerran, Nucl. Phys. A **692** (2001), 583-645 [arXiv:hep-ph/0011241 [hep-ph]].

- ph]].
- [18] E. Ferreira, E. Iancu, A. Leonidov and L. McLerran, Nucl. Phys. A **703** (2002), 489-538 [arXiv:hep-ph/0109115 [hep-ph]].
- [19] I. Arsene *et al.* [BRAHMS], Phys. Rev. Lett. **93** (2004), 242303 [arXiv:nucl-ex/0403005 [nucl-ex]].
- [20] J. Adams *et al.* [STAR], Phys. Rev. Lett. **97** (2006), 152302 [arXiv:nucl-ex/0602011 [nucl-ex]].
- [21] E. Braidot [STAR], Nucl. Phys. A **854** (2011), 168-174 [arXiv:1008.3989 [nucl-ex]].
- [22] A. Adare *et al.* [PHENIX], Phys. Rev. Lett. **107** (2011), 172301 [arXiv:1105.5112 [nucl-ex]].
- [23] C. Hadjidakis [ALICE], Nucl. Phys. B Proc. Suppl. **214** (2011), 80-83.
- [24] B. Abelev *et al.* [ALICE], Phys. Rev. Lett. **110** (2013) no.3, 032301 [arXiv:1210.3615 [nucl-ex]].
- [25] B. Abelev *et al.* [ALICE], Phys. Rev. Lett. **110** (2013) no.8, 082302 [arXiv:1210.4520 [nucl-ex]].
- [26] G. Aad *et al.* [ATLAS], Phys. Lett. B **763** (2016), 313-336 [arXiv:1605.06436 [hep-ex]].
- [27] R. Aaij *et al.* [LHCb], [arXiv:2107.10090 [hep-ex]].
- [28] R. Aaij *et al.* [LHCb], [arXiv:2108.13115 [hep-ex]].
- [29] Y. V. Kovchegov and A. H. Mueller, Nucl. Phys. B **529** (1998), 451-479 [arXiv:hep-ph/9802440 [hep-ph]].
- [30] A. Dumitru and J. Jalilian-Marian, Phys. Rev. Lett. **89** (2002), 022301 [arXiv:hep-ph/0204028 [hep-ph]].
- [31] A. Dumitru, A. Hayashigaki and J. Jalilian-Marian, Nucl. Phys. A **770** (2006), 57-70 [arXiv:hep-ph/0512129 [hep-ph]].
- [32] J. L. Albacete and C. Marquet, Phys. Lett. B **687** (2010), 174-179 [arXiv:1001.1378 [hep-ph]].
- [33] E. Levin and A. H. Rezaeian, Phys. Rev. D **82** (2010), 014022 [arXiv:1005.0631 [hep-ph]].
- [34] T. Altinoluk and A. Kovner, Phys. Rev. D **83** (2011), 105004 [arXiv:1102.5327 [hep-ph]].
- [35] H. Fujii, K. Itakura, Y. Kitadono and Y. Nara, J. Phys. G **38** (2011), 124125 [arXiv:1107.1333 [hep-ph]].
- [36] G. A. Chirilli, B. W. Xiao and F. Yuan, Phys. Rev. Lett. **108** (2012), 122301 [arXiv:1112.1061 [hep-ph]].
- [37] G. A. Chirilli, B. W. Xiao and F. Yuan, Phys. Rev. D **86** (2012), 054005 [arXiv:1203.6139 [hep-ph]].
- [38] J. L. Albacete, A. Dumitru, H. Fujii and Y. Nara, Nucl. Phys. A **897** (2013), 1-27 [arXiv:1209.2001 [hep-ph]].
- [39] J. L. Albacete, N. Armesto, R. Baier, G. G. Barnafoldi, J. Barrette, S. De, W. T. Deng, A. Dumitru, K. Dusling and K. J. Eskola, *et al.* Int. J. Mod. Phys. E **22** (2013), 1330007 [arXiv:1301.3395 [hep-ph]].
- [40] A. M. Stasto, B. W. Xiao and D. Zaslavsky, Phys. Rev. Lett. **112** (2014) no.1, 012302 [arXiv:1307.4057 [hep-ph]].
- [41] T. Lappi and H. Mäntysaari, Phys. Rev. D **88** (2013), 114020 [arXiv:1309.6963 [hep-ph]].
- [42] A. van Hameren, P. Kotko, K. Kutak, C. Marquet and S. Sapeta, Phys. Rev. D **89** (2014) no.9, 094014 [arXiv:1402.5065 [hep-ph]].
- [43] A. M. Stasto, B. W. Xiao, F. Yuan and D. Zaslavsky, Phys. Rev. D **90** (2014) no.1, 014047 [arXiv:1405.6311 [hep-ph]].
- [44] T. Altinoluk, N. Armesto, G. Beuf, A. Kovner and M. Lublinsky, Phys. Rev. D **91** (2015) no.9, 094016 [arXiv:1411.2869 [hep-ph]].
- [45] K. Watanabe, B. W. Xiao, F. Yuan and D. Zaslavsky, Phys. Rev. D **92** (2015) no.3, 034026 [arXiv:1505.05183 [hep-ph]].
- [46] A. M. Stasto and D. Zaslavsky, Int. J. Mod. Phys. A **31** (2016) no.24, 1630039 [arXiv:1608.02285 [hep-ph]].
- [47] E. Iancu, A. H. Mueller and D. N. Triantafyllopoulos, JHEP **12** (2016), 041 [arXiv:1608.05293 [hep-ph]].
- [48] B. Ducloué, T. Lappi and Y. Zhu, Phys. Rev. D **93** (2016) no.11, 114016 [arXiv:1604.00225 [hep-ph]].
- [49] B. Ducloué, E. Iancu, T. Lappi, A. H. Mueller, G. Soyez, D. N. Triantafyllopoulos and Y. Zhu, Phys. Rev. D **97** (2018) no.5, 054020 [arXiv:1712.07480 [hep-ph]].
- [50] F. Dominguez, B. W. Xiao and F. Yuan, Phys. Rev. Lett. **106** (2011), 022301 [arXiv:1009.2141 [hep-ph]].
- [51] F. Dominguez, C. Marquet, B. W. Xiao and F. Yuan, Phys. Rev. D **83** (2011), 105005 [arXiv:1101.0715 [hep-ph]].
- [52] D. Kharzeev, Y. V. Kovchegov and K. Tuchin, Phys. Rev. D **68** (2003), 094013 [arXiv:hep-ph/0307037 [hep-ph]].
- [53] D. Kharzeev, Y. V. Kovchegov and K. Tuchin, Phys. Lett. B **599** (2004), 23-31 [arXiv:hep-ph/0405045 [hep-ph]].
- [54] J. L. Albacete, N. Armesto, A. Kovner, C. A. Salgado and U. A. Wiedemann, Phys. Rev. Lett. **92** (2004), 082001 [arXiv:hep-ph/0307179 [hep-ph]].
- [55] E. Iancu, K. Itakura and D. N. Triantafyllopoulos, Nucl. Phys. A **742** (2004), 182-252 [arXiv:hep-ph/0403103 [hep-ph]].
- [56] A. Dumitru, A. Hayashigaki and J. Jalilian-Marian, Nucl. Phys. A **765** (2006), 464-482 [arXiv:hep-ph/0506308 [hep-ph]].
- [57] J. P. Blaizot, F. Gelis and R. Venugopalan, Nucl. Phys. A **743** (2004), 13-56 [arXiv:hep-ph/0402256 [hep-ph]].
- [58] J. P. Blaizot, F. Gelis and R. Venugopalan, Nucl. Phys. A **743** (2004), 57-91 [arXiv:hep-ph/0402257 [hep-ph]].
- [59] M. Bury, H. Van Havermaet, A. Van Hameren, P. Van Mechelen, K. Kutak and M. Serino, Phys. Lett. B **780** (2018), 185-190 [arXiv:1712.08105 [hep-ph]].
- [60] Z. B. Kang, I. Vitev and H. Xing, Phys. Rev. Lett. **113** (2014), 062002 [arXiv:1403.5221 [hep-ph]].
- [61] B. Ducloué, T. Lappi and Y. Zhu, Phys. Rev. D **95** (2017) no.11, 114007 [arXiv:1703.04962 [hep-ph]].
- [62] B. W. Xiao and F. Yuan, Phys. Lett. B **788** (2019), 261-269 [arXiv:1806.03522 [hep-ph]].
- [63] H. Y. Liu, Y. Q. Ma and K. T. Chao, Phys. Rev. D **100** (2019) no.7, 071503 [arXiv:1909.02370 [nucl-th]].
- [64] Z. B. Kang and X. Liu, [arXiv:1910.10166 [hep-ph]].
- [65] H. Y. Liu, Z. B. Kang and X. Liu, Phys. Rev. D **102** (2020) no.5, 051502 [arXiv:2004.11990 [hep-ph]].
- [66] A. H. Mueller and S. Munier, Nucl. Phys. A **893** (2012), 43-86 [arXiv:1206.1333 [hep-ph]].
- [67] M. Hentschinski, J. D. M. Martínez, B. Murdaca and A. Sabio Vera, Nucl. Phys. B **889** (2014), 549-579 [arXiv:1409.6704 [hep-ph]].
- [68] S. Benic, K. Fukushima, O. Garcia-Montero and R. Venugopalan, JHEP **01** (2017), 115 [arXiv:1609.09424 [hep-ph]].
- [69] R. Boussarie, A. V. Grabovsky, D. Y. Ivanov, L. Szymanowski and S. Wallon, Phys. Rev. Lett. **119** (2017) no.7, 072002 [arXiv:1612.08026 [hep-ph]].
- [70] B. Ducloué, H. Hänninen, T. Lappi and Y. Zhu, Phys. Rev. D **96** (2017) no.9, 094017 [arXiv:1708.07328 [hep-ph]].
- [71] K. Roy and R. Venugopalan, JHEP **05** (2018), 013 [arXiv:1802.09550 [hep-ph]].
- [72] K. Roy and R. Venugopalan, Phys. Rev. D **101** (2020)

- no.7, 071505 [arXiv:1911.04519 [hep-ph]].
- [73] K. Roy and R. Venugopalan, Phys. Rev. D **101** (2020) no.3, 034028 [arXiv:1911.04530 [hep-ph]].
- [74] E. Iancu and Y. Mulian, JHEP **03** (2021), 005 [arXiv:2009.11930 [hep-ph]].
- [75] P. Caucal, F. Salazar and R. Venugopalan, [arXiv:2108.06347 [hep-ph]].
- [76] T. Altinoluk, N. Armesto, G. Beuf, M. Martínez and C. A. Salgado, JHEP **07** (2014), 068 [arXiv:1404.2219 [hep-ph]].
- [77] T. Altinoluk, N. Armesto, G. Beuf and A. Moscoso, JHEP **01** (2016), 114 [arXiv:1505.01400 [hep-ph]].
- [78] G. A. Chirilli, JHEP **01** (2019), 118 [arXiv:1807.11435 [hep-ph]].
- [79] T. Altinoluk, G. Beuf, A. Czakajka and A. Tymowska, Phys. Rev. D **104** (2021) no.1, 014019 [arXiv:2012.03886 [hep-ph]].
- [80] P. Sun and F. Yuan, Phys. Rev. D **88** (2013) no.11, 114012 [arXiv:1308.5003 [hep-ph]].
- [81] A. H. Mueller, B. W. Xiao and F. Yuan, Phys. Rev. D **88** (2013) no.11, 114010 [arXiv:1308.2993 [hep-ph]].
- [82] P. Sun, C. P. Yuan and F. Yuan, Phys. Rev. Lett. **113** (2014) no.23, 232001 [arXiv:1405.1105 [hep-ph]].
- [83] G. F. Sterman, Nucl. Phys. B **281** (1987), 310-364.
- [84] S. Catani and L. Trentadue, Nucl. Phys. B **327** (1989), 323-352.
- [85] S. Catani, M. L. Mangano, P. Nason and L. Trentadue, Nucl. Phys. B **478** (1996), 273-310 [arXiv:hep-ph/9604351 [hep-ph]].
- [86] D. de Florian, W. Vogelsang and F. Wagner, Phys. Rev. D **78** (2008), 074025 [arXiv:0807.4515 [hep-ph]].
- [87] S. W. Bosch, B. O. Lange, M. Neubert and G. Paz, Nucl. Phys. B **699** (2004), 335-386 [arXiv:hep-ph/0402094 [hep-ph]].
- [88] T. Becher and M. Neubert, Phys. Lett. B **637** (2006), 251-259 [arXiv:hep-ph/0603140 [hep-ph]].
- [89] T. Becher and M. Neubert, Phys. Rev. Lett. **97** (2006), 082001 [arXiv:hep-ph/0605050 [hep-ph]].
- [90] T. Becher, M. Neubert and B. D. Pecjak, JHEP **01** (2007), 076 [arXiv:hep-ph/0607228 [hep-ph]].
- [91] G. Parisi and R. Petronzio, Nucl. Phys. B **154** (1979), 427-440.
- [92] J. C. Collins, D. E. Soper and G. F. Sterman, Nucl. Phys. B **250** (1985), 199-224.
- [93] J. w. Qiu and X. f. Zhang, Phys. Rev. Lett. **86** (2001), 2724-2727 [arXiv:hep-ph/0012058 [hep-ph]].
- [94] A. D. Martin, W. J. Stirling, R. S. Thorne and G. Watt, Eur. Phys. J. C **63** (2009), 189-285 [arXiv:0901.0002 [hep-ph]].
- [95] D. de Florian, R. Sassot, M. Epele, R. J. Hernández-Pinto and M. Stratmann, Phys. Rev. D **91** (2015) no.1, 014035 [arXiv:1410.6027 [hep-ph]].
- [96] K. J. Golec-Biernat and M. Wusthoff, Phys. Rev. D **59** (1998), 014017 [arXiv:hep-ph/9807513 [hep-ph]].
- [97] A. M. Stasto, K. J. Golec-Biernat and J. Kwiecinski, Phys. Rev. Lett. **86** (2001), 596-599 [arXiv:hep-ph/0007192 [hep-ph]].
- [98] A. H. Mueller, Nucl. Phys. B **558** (1999), 285-303 [arXiv:hep-ph/9904404 [hep-ph]].
- [99] F. Gelis and A. Peshier, Nucl. Phys. A **697** (2002), 879-901 [arXiv:hep-ph/0107142 [hep-ph]].
- [100] J. L. Albacete, N. Armesto, J. G. Milhano, P. Quiroga-Arias and C. A. Salgado, Eur. Phys. J. C **71** (2011), 1705 [arXiv:1012.4408 [hep-ph]].
- [101] K. J. Golec-Biernat, L. Motyka and A. M. Stasto, Phys. Rev. D **65** (2002), 074037 [arXiv:hep-ph/0110325 [hep-ph]].
- [102] Y. V. Kovchegov and H. Weigert, Nucl. Phys. A **784** (2007), 188-226 [arXiv:hep-ph/0609090 [hep-ph]].
- [103] I. Balitsky, Phys. Rev. D **75** (2007), 014001 [arXiv:hep-ph/0609105 [hep-ph]].
- [104] E. Gardi, J. Kuokkanen, K. Rummukainen and H. Weigert, Nucl. Phys. A **784** (2007), 282-340 [arXiv:hep-ph/0609087 [hep-ph]].
- [105] J. L. Albacete and Y. V. Kovchegov, Phys. Rev. D **75** (2007), 125021 [arXiv:0704.0612 [hep-ph]].
- [106] I. Balitsky and G. A. Chirilli, Phys. Rev. D **77** (2008), 014019 [arXiv:0710.4330 [hep-ph]].
- [107] J. Berger and A. Stasto, Phys. Rev. D **83** (2011), 034015 [arXiv:1010.0671 [hep-ph]].
- [108] H. Fujii and K. Watanabe, Nucl. Phys. A **915** (2013), 1-23 [arXiv:1304.2221 [hep-ph]].
- [109] E. Iancu, A. H. Mueller, D. N. Triantafyllopoulos and S. Y. Wei, JHEP **07** (2021), 196 [arXiv:2012.08562 [hep-ph]].

SUPPLEMENTAL MATERIAL

As the supplemental material of the paper, we provide all the technical details attached below, which include the following ten sections.

1. First, we present the summary of the leading-order (LO) and next-to-leading order (NLO) cross-section for hadron productions in pA collisions in the forward rapidity region in both the coordinate space and momentum space in Sec. I. Since the multi-dimensional numerical integrations (ranging from one to eight-dimensional integrations) of the NLO cross-section are pretty demanding, we have to adopt several technical procedures to accelerate the computation and improve the numerical accuracy significantly. For example, it is essential to note that the numerical evaluation of the momentum space expressions is much faster than that of the coordinate space expressions. This improvement is the primary reason that we Fourier transform all the terms of the LO and NLO cross-sections from the coordinate space into the analytic expressions in the momentum space. In addition, to prepare for the threshold resummation discussed below, we also identify the appearance of logarithms in the NLO corrections.
2. With the help of the density plots of the hadron momentum fraction τ at RHIC and LHC energies, we illustrate and discuss the kinematics near the threshold region in detail in Sec. II. These plots allow one to visualize the regions of y and p_T where the threshold logarithms become important and the boundaries due to the small- x kinematic constraint.
3. There are two types of threshold logarithms in forward hadron productions: the collinear and the soft logarithms. Using two complimentary methods, we can resum the collinear part and obtain similar numerical results. First, in Sec. III A, we show that the collinear logarithms can be resummed with the help of the DGLAP equations by resetting the factorization scale μ to the auxiliary semi-hard scale Λ in the parton distribution functions (PDFs) and fragmentation functions (FFs) of the resummed contribution. Alternatively, we also show that one can directly solve the DGLAP equation in the threshold ($\xi \rightarrow 1$) limit and analytically resum the collinear threshold logarithms by using the so-called forward threshold jet function $\Delta(\mu^2, \Lambda^2, \omega)$ in Sec. III B. The latter method is equivalent to the renormalization group approach developed in the soft-collinear effective theory (SCET). Furthermore, we demonstrate that these two resummation approaches are numerically equivalent.
4. Following the above discussion, the soft part of the threshold logarithms is then resummed via the corresponding Sudakov factor. Besides, the remainder of the finite terms due to the mismatch between the running coupling and the fixed coupling cases are then redefined as the Sudakov matching term and implemented as part of the NLO hard factor. The resummation of the soft logarithms is summarized and presented in Sec. IV.
5. For the reader's convenience, we summarize the full resummed expressions after implementing the threshold resummation in Sec. V. The numerical outcomes of the resummed expressions are labeled "resummed" results in our plots.
6. Sec. VI is devoted to discussing the "natural" choice of the semi-hard auxiliary scale Λ . Based on the kinematics and the partonic interactions, we first provide an intuitive way to show that this auxiliary scale Λ^2 is related to the saturation momentum Q_s^2 and the scale $(1 - \xi)k_\perp^2$ when the coupling constant α_s is fixed. Then, using the saddle point approximation, we analytically show that one can reproduce the previous results for the choice of Λ^2 in the fixed coupling case. In addition, for the running coupling case, we further identify the typical value of Λ^2 determined by the saddle point of the resummation integral in coordinate space. According to the quantitative estimate of the typical value for Λ^2 , we thus summarize the corresponding Λ^2 values used in the numerical evaluation at various rapidity bins and collision energies.
7. In Sec. VII, we describe in detail the dipole gluon distributions used in this NLO calculation. First, we adopt the initial condition for the dipole scattering amplitude $S_{x_g}^{(2)}(r_\perp)$ that is widely used in CGC calculations, and then numerically evolve it with the running-coupling Balitsky-Kovchegov (rcBK) equation. Through the numerical Fourier transform, this numerical solution of the scattering amplitude is converted into the transverse momentum-dependent dipole gluon distribution, and it provides us the input for small- x gluons with $x_g \leq 10^{-2}$.
8. Also, we briefly discuss the issue of the correlated uncertainties when we compute the nuclear modification factor from the ratio of the cross-section computed from the pA and pp collisions in Sec. VIII. In principle, the uncertainties of these two cross-sections, obtained by varying the factorization scale μ^2 and the auxiliary scale Λ^2 , are correlated in theory calculations since they are computed from the same CGC formalism.
9. In addition, to bridge our theoretical calculation and experimental data reported by different collaborations at RHIC and the LHC, we adopt a systematic conversion between the hadron multiplicities computed in our framework and the measured cross-sections (multiplicities) for various hadrons.

All of our numerical results are obtained from the rcBK solution described above and calculated with a uniform set of parameters. We provide the details of the relation between our theoretical calculation and various experimental measurements in Sec. IX.

10. In Sec. X, we present many additional plots and show the detailed comparisons of our numerical calculations with all of the available RHIC and the LHC data measured in forward pp and pPb collisions, and further discuss the range of validity of the CGC calculation at both RHIC and the LHC kinematic regimes.

I. THE CROSS-SECTIONS AT ONE-LOOP ORDER

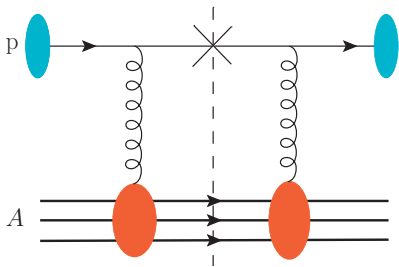


FIG. 3. LO diagram for the $q \rightarrow q$ channel in pA collisions.

As shown in Fig. 3, forward single inclusive hadron productions in pA collisions at leading order (LO) in the CGC formalism can be modeled as follows: A collinear parton (either a quark or a gluon) from the projectile proton interacts with the dense gluon fields in the nuclear target before it fragments into an observed hadron with the transverse momentum p_T at the rapidity y . In high energy limit, the LO cross-section is cast into [30]

$$\frac{d\sigma^{\text{LO}}}{dyd^2p_T} = \int_{\tau}^1 \frac{dz}{z^2} \sum_f x_p q_f(x_p) \mathcal{F}^{x_g}(k_{\perp}) D_{h/q}(z) + \int_{\tau}^1 \frac{dz}{z^2} x_p g(x_p) \tilde{\mathcal{F}}^{x_g}(k_{\perp}) D_{h/g}(z), \quad (8)$$

where $q_f(x_p)$ and $g(x_p)$ represent the quark and gluon collinear PDF with the longitudinal momentum fraction x_p , respectively. $D_{h/q,g}(z)$ is the corresponding FF which describes the probability density of a quark or a gluon fragmenting into a hadron with the momentum fraction z . These quantities all depend on the so-called factorization scale μ due to the DGLAP evolution of the PDF and FF. The dependence on μ in the PDF and FF can be compensated and thus reduced by higher order corrections in the hard factor. $\mathcal{F}^{x_g}(k_{\perp})$ and $\tilde{\mathcal{F}}^{x_g}(k_{\perp})$ stand for the Fourier transforms of the dipole scattering amplitude in the fundamental and adjoint representations, respectively. If we define the quark dipole amplitude

as $S_{x_g}^{(2)}(r_{\perp})$, then $\mathcal{F}^{x_g}(k_{\perp}) \equiv S_{\perp} \int \frac{d^2r_{\perp}}{(2\pi)^2} e^{-ik_{\perp} \cdot r_{\perp}} S_{x_g}^{(2)}(r_{\perp})$. S_{\perp} is defined as the effective transverse area of the target nucleus obtained after averaging over the impact parameter. It is usually convenient to define $F(\eta, k_{\perp}) \equiv \mathcal{F}^{x_g}(k_{\perp})/S_{\perp} = \int \frac{d^2r_{\perp}}{(2\pi)^2} e^{-ik_{\perp} \cdot r_{\perp}} S_{x_g}^{(2)}(r_{\perp})$ in solving the rcBK evolution equation with $\eta = \ln \frac{x_0}{x_g}$ and $x_0 = 0.01$.

In principle, $F(\eta, k_{\perp})$ and $S_{x_g}^{(2)}(r_{\perp})$ depend on x_g or η . We suppress the x_g or η dependence for simplicity in the following sections. The adjoint representation of the dipole amplitude yields $\tilde{\mathcal{F}}^{x_g}(k_{\perp})$ accordingly. These two dipole amplitudes encode the strength of the multiple interactions between the quark/gluon projectiles and the dense gluon fields in the small- x regime inside the nuclear target. At LO, the transverse momentum k_{\perp} of the final state measured parton is determined by the transverse momentum that the incoming quark/gluon receives due to the multiple interaction. The LO kinematics imply $x_p = k_{\perp} e^y / \sqrt{s}$, $x_g = k_{\perp} e^{-y} / \sqrt{s}$ and $p_T = z k_{\perp}$. \sqrt{s} is the total energy in the center-of-mass frame for pp collisions, and it is identified as the center-of-mass energy per nucleon pair $\sqrt{s_{\text{NN}}}$ in dAu or pPb collisions in our calculation. The advantage of measuring hadron productions in the forward rapidity region is that the active parton from the proton projectile is from the large x region while target gluon fields deep in the low- x region are probed.

By considering the diagrams of the real emission of an additional gluon and the corresponding virtual contributions in this process as illustrated in Fig. 4, we can compute hadron production at the one-loop order. At this order, both the collinear and rapidity divergence appear in the one-loop contributions. Although the results of the one-loop diagrams are unique, there are freedoms for divergence subtractions. For example, one can choose either the modified minimal subtraction ($\overline{\text{MS}}$) scheme or other schemes when one removes collinear divergences from one-loop contributions. In our calculation, we adopt the $\overline{\text{MS}}$ scheme in order to implement the widely used PDFs and FFs in numerical calculations. Similarly, there are various proposals of scheme choices for the subtraction of the rapidity logarithm [47–49, 60, 61, 63–65]. In this paper, we follow the scheme choice adopted in Refs. [36, 37, 45], and we only subtract the exact amount of the logarithm $\alpha_s \ln \frac{1}{x_g}$ from the one-loop contributions according to the LO kinematics. Therefore, the corresponding amount of the rapidity evolution that is put into the rcBK equation is then $\Delta\eta = \ln \frac{1}{x_g}$. In light of recent new developments of other factorization schemes, such as the one proposed in Refs. [47–49, 70], it will be interesting to explore the numerical performance of these schemes and further improve the NLO calculations in CGC framework. Nevertheless, we leave this for a future study.

After subtracting all the divergences under the chosen schemes, the NLO corrections are free of any singularities and they can be evaluated numerically. Based on the calculation presented in Refs. [36, 37, 45], the results for the NLO cross-sections are summarized below.

A. $q \rightarrow q$ channel

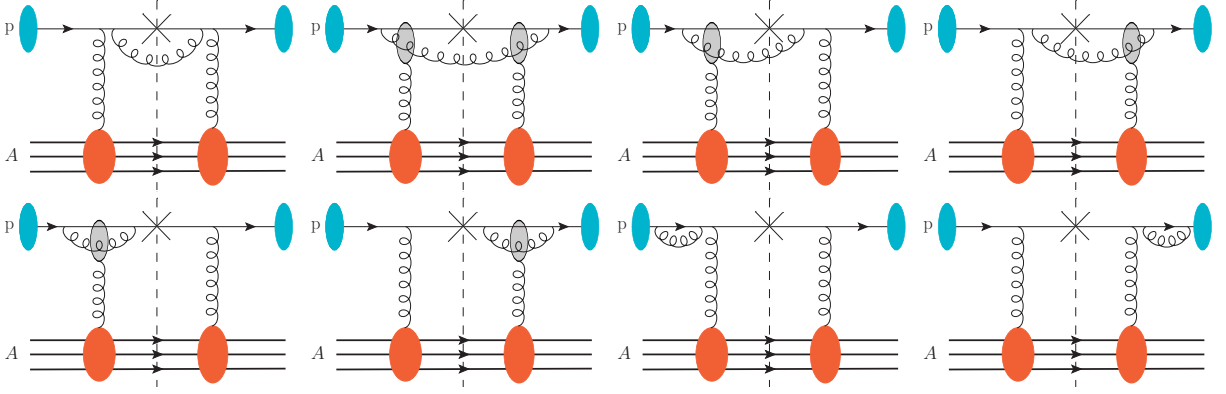


FIG. 4. The NLO real and virtual diagrams for the $q \rightarrow q$ channel in pA collisions. Here the grey blobs indicate where non-linear multiple interactions occur between the vertical gluons and the quark-gluon pair.

The cross-section in the coordinate space has been obtained in Refs. [36, 37] with two additional terms presented in Ref. [45]. To be self-contained, we summarize the final results here as the starting point. In the large N_c limit, the complete one-loop cross-section for the $q \rightarrow q$ channel is divided into the following parts

$$\frac{d\sigma_{qq}}{dyd^2p_T} = \frac{d\sigma_{qq}^{\text{LO}}}{dyd^2p_T} + \frac{d\sigma_{qq}^{\text{NLO}}}{dyd^2p_T} = \frac{d\sigma_{qq}^{\text{LO}}}{dyd^2p_T} + \sum_{i=a}^e \frac{d\sigma_{qq}^i}{dyd^2p_T}, \quad (9)$$

where the LO and NLO parts read

$$\frac{d\sigma_{qq}^{\text{LO}}}{dyd^2p_T} = S_{\perp} \int_{\tau}^1 \frac{dz}{z^2} x_p q(x_p, \mu^2) D_{h/q}(z, \mu^2) \int \frac{d^2 r_{\perp}}{(2\pi)^2} e^{-ik_{\perp} \cdot r_{\perp}} S^{(2)}(r_{\perp}), \quad (10)$$

$$\begin{aligned} \frac{d\sigma_{qq}^a}{dyd^2p_T} &= \frac{\alpha_s}{2\pi} S_{\perp} C_F \int_{\tau}^1 \frac{dz}{z^2} \int_{\tau/z}^1 d\xi x q(x, \mu^2) D_{h/q}(z, \mu^2) \mathcal{P}_{qq}(\xi) \int \frac{d^2 r_{\perp}}{(2\pi)^2} \ln \frac{c_0^2}{r_{\perp}^2 \mu^2} \\ &\times \left(e^{-ik_{\perp} \cdot r_{\perp}} + \frac{1}{\xi^2} e^{-i\frac{1}{\xi} k_{\perp} \cdot r_{\perp}} \right) S^{(2)}(r_{\perp}), \end{aligned} \quad (11)$$

$$\frac{d\sigma_{qq}^b}{dyd^2p_T} = -3 \frac{\alpha_s}{2\pi} S_{\perp} C_F \int_{\tau}^1 \frac{dz}{z^2} x_p q(x_p, \mu^2) D_{h/q}(z, \mu^2) \int \frac{d^2 r_{\perp}}{(2\pi)^2} e^{-ik_{\perp} \cdot r_{\perp}} S^{(2)}(r_{\perp}) \ln \frac{c_0^2}{r_{\perp}^2 k_{\perp}^2}, \quad (12)$$

$$\begin{aligned} \frac{d\sigma_{qq}^c}{dyd^2p_T} &= -8\pi \frac{\alpha_s}{2\pi} S_{\perp} C_F \int_{\tau}^1 \frac{dz}{z^2} \int_{\tau/z}^1 d\xi x q(x, \mu^2) D_{h/q}(z, \mu^2) \int \frac{d^2 u_{\perp} d^2 v_{\perp}}{(2\pi)^4} e^{-ik_{\perp} \cdot (u_{\perp} - v_{\perp})} e^{-i\frac{1-\xi}{\xi} k_{\perp} \cdot u_{\perp}} \\ &\times \frac{1 + \xi^2}{(1-\xi)_+} \frac{1}{\xi} \frac{u_{\perp} \cdot v_{\perp}}{u_{\perp}^2 v_{\perp}^2} S^{(2)}(u_{\perp}) S^{(2)}(v_{\perp}), \end{aligned} \quad (13)$$

$$\begin{aligned} \frac{d\sigma_{qq}^d}{dyd^2p_T} &= 8\pi \frac{\alpha_s}{2\pi} S_{\perp} C_F \int_{\tau}^1 \frac{dz}{z^2} x_p q(x_p, \mu^2) D_{h/q}(z, \mu^2) \int \frac{d^2 u_{\perp} d^2 v_{\perp}}{(2\pi)^4} e^{-ik_{\perp} \cdot (u_{\perp} - v_{\perp})} S^{(2)}(u_{\perp}) S^{(2)}(v_{\perp}) \\ &\times \int_0^1 d\xi' \frac{1 + \xi'^2}{(1-\xi')_+} \left(e^{-i(1-\xi') k_{\perp} \cdot v_{\perp}} \frac{1}{v_{\perp}^2} - \delta^2(v_{\perp}) \int d^2 r'_{\perp} e^{ik_{\perp} \cdot r'_{\perp}} \frac{1}{r'_{\perp}{}^2} \right), \end{aligned} \quad (14)$$

$$\begin{aligned} \frac{d\sigma_{qq}^e}{dyd^2p_T} &= \frac{\alpha_s}{\pi^2} S_{\perp} \frac{N_c}{2} \int_{\tau}^1 \frac{dz}{z^2} x_p q(x_p, \mu^2) D_{h/q}(z, \mu^2) \int \frac{d^2 u_{\perp} d^2 v_{\perp}}{(2\pi)^2} e^{-ik_{\perp} \cdot (u_{\perp} - v_{\perp})} [S^{(2)}(u_{\perp}) S^{(2)}(v_{\perp}) - S^{(2)}(u_{\perp} - v_{\perp})] \\ &\times \left[\frac{1}{u_{\perp}^2} \ln \frac{k_{\perp}^2 u_{\perp}^2}{c_0^2} + \frac{1}{v_{\perp}^2} \ln \frac{k_{\perp}^2 v_{\perp}^2}{c_0^2} - \frac{2u_{\perp} \cdot v_{\perp}}{u_{\perp}^2 v_{\perp}^2} \ln \frac{k_{\perp}^2 |u_{\perp}| |v_{\perp}|}{c_0^2} \right], \end{aligned} \quad (15)$$

with the kinematic variables $x_p = \tau/z$, $x = x_p/\xi$, and $k_{\perp} = p_T/z$. The coordinate variables are defined as follows $r_{\perp} = x_{\perp} - y_{\perp}$, $u_{\perp} = x_{\perp} - b_{\perp}$, $v_{\perp} = y_{\perp} - b_{\perp}$. For convenience, we also denote $c_0 = 2e^{-\gamma_E}$ with γ_E the Euler constant and the splitting function $\mathcal{P}_{qq}(\xi) = \frac{1+\xi^2}{(1-\xi)_+} + \frac{3}{2}\delta(1-\xi)$. For simplicity, $S^{(2)}(r_{\perp})$ is assumed to be only a function

of $|r_\perp|$ while the impact parameter dependence is neglected throughout this calculation. Therefore, one can simply define $S_\perp = \int d^2 R_\perp$ as the effective transverse area of the target nucleus after integrating over the impact parameter R_\perp . The first four terms σ_{qq}^{a-d} among the NLO corrections are first derived in Refs. [36, 37] and the last term σ_{qq}^e is due to the kinematic constraint as illustrated in Ref. [45]. As we show in the discussion in Sec. VI, there are two logarithms $\ln \frac{1}{x_g}$ and $\ln \frac{k_\perp^2}{q_\perp^2}$ arising from the rapidity integral when we consider the kinematic constraint. The first logarithm $\ln \frac{1}{x_g}$ is corresponding to the rapidity divergence when the center of mass energy \sqrt{s} is taken to be ∞ , and it is resummed through the BK evolution equation. In our scheme choice, we keep the second logarithm $\ln \frac{k_\perp^2}{q_\perp^2}$ in the NLO hard factor and this eventually gives rise to the last term σ_{qq}^e as shown in Ref. [45].

In arriving the above expressions, we have taken the large N_c limit and assumed the Gaussian approximation for color charge distributions inside the target nucleus. Then, we can safely neglect the NLO corrections which are suppressed by $1/N_c^2$, and we also simplify multiple point correlation functions and write them in terms of products of dipole amplitudes $S^{(2)}$ as shown in the last three terms, i.e., σ_{qq}^c , σ_{qq}^d , and σ_{qq}^e . Since we do not distinguish between $N_c/2$ and C_F in the large N_c limit, we have replaced the color factors in σ_{qq}^c , σ_{qq}^d by C_F and we will change the color factor $\frac{N_c}{2}$ in σ_{qq}^e to C_F in the following discussions.

Although the physical interpretation of each NLO correction is manifest in the above coordinate space expressions [36, 37], it is challenging to evaluate some of the NLO corrections accurately in numerical computations, especially in the LHC kinematic regime. To achieve better numerical performance, we adopt an analytical procedure including the following three steps of manipulations: 1. Fourier transform; 2. Combining terms that are cancelling each other; 3. Shifting coordinates.

1. Fourier Transform

Due to the oscillatory behavior of the phase factor $e^{-ik_\perp \cdot r_\perp}$, which can be translated into a Bessel function $J_0(|k_\perp||r_\perp|)$ after averaging over the azimuthal angle, it is notoriously difficult to numerically calculate the cross-section in the coordinate space especially in the large k_\perp region. To achieve a much better numerical performance, we analytically transform all of the above coordinate space expressions to the momentum space. This step is vital in the numerical evaluation of the NLO corrections since we need to perform up to eight-dimensional numerical integrations with high precision.

The Fourier transform of the σ_{qq}^{LO} term is straightforward, while the transforms of other terms are less trivial. For example, let us consider the Fourier transform of the σ_{qq}^a and σ_{qq}^b terms. Since the splitting function $\mathcal{P}_{qq}(\xi) = \frac{1+\xi^2}{(1-\xi)_+} + \frac{3}{2}\delta(1-\xi)$ contains two terms, we can rewrite σ_{qq}^a as

$$\begin{aligned} \frac{d\sigma_{qq}^a}{dyd^2p_T} &= \frac{\alpha_s}{2\pi} S_\perp C_F \int_\tau^1 \frac{dz}{z^2} \int_{\tau/z}^1 d\xi xq(x, \mu^2) D_{h/q}(z, \mu^2) \frac{1+\xi^2}{(1-\xi)_+} \int \frac{d^2 r_\perp}{(2\pi)^2} \ln \frac{c_0^2}{r_\perp^2 \mu^2} \\ &\quad \times \left(e^{-ik_\perp \cdot r_\perp} + \frac{1}{\xi^2} e^{-i\frac{1}{\xi} k_\perp \cdot r_\perp} \right) S^{(2)}(r_\perp) \\ &\quad + 3 \frac{\alpha_s}{2\pi} S_\perp C_F \int_\tau^1 \frac{dz}{z^2} x_p q(x_p, \mu^2) D_{h/q}(z, \mu^2) \int \frac{d^2 r_\perp}{(2\pi)^2} e^{-ik_\perp \cdot r_\perp} S^{(2)}(r_\perp) \ln \frac{c_0^2}{r_\perp^2 \mu^2}. \end{aligned} \quad (16)$$

We then combine the second term in Eq. (16), which is proportional to $\ln \frac{c_0^2}{r_\perp^2 \mu^2}$, together with σ_{qq}^b , which is proportional to $-\ln \frac{c_0^2}{r_\perp^2 k_\perp^2}$, and obtain the following contribution

$$3 \frac{\alpha_s}{2\pi} S_\perp C_F \int_\tau^1 \frac{dz}{z^2} x_p q(x_p, \mu^2) D_{h/q}(z, \mu^2) \int \frac{d^2 r_\perp}{(2\pi)^2} e^{-ik_\perp \cdot r_\perp} S^{(2)}(r_\perp) \ln \frac{k_\perp^2}{\mu^2}. \quad (17)$$

The Fourier transform of this term is then straightforward. For the remaining terms of σ_{qq}^a (i.e., the first term of Eq. (16)), the derivation is a bit more involved. We use the following identities

$$\begin{aligned} \int \frac{d^2 r_\perp}{(2\pi)^2} e^{-ik_\perp \cdot r_\perp} S^{(2)}(r_\perp) \ln \frac{c_0^2}{r_\perp^2 \mu^2} &= \frac{1}{\pi} \int \frac{d^2 l_\perp}{l_\perp^2} \left[F(k_\perp - l_\perp) - J_0 \left(\frac{c_0}{\mu} |l_\perp| \right) F(k_\perp) \right] \\ &= \frac{1}{\pi} \int \frac{d^2 l_\perp}{l_\perp^2} \left[F(k_\perp - l_\perp) - \frac{\Lambda^2}{\Lambda^2 + l_\perp^2} F(k_\perp) \right] + F(k_\perp) \ln \frac{\Lambda^2}{\mu^2}, \end{aligned} \quad (18)$$

where we introduce a convenient notation for the dipole gluon distribution $F(k_\perp) \equiv \int \frac{d^2 r_\perp}{(2\pi)^2} e^{-ik_\perp \cdot r_\perp} S^{(2)}(r_\perp)$ (note that $\mathcal{F}^{x_g}(k_\perp) \equiv S_\perp F(k_\perp)$ as previously defined). The second term arises from the integral identity

$$\frac{1}{\pi} \int \frac{d^2 l_\perp}{l_\perp^2} \left[\frac{\Lambda^2}{\Lambda^2 + l_\perp^2} - J_0 \left(\frac{c_0}{\mu} |l_\perp| \right) \right] = \ln \frac{\Lambda^2}{\mu^2}. \quad (19)$$

To optimize the Monte Carlo integrations and extract the large logarithm, we add and subtract a regulator term $\frac{1}{\pi l_\perp^2} \frac{\Lambda^2}{\Lambda^2 + l_\perp^2} F(k_\perp)$ and eventually obtain two terms shown in Eq. (18). The choice of the regulating counter term is not unique. It is straightforward to find that one gets the same result if one replaces $\frac{\Lambda^2}{\Lambda^2 + l_\perp^2}$ by $J_0 \left(\frac{c_0}{\Lambda} |l_\perp| \right)$ in the above equation. Nevertheless, it appears that the counter term $\frac{\Lambda^2}{\Lambda^2 + l_\perp^2}$ is better behaved in numerical evaluations since it does not have the oscillatory behavior as $J_0 \left(\frac{c_0}{\Lambda} |l_\perp| \right)$ does.

As shown in the above mathematical manipulation, an auxiliary scale Λ^2 has been introduced and it is clear that Eq. (18) does not depend on the value of the auxiliary scale Λ^2 . The second term of Eq. (18) is finite as long as $\Lambda \neq 0$ and it is ready for resummation as it is proportional to $F(k_\perp)$. With proper choices of Λ^2 , one can extract the corresponding logarithms and efficiently evaluate the remaining first term in numerical computations.

Furthermore, this auxiliary scale can receive the physical interpretation as the semi-hard scale related to the saturation momentum or the semi-hard scale in the threshold resummation. For example, when $k_\perp^2 \sim Q_s^2$, a reasonable choice of Λ^2 is expected to be Q_s^2 . In this case, on the LHS of Eq. (18), the r_\perp integral is dominated by the region where $r_\perp \sim 1/Q_s$. Meanwhile, the desired logarithm $\ln \frac{Q_s^2}{\mu^2}$ naturally arises from the second term once we set $\Lambda^2 = Q_s^2$, while the first term on the RHS of Eq. (18) should be small due to the cancellation between those two terms inside the square brackets. When $k_\perp^2 \gg Q_s^2$ near the threshold regime, Λ^2 can act as the semi-hard scale separating the hard momentum exchange and the soft momentum emission. In the latter case, the ‘‘natural’’ choice of Λ^2 will be discussed in detail later.

As for σ_{qq}^c , the Fourier transform gives

$$\begin{aligned} \frac{d\sigma_{qq}^c}{dy d^2 p_T} &= \frac{\alpha_s}{2\pi^2} C_F S_\perp \int_\tau^1 \frac{dz}{z^2} \int_{\tau/z}^1 d\xi x q(x, \mu^2) D_{h/q}(z, \mu^2) \int d^2 q_{1\perp} d^2 q_{2\perp} F(q_{1\perp} - k_\perp/\xi) F(q_{2\perp} - k_\perp) \\ &\times \frac{1}{\xi} \frac{1 + \xi^2}{(1 - \xi)_+} \frac{-2q_{1\perp} \cdot q_{2\perp}}{q_{1\perp}^2 q_{2\perp}^2}. \end{aligned} \quad (20)$$

In the step discussed in the next subsection, we will combine σ_{qq}^c with the first term on the RHS of Eq. (18) to expedite the numerical integration when k_\perp is large.

In addition, to deal with the σ_{qq}^d term, we need to employ the following identity

$$\int \frac{d^2 r_\perp}{(2\pi)^2} e^{-iq_{1\perp} \cdot r_\perp} \frac{1}{r_\perp^2} = \lim_{\rho \rightarrow 0} \int \frac{d^2 r_\perp}{(2\pi)^2} e^{-iq_{1\perp} \cdot r_\perp} \frac{1}{r_\perp^2 + \rho^2} = \frac{1}{2\pi} \lim_{\rho \rightarrow 0} K_0(\rho q_{1\perp}). \quad (21)$$

where we have introduced an infinitesimal parameter ρ to regulate the divergence. The two terms in σ^d correspond to the following kernel

$$\frac{1}{2\pi} \lim_{\rho \rightarrow 0} [K_0(\rho(q_{1\perp} - \xi' k_\perp)) - K_0(\rho k_\perp)] = -\frac{1}{4\pi} \ln \frac{(q_{1\perp} - \xi' k_\perp)^2}{k_\perp^2}, \quad (22)$$

which leads to a finite contribution after cancelling the logarithmic divergences between them. Therefore, the Fourier transform of σ_{qq}^d becomes σ_{qq}^4 as shown in Eq. (41).

The Fourier transform of σ_{qq}^e is the most difficult one. The analytical techniques have been outlined in Ref. [45], thus only a brief summary of the steps is provided here. By employing the following relations

$$\frac{1}{r_\perp^2} \ln \frac{k_\perp^2 r_\perp^2}{c_0^2} = \frac{1}{8\pi} \int d^2 q_{1\perp} e^{iq_{1\perp} \cdot r_\perp} \ln^2 \frac{k_\perp^2}{q_{1\perp}^2}, \quad (23)$$

$$\frac{\vec{r}_\perp}{r_\perp^2} \ln \frac{k_\perp^2 r_\perp^2}{c_0^2} = \frac{1}{2\pi} \int d^2 q_{1\perp} e^{iq_{1\perp} \cdot r_\perp} \frac{i\vec{q}_{1\perp}}{q_{1\perp}^2} \ln \frac{k_\perp^2}{q_{1\perp}^2}, \quad (24)$$

we can convert the terms in σ_{qq}^e into the following three terms

$$\frac{d\sigma_{qq}^e}{dy d^2 p_T} = \int_\tau^1 \frac{dz}{z^2} x_p q(x_p, \mu^2) D_{h/q}(z, \mu^2) [L_{q1}(k_\perp) + L_{q2}(k_\perp) + L_{q3}(k_\perp)] \quad (25)$$

$$\begin{aligned}
L_{q1}(k_\perp) &= -\frac{2\alpha_s}{\pi^2} C_F S_\perp \int \frac{d^2 u_\perp d^2 v_\perp}{(2\pi)^2} e^{-ik_\perp \cdot (u_\perp - v_\perp)} S^{(2)}(u_\perp - v_\perp) \left[\frac{1}{u_\perp^2} \ln \frac{k_\perp^2 u_\perp^2}{c_0^2} - \frac{u_\perp \cdot v_\perp}{u_\perp^2 v_\perp^2} \ln \frac{k_\perp^2 |u_\perp| |v_\perp|}{c_0^2} \right] \\
&= \lim_{\rho \rightarrow 0} \frac{\alpha_s}{\pi} C_F S_\perp \int \frac{d^2 r_\perp}{(2\pi)^2} e^{-ik_\perp \cdot r_\perp} S^{(2)}(r_\perp) \left[-\ln^2 \frac{k_\perp^2}{\rho^2} + 4 \int_\rho^\infty \frac{dq_{1\perp}}{q_{1\perp}} \ln \frac{k_\perp^2}{q_{1\perp}^2} J_0(q_{1\perp} r_\perp) \right] \\
&= -\frac{\alpha_s}{2\pi^2} C_F S_\perp \int \frac{d^2 r_\perp}{2\pi} e^{-ik_\perp \cdot r_\perp} S^{(2)}(r_\perp) \ln^2 \frac{k_\perp^2 r_\perp^2}{c_0^2}, \tag{26}
\end{aligned}$$

$$\begin{aligned}
L_{q2}(k_\perp) &= \frac{2\alpha_s}{\pi^2} S_\perp C_F \int \frac{d^2 u_\perp d^2 v_\perp}{(2\pi)^2} e^{-ik_\perp \cdot (u_\perp - v_\perp)} S^{(2)}(u_\perp) S^{(2)}(v_\perp) \frac{1}{u_\perp^2} \ln \frac{k_\perp^2 u_\perp^2}{c_0^2} \\
&= \frac{\alpha_s}{\pi} C_F S_\perp F(k_\perp) \int d^2 q_{1\perp} F(k_\perp - q_{1\perp}) \ln^2 \frac{k_\perp^2}{q_{1\perp}^2}, \tag{27}
\end{aligned}$$

$$\begin{aligned}
L_{q3}(k_\perp) &= -\frac{2\alpha_s}{\pi^2} S_\perp C_F \int \frac{d^2 u_\perp d^2 v_\perp}{(2\pi)^2} e^{-ik_\perp \cdot (u_\perp - v_\perp)} S^{(2)}(u_\perp) S^{(2)}(v_\perp) \frac{u_\perp \cdot v_\perp}{u_\perp^2 v_\perp^2} \ln \frac{k_\perp^2 |u_\perp| |v_\perp|}{c_0^2} \\
&= -\frac{2\alpha_s}{\pi^2} S_\perp C_F \int d^2 q_{1\perp} d^2 q_{2\perp} F(k_\perp - q_{1\perp}) F(k_\perp - q_{2\perp}) \frac{q_{1\perp} \cdot q_{2\perp}}{q_{1\perp}^2 q_{2\perp}^2} \ln \frac{k_\perp^2}{q_{1\perp}^2}, \tag{28}
\end{aligned}$$

where we have introduced ρ as an infrared cutoff to regularize the integration in Eq. (26). While the last two terms are already in the momentum space, Eq. (26) needs an extra step of manipulation. To perform the Fourier transform of the double logarithmic factor $\ln^2 \frac{k_\perp^2 r_\perp^2}{c_0^2}$, we utilize the following relations inspired by the Sudakov double logarithm calculation[45, 81] in the dimensional regularization

$$\left(\frac{\mu^2 e^{\gamma_E}}{4\pi} \right)^\epsilon \int \frac{d^{2-2\epsilon} q_{1\perp}}{(2\pi)^{2-2\epsilon} q_{1\perp}^2} e^{-iq_{1\perp} \cdot r_\perp} \ln \frac{k_\perp^2}{q_{1\perp}^2} = \frac{1}{4\pi} \left[\frac{1}{\epsilon^2} - \frac{1}{\epsilon} \ln \frac{k_\perp^2}{\mu^2} + \frac{1}{2} \ln^2 \frac{k_\perp^2}{\mu^2} - \frac{1}{2} \ln^2 \frac{k_\perp^2 r_\perp^2}{c_0^2} - \frac{\pi^2}{12} \right], \tag{29}$$

$$\left(\frac{\mu^2 e^{\gamma_E}}{4\pi} \right)^\epsilon \int \frac{d^{2-2\epsilon} q_{1\perp}}{(2\pi)^{2-2\epsilon} q_{1\perp}^2} \ln \frac{k_\perp^2}{q_{1\perp}^2} \theta(k_\perp^2 - q_{1\perp}^2) = \frac{1}{4\pi} \left[\frac{1}{\epsilon^2} - \frac{1}{\epsilon} \ln \frac{k_\perp^2}{\mu^2} + \frac{1}{2} \ln^2 \frac{k_\perp^2}{\mu^2} - \frac{\pi^2}{12} \right]. \tag{30}$$

By taking the difference of these two terms, we obtain

$$\ln^2 \frac{k_\perp^2 r_\perp^2}{c_0^2} = 8\pi \int \frac{d^2 q_{1\perp}}{(2\pi)^2} \frac{1}{q_{1\perp}^2} \ln \frac{k_\perp^2}{q_{1\perp}^2} [\theta(k_\perp^2 - q_{1\perp}^2) - e^{-iq_{1\perp} \cdot r_\perp}]. \tag{31}$$

With the above relations, we can easily find

$$\int \frac{d^2 r_\perp}{(2\pi)^2} e^{-ik_\perp \cdot r_\perp} S^{(2)}(r_\perp) \ln^2 \frac{k_\perp^2 r_\perp^2}{c_0^2} = \frac{2}{\pi} \int \frac{d^2 q_{1\perp}}{q_{1\perp}^2} \ln \frac{k_\perp^2}{q_{1\perp}^2} [\theta(k_\perp^2 - q_{1\perp}^2) F(k_\perp) - F(k_\perp - q_{1\perp})]. \tag{32}$$

Finally, the Fourier transform of σ_{qq}^e becomes σ_{qq}^5 as given in Eq. (42).

2. Combinations of terms

Using the normalization of $F(q_{1\perp})$, we can rewrite the first term of Eq. (18) as

$$\frac{1}{\pi} \int d^2 q_{1\perp} d^2 q_{2\perp} \frac{1}{q_{2\perp}^2} F(q_{1\perp}) \left[F(q_{2\perp} - k_\perp) - \frac{\Lambda^2}{\Lambda^2 + q_{2\perp}^2} F(k_\perp) \right]. \tag{33}$$

σ_{qq}^a contains two Fourier transforms. Combining these two terms from σ_{qq}^a with σ_{qq}^c , we obtain σ_{qq}^3 in the momentum space with the following kernel

$$\begin{aligned}
&\int d^2 q_{1\perp} d^2 q_{2\perp} \left[\frac{(q_{2\perp} - q_{1\perp}/\xi)^2}{q_{1\perp}^2 q_{2\perp}^2} F(q_{1\perp} - k_\perp/\xi) F(q_{2\perp} - k_\perp) \right. \\
&\quad \left. - \frac{1}{q_{1\perp}^2} \frac{\Lambda^2}{\Lambda^2 + q_{1\perp}^2} F(q_{2\perp}) F(k_\perp) - \frac{1}{\xi^2 q_{2\perp}^2} \frac{\Lambda^2}{\Lambda^2 + q_{2\perp}^2} F(k_\perp/\xi) F(q_{1\perp}) \right]. \tag{34}
\end{aligned}$$

In the above expression, the poles at $|q_{1\perp}| = 0$ in the first and second terms cancel each other and those at $|q_{2\perp}| = 0$ in the first and third terms also cancel each other. Therefore, the above formula is free from any divergences. However,

the integration region of $|q_{1\perp}|$ and $|q_{2\perp}|$ is from 0 to $+\infty$, which is impossible to implement exactly in the Monte Carlo simulation. In practice, we always numerically integrate in the finite region and assume that the contribution from outside is negligible. The validity of this technique requires that the integrand falls off much faster than $\frac{1}{V}$ with V being the volume of integration region. The dominant contribution of the first term in Eq. (34) arises from both $q_{1\perp} \sim 0$, $q_{2\perp} \sim 0$ and $q_{1\perp} \sim k_{\perp}/\xi$ and $q_{2\perp} \sim k_{\perp}$, while that of the second and third terms comes only from $q_{1\perp} \sim 0$, $q_{2\perp} \sim 0$. Each term results in a large contribution while the sum of them is relatively small. The cancellation of large contributions does not occur at the integrand level since the dominant contributions of these three terms arise from different $|q_{1\perp}|$ and $|q_{2\perp}|$ regions. Therefore, if one directly evaluates Eq. (34), it may consume enormous amount of computing resources in order to obtain accurate numerical results. Besides, the final results may also be sensitive to the upper cuts of $|q_{1\perp}|$ and $|q_{2\perp}|$ in the numerical implementation, if these cuts are not sufficiently large enough. This issue can be significantly mitigated by shifting the momentum coordinates as discussed in the following subsection.

3. Shifting Coordinates

The above-mentioned numerical challenges can be solved by coordinate shifts. Defining $q'_{1\perp} = q_{1\perp} - k_{\perp}/\xi$ and $q'_{2\perp} = q_{2\perp} - k_{\perp}$, we switch to the following optimized expression for numerical evaluation

$$\begin{aligned} \int d^2q_{1\perp} d^2q_{2\perp} & \left[\frac{(q_{2\perp} - q_{1\perp}/\xi)^2}{(k_{\perp} + q_{1\perp})^2 (k_{\perp}/\xi + q_{2\perp})^2} F(q_{1\perp}) F(q_{2\perp}) \right. \\ & - \frac{1}{(k_{\perp} + q_{1\perp})^2} \frac{\Lambda^2}{\Lambda^2 + (k_{\perp} + q_{1\perp})^2} F(q_{2\perp}) F(k_{\perp}) \\ & \left. - \frac{1}{(k_{\perp} + \xi q_{2\perp})^2} \frac{\Lambda^2}{\Lambda^2 + (k_{\perp}/\xi + q_{2\perp})^2} F(k_{\perp}/\xi) F(q_{1\perp}) \right]. \end{aligned} \quad (35)$$

It is straightforward to show that Eq. (35) and Eq. (34) are equivalent. The dominant contributions of these three terms come from the small $|q_{1\perp}|$ and small $|q_{2\perp}|$ region. The cancellation now occurs at the integrand level. Therefore, it is much more efficient to numerically evaluate Eq. (35) rather than Eq. (34), although they are analytically equivalent.

4. The full NLO/one-loop corrections in the momentum space

At the end of the day, we arrive at the results of the one-loop cross-section in the momentum space in the large N_c limit after following the above three-step procedure

$$\frac{d\sigma_{qq}}{dyd^2p_T} = \frac{d\sigma_{qq}^{\text{LO}}}{dyd^2p_T} + \frac{d\sigma_{qq}^{\text{NLO}}}{dyd^2p_T} = \frac{d\sigma_{qq}^{\text{LO}}}{dyd^2p_T} + \sum_{i=1}^5 \frac{d\sigma_{qq}^i}{dyd^2p_T}, \quad (36)$$

where the new corresponding LO and NLO contributions are cast into

$$\frac{d\sigma_{qq}^{\text{LO}}}{dyd^2p_T} = S_{\perp} \int_{\tau}^1 \frac{dz}{z^2} x_p q(x_p, \mu^2) D_{h/q}(z, \mu^2) F(k_{\perp}), \quad (37)$$

$$\frac{d\sigma_{qq}^1}{dyd^2p_T} = \frac{\alpha_s}{2\pi} C_F S_{\perp} \int_{\tau}^1 \frac{dz}{z^2} \int_{\tau/z}^1 d\xi x q(x, \mu^2) D_{h/q}(z, \mu^2) \mathcal{P}_{qq}(\xi) \ln \frac{\Lambda^2}{\mu^2} \left(F(k_{\perp}) + \frac{1}{\xi^2} F(k_{\perp}/\xi) \right), \quad (38)$$

$$\frac{d\sigma_{qq}^2}{dyd^2p_T} = 3 \frac{\alpha_s}{2\pi} C_F S_{\perp} \int_{\tau}^1 \frac{dz}{z^2} x_p q(x_p, \mu^2) D_{h/q}(z, \mu^2) \ln \frac{k_{\perp}^2}{\Lambda^2} F(k_{\perp}), \quad (39)$$

$$\frac{d\sigma_{qq}^3}{dyd^2p_T} = \frac{\alpha_s}{2\pi^2} C_F S_{\perp} \int_{\tau}^1 \frac{dz}{z^2} \int_{\tau/z}^1 d\xi \int d^2q_{1\perp} d^2q_{2\perp} x q(x, \mu^2) D_{h/q}(z, \mu^2) \frac{1 + \xi^2}{(1 - \xi)_+} \mathcal{T}_{qq}^{(1)}(\xi, q_{1\perp}, q_{2\perp}, k_{\perp}), \quad (40)$$

$$\frac{d\sigma_{qq}^4}{dyd^2p_T} = -\frac{\alpha_s}{\pi} C_F S_{\perp} \int_{\tau}^1 \frac{dz}{z^2} \int_0^1 d\xi' \int d^2q_{1\perp} x_p q(x_p, \mu^2) D_{h/q}(z, \mu^2) \frac{1 + \xi'^2}{(1 - \xi')_+} \ln \frac{(q_{1\perp} - \xi' k_{\perp})^2}{k_{\perp}^2} F(q_{1\perp}) F(k_{\perp}), \quad (41)$$

$$\begin{aligned} \frac{d\sigma_{qq}^5}{dyd^2p_T} &= \frac{2\alpha_s}{\pi^2} C_F S_{\perp} \int_{\tau}^1 \frac{dz}{z^2} \int d^2q_{1\perp} x_p q(x_p, \mu^2) D_{h/q}(z, \mu^2) \frac{1}{q_{1\perp}^2} \ln \frac{k_{\perp}^2}{q_{1\perp}^2} [F(k_{\perp} - q_{1\perp}) - \theta(k_{\perp}^2 - q_{1\perp}^2) F(k_{\perp})] \\ &+ \frac{\alpha_s}{\pi} C_F S_{\perp} \int_{\tau}^1 \frac{dz}{z^2} \int d^2q_{1\perp} x_p q(x_p, \mu^2) D_{h/q}(z, \mu^2) F(q_{1\perp}) F(k_{\perp}) \ln^2 \frac{k_{\perp}^2}{(k_{\perp} - q_{1\perp})^2} \end{aligned}$$

$$\begin{aligned}
& -\frac{2\alpha_s}{\pi^2} C_F S_\perp \int_\tau^1 \frac{dz}{z^2} \int d^2 q_{1\perp} \int d^2 q_{2\perp} x_p q(x_p, \mu^2) D_{h/q}(z, \mu^2) F(q_{1\perp}) F(q_{2\perp}) \ln \frac{k_\perp^2}{(k_\perp - q_{1\perp})^2} \\
& \times \frac{(k_\perp - q_{1\perp}) \cdot (k_\perp - q_{2\perp})}{(k_\perp - q_{1\perp})^2 (k_\perp - q_{2\perp})^2}.
\end{aligned} \tag{42}$$

In Eq. (40), we use the shorthand notation $\mathcal{T}_{qq}^{(1)}(\xi, q_{1\perp}, q_{2\perp}, k_\perp)$ defined as

$$\begin{aligned}
\mathcal{T}_{qq}^{(1)}(\xi, q_{1\perp}, q_{2\perp}, k_\perp) &= \frac{(q_{2\perp} - q_{1\perp}/\xi)^2}{(k_\perp + q_{1\perp})^2 (k_\perp/\xi + q_{2\perp})^2} F(q_{1\perp}) F(q_{2\perp}) \\
& - \frac{1}{(k_\perp + q_{1\perp})^2} \frac{\Lambda^2}{\Lambda^2 + (k_\perp + q_{1\perp})^2} F(q_{2\perp}) F(k_\perp) \\
& - \frac{1}{(k_\perp + \xi q_{2\perp})^2} \frac{\Lambda^2}{\Lambda^2 + (k_\perp/\xi + q_{2\perp})^2} F(k_\perp/\xi) F(q_{1\perp}).
\end{aligned} \tag{43}$$

The Λ dependence in σ_{qq}^1 , σ_{qq}^2 and σ_{qq}^3 completely cancels when they are summed together. Therefore, the above complete one-loop cross-section for the $q \rightarrow q$ channel is Λ -independent. This result together with the one-loop contributions from the other three channels is numerically evaluated and denoted as the ‘‘one-loop’’ results in plots.

5. Identifying the double logarithmic contribution

In the high k_\perp regime, it was found that the threshold type logarithm is one of the dominant contributions to the one-loop results. To set the stage for the resummation in the threshold regime, let us identify the double logarithm hidden in σ_{qq}^5 . Since there are partial cancellations among terms in σ^5 , we need to adopt a rather nuanced approach to analytically extract the double logarithmic term.

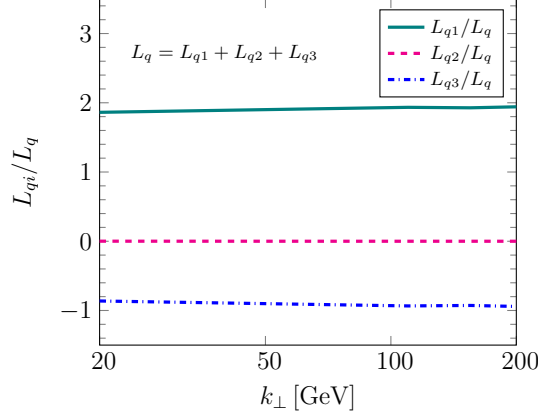


FIG. 5. Ratios of L_{q1} , L_{q2} , L_{q3} to $L_q = L_{q1} + L_{q2} + L_{q3}$.

First of all, as shown in Ref. [45], one can analytically study the high k_\perp limit of all three terms in σ^5 by using the GBW model and setting $S^{(2)}(k_\perp) = \exp(-Q_s^2 r^2/4)$ with fixed Q_s^2 . In this special case, the first term (L_{q1}) and the third term (L_{q3}) in σ^5 are proportional to $\frac{8Q_s^2}{k_\perp^4}$ and $-\frac{4Q_s^2}{k_\perp^4}$ at the large- k_\perp limit, respectively. The second term (L_{q2}) is found to be exponentially suppressed. Furthermore, as shown in Fig. 5, we have numerically evaluated σ_{qq}^5 with the rcBK solution as the input and checked that σ_{qq}^5 is roughly half of the first term in the high k_\perp limit. In addition, due to the kinematic constraint, the gluon emissions from both the initial and final state quark are required to be soft in the forward threshold limit. Thus, according to the counting rule [81, 82] for the double logarithmic contributions arising from the soft regime, the corresponding coefficient of the double logarithmic term should be $2\frac{\alpha_s}{4\pi}C_F$, since both initial state and final state gluons radiations can contribute and each of them contributes to $\frac{\alpha_s}{4\pi}C_F$.

Therefore, to analytically extract the double logarithmic term, we can decompose the θ -function term of σ_{qq}^5 as follows

$$\frac{2}{\pi} \int \frac{d^2 q_{1\perp}}{q_{1\perp}^2} \ln \frac{k_\perp^2}{q_{1\perp}^2} [\theta(\Lambda^2 - q_{1\perp}^2) - \theta(k_\perp^2 - q_{1\perp}^2)] F(k_\perp) - \frac{2}{\pi} \int \frac{d^2 q_{1\perp}}{q_{1\perp}^2} \ln \frac{k_\perp^2}{q_{1\perp}^2} \theta(\Lambda^2 - q_{1\perp}^2) F(k_\perp), \tag{44}$$

where the first term leads to a double logarithm. As discussed above, we rewrite σ_{qq}^5 as

$$\frac{d\sigma_{qq}^5}{dyd^2p_T} = \frac{d\sigma_{qq}^{5a}}{dyd^2p_T} + \frac{d\sigma_{qq}^{5b}}{dyd^2p_T}, \quad (45)$$

where,

$$\begin{aligned} \frac{d\sigma_{qq}^{5a}}{dyd^2p_T} &= -\frac{\alpha_s}{2\pi} C_F S_\perp \int_\tau^1 \frac{dz}{z^2} x_p q(x_p, \mu^2) D_{h/q}(z, \mu^2) F(k_\perp) \ln^2 \frac{k_\perp^2}{\Lambda^2}, \\ \frac{d\sigma_{qq}^{5b}}{dyd^2p_T} &= \frac{2\alpha_s}{\pi^2} C_F S_\perp \int_\tau^1 \frac{dz}{z^2} \int d^2q_{1\perp} x_p q(x_p, \mu^2) D_{h/q}(z, \mu^2) \frac{1}{q_{1\perp}^2} \ln \frac{k_\perp^2}{q_{1\perp}^2} [F(k_\perp - q_{1\perp}) - \theta(\Lambda^2 - q_{1\perp}^2) F(k_\perp)] \\ &\quad - \frac{\alpha_s}{2\pi} C_F S_\perp \int_\tau^1 \frac{dz}{z^2} x_p q(x_p, \mu^2) D_{h/q}(z, \mu^2) F(k_\perp) \ln^2 \frac{k_\perp^2}{\Lambda^2} \\ &\quad + \frac{\alpha_s}{\pi} C_F S_\perp \int_\tau^1 \frac{dz}{z^2} \int d^2q_{1\perp} x_p q(x_p, \mu^2) D_{h/q}(z, \mu^2) F(q_{1\perp}) F(k_\perp) \ln^2 \frac{k_\perp^2}{(k_\perp - q_{1\perp})^2} \\ &\quad - \frac{2\alpha_s}{\pi^2} C_F S_\perp \int_\tau^1 \frac{dz}{z^2} \int d^2q_{1\perp} \int d^2q_{2\perp} x_p q(x_p, \mu^2) D_{h/q}(z, \mu^2) F(q_{1\perp}) F(q_{2\perp}) \ln \frac{k_\perp^2}{(k_\perp - q_{1\perp})^2} \\ &\quad \times \frac{(k_\perp - q_{1\perp}) \cdot (k_\perp - q_{2\perp})}{(k_\perp - q_{1\perp})^2 (k_\perp - q_{2\perp})^2}. \end{aligned} \quad (47)$$

In the large k_\perp limit, with proper choice of Λ^2 , σ^{5a} represents the Sudakov double logarithm contribution. In the mean time, σ^{5b} is put back into the NLO hard factor as part of σ_{NLO} matching.

B. $g \rightarrow g$ channel

The computation for the $g \rightarrow g$ channel is akin to the calculation we have done above for the $q \rightarrow q$ channel. In the large N_c limit, the one loop cross-section for the $g \rightarrow g$ channel in the coordinate space reads

$$\frac{d\sigma_{gg}}{dyd^2p_T} = \frac{d\sigma_{gg}^{\text{LO}}}{dyd^2p_T} + \frac{d\sigma_{gg}^{\text{NLO}}}{dyd^2p_T} = \frac{d\sigma_{gg}^{\text{LO}}}{dyd^2p_T} + \sum_{i=a}^f \frac{d\sigma_{gg}^i}{dyd^2p_T}, \quad (48)$$

where the LO and NLO cross-sections are given by

$$\frac{d\sigma_{gg}^{\text{LO}}}{dyd^2p_T} = S_\perp \int_\tau^1 \frac{dz}{z^2} x_p g(x_p, \mu^2) D_{h/g}(z, \mu^2) \int \frac{d^2r_\perp}{(2\pi)^2} e^{-ik_\perp \cdot r_\perp} S^{(2)}(r_\perp) S^{(2)}(r_\perp), \quad (49)$$

$$\begin{aligned} \frac{d\sigma_{gg}^a}{dyd^2p_T} &= \frac{\alpha_s}{2\pi} S_\perp N_c \int_\tau^1 \frac{dz}{z^2} \int_{\tau/z}^1 d\xi x g(x, \mu^2) D_{h/g}(z, \mu^2) \mathcal{P}_{gg}(\xi) \int \frac{d^2r_\perp}{(2\pi)^2} S^{(2)}(r_\perp) S^{(2)}(r_\perp) \\ &\quad \times \left(e^{-ik_\perp \cdot r_\perp} + \frac{1}{\xi^2} e^{-i\frac{1}{\xi} k_\perp \cdot r_\perp} \right) \ln \frac{c_0^2}{r_\perp^2 \mu^2}, \end{aligned} \quad (50)$$

$$\frac{d\sigma_{gg}^b}{dyd^2p_T} = -\frac{\alpha_s}{2\pi} 4\beta_0 S_\perp N_c \int_\tau^1 \frac{dz}{z^2} x_p g(x_p, \mu^2) D_{h/g}(z, \mu^2) \int \frac{d^2r_\perp}{(2\pi)^2} e^{-ik_\perp \cdot r_\perp} S^{(2)}(r_\perp) S^{(2)}(r_\perp) \ln \frac{c_0^2}{r_\perp^2 k_\perp^2}, \quad (51)$$

$$\begin{aligned} \frac{d\sigma_{gg}^c}{dyd^2p_T} &= 8\pi S_\perp N_f T_R \frac{\alpha_s}{2\pi} \int_\tau^1 \frac{dz}{z^2} x_p g(x_p, \mu^2) D_{h/g}(z, \mu^2) \int \frac{d^2u_\perp d^2v_\perp}{(2\pi)^4} e^{-ik_\perp \cdot v_\perp} S^{(2)}(u_\perp) S^{(2)}(v_\perp) \\ &\quad \times \int_0^1 d\xi' [\xi'^2 + (1 - \xi')^2] \left[\frac{e^{-i\xi' k_\perp \cdot (u_\perp - v_\perp)}}{(u_\perp - v_\perp)^2} - \delta^2(u_\perp - v_\perp) \int d^2r'_\perp \frac{e^{ik_\perp \cdot r'_\perp}}{r'^2_\perp} \right], \end{aligned} \quad (52)$$

$$\begin{aligned} \frac{d\sigma_{gg}^d}{dyd^2p_T} &= -16\pi S_\perp N_c \frac{\alpha_s}{2\pi} \int_\tau^1 \frac{dz}{z^2} \int_{\tau/z}^1 d\xi x g(x, \mu^2) D_{h/g}(z, \mu^2) \int \frac{d^2u_\perp d^2v_\perp}{(2\pi)^4} e^{-ik_\perp \cdot (u_\perp - v_\perp)} e^{-i\frac{1}{\xi} k_\perp \cdot v_\perp} \\ &\quad \times S^{(2)}(u_\perp) S^{(2)}(v_\perp) S^{(2)}(u_\perp - v_\perp) \frac{[1 - \xi(1 - \xi)]^2}{(1 - \xi)_+} \frac{1}{\xi^2} \frac{(u_\perp - v_\perp) \cdot v_\perp}{(u_\perp - v_\perp)^2 v_\perp^2}, \end{aligned} \quad (53)$$

$$\frac{d\sigma_{gg}^e}{dyd^2p_T} = 16\pi S_\perp N_c \frac{\alpha_s}{2\pi} \int_\tau^1 \frac{dz}{z^2} x_p g(x_p, \mu^2) D_{h/g}(z, \mu^2) \int \frac{d^2u_\perp d^2v_\perp}{(2\pi)^4} S^{(2)}(u_\perp) S^{(2)}(v_\perp) S^{(2)}(u_\perp - v_\perp)$$

$$\times e^{-ik_{\perp} \cdot (u_{\perp} - v_{\perp})} \int_0^1 d\xi' \left[\frac{\xi'}{(1-\xi')_+} + \frac{\xi'(1-\xi')}{2} \right] \left[\frac{e^{-i\xi' k_{\perp} \cdot v_{\perp}}}{v_{\perp}^2} - \delta^2(v_{\perp}) \int d^2 r'_{\perp} \frac{e^{ik_{\perp} \cdot r'_{\perp}}}{r_{\perp}^{\prime 2}} \right], \quad (54)$$

$$\begin{aligned} \frac{d\sigma_{gg}^f}{dyd^2p_T} &= \frac{\alpha_s}{\pi^2} S_{\perp} N_c \int_{\tau}^1 \frac{dz}{z^2} x_p g(x_p, \mu^2) D_{h/g}(z, \mu^2) \int \frac{d^2 u_{\perp} d^2 v_{\perp}}{(2\pi)^2} e^{-ik_{\perp} \cdot (u_{\perp} - v_{\perp})} [S^{(2)}(u_{\perp}) S^{(2)}(v_{\perp}) - S^{(2)}(u_{\perp} - v_{\perp})] \\ &\times S^{(2)}(u_{\perp} - v_{\perp}) \left[\frac{1}{u_{\perp}^2} \ln \frac{k_{\perp}^2 u_{\perp}^2}{c_0^2} + \frac{1}{v_{\perp}^2} \ln \frac{k_{\perp}^2 v_{\perp}^2}{c_0^2} - \frac{2u_{\perp} \cdot v_{\perp}}{u_{\perp}^2 v_{\perp}^2} \ln \frac{k_{\perp}^2 |u_{\perp}| |v_{\perp}|}{c_0^2} \right], \end{aligned} \quad (55)$$

where $\mathcal{P}_{gg}(\xi) = 2 \left[\frac{\xi}{(1-\xi)_+} + \frac{1-\xi}{\xi} + \xi(1-\xi) \right] + 2\beta_0 \delta(1-\xi)$ and $\beta_0 = \frac{11}{12} - \frac{2N_f T_R}{6N_c}$.

Due to the same reasons discussed in the last subsection, we also need to Fourier transform the above equations to the momentum space analytically. Most of the techniques have been presented in the last subsection except for the following one

$$\begin{aligned} \int \frac{d^2 r_{\perp}}{(2\pi)^2} e^{-ik_{\perp} \cdot r_{\perp}} S^{(2)}(r_{\perp}) S^{(2)}(r_{\perp}) &= \int \frac{d^2 r_{\perp}}{(2\pi)^2} e^{-ik_{\perp} \cdot r_{\perp}} \int d^2 q_{1\perp} e^{iq_{1\perp} \cdot r_{\perp}} F(q_{1\perp}) \int d^2 q_{2\perp} e^{iq_{2\perp} \cdot r_{\perp}} F(q_{2\perp}) \\ &= \int d^2 q_{1\perp} F(q_{1\perp}) F(k_{\perp} - q_{1\perp}), \end{aligned} \quad (56)$$

which transforms the gluon dipole into the momentum space. In addition, the σ_{gg}^f term can be written as

$$\frac{d\sigma_{gg}^f}{dyd^2p_T} = \int_{\tau}^1 \frac{dz}{z^2} x_p g(x_p, \mu^2) D_{h/g}(z, \mu^2) [L_{g1}(k_{\perp}) + L_{g2}(k_{\perp}) + L_{g3}(k_{\perp})], \quad (57)$$

$$L_{g1}(k_{\perp}) = -\frac{\alpha_s N_c}{2\pi^2} S_{\perp} \int \frac{d^2 r_{\perp}}{2\pi} e^{-ik_{\perp} \cdot r_{\perp}} S^{(2)}(r_{\perp}) S^{(2)}(r_{\perp}) \ln^2 \frac{k_{\perp}^2 r_{\perp}^2}{c_0^2}, \quad (58)$$

$$L_{g2}(k_{\perp}) = \frac{\alpha_s N_c}{\pi} S_{\perp} \int d^2 q_{1\perp} d^2 q_{2\perp} F(k_{\perp} - q_{1\perp} - q_{2\perp}) F(k_{\perp} - q_{2\perp}) F(q_{2\perp}) \ln^2 \frac{k_{\perp}^2}{q_{1\perp}^2}, \quad (59)$$

$$L_{g3}(k_{\perp}) = -\frac{2\alpha_s N_c}{\pi^2} S_{\perp} \int d^2 q_{1\perp} d^2 q_{2\perp} d^2 q_{3\perp} F(q_{3\perp}) F(k_{\perp} - q_{2\perp} - q_{3\perp}) F(k_{\perp} - q_{1\perp} - q_{3\perp}) \frac{q_{1\perp} \cdot q_{2\perp}}{q_{1\perp}^2 q_{2\perp}^2} \ln \frac{k_{\perp}^2}{q_{1\perp}^2}. \quad (60)$$

Using the same procedure laid out in the $q \rightarrow q$ channel, we can convert the above cross-section into the expressions in the momentum space as follows

$$\frac{d\sigma_{gg}}{dyd^2p_T} = \frac{d\sigma_{gg}^{\text{LO}}}{dyd^2p_T} + \frac{d\sigma_{gg}^{\text{NLO}}}{dyd^2p_T} = \frac{d\sigma_{gg}^{\text{LO}}}{dyd^2p_T} + \sum_{i=1}^6 \frac{d\sigma_{gg}^i}{dyd^2p_T}, \quad (61)$$

with the LO and NLO cross-sections defined as

$$\frac{d\sigma_{gg}^{\text{LO}}}{dyd^2p_T} = S_{\perp} \int_{\tau}^1 \frac{dz}{z^2} x_p g(x_p, \mu^2) D_{h/g}(z, \mu^2) \int d^2 q_{1\perp} F(q_{1\perp}) F(k_{\perp} - q_{1\perp}), \quad (62)$$

$$\begin{aligned} \frac{d\sigma_{gg}^1}{dyd^2p_T} &= \frac{\alpha_s}{2\pi} N_c S_{\perp} \int_{\tau}^1 \frac{dz}{z^2} \int_{\tau/z}^1 d\xi \int d^2 q_{1\perp} x g(x, \mu^2) D_{h/g}(z, \mu^2) \mathcal{P}_{gg}(\xi) \\ &\times \ln \frac{\Lambda^2}{\mu^2} \left[F(k_{\perp} - q_{1\perp}) + \frac{1}{\xi^2} F(k_{\perp}/\xi - q_{1\perp}) \right] F(q_{1\perp}), \end{aligned} \quad (63)$$

$$\frac{d\sigma_{gg}^2}{dyd^2p_T} = \frac{\alpha_s}{2\pi} N_c S_{\perp} 4\beta_0 \int_{\tau}^1 \frac{dz}{z^2} \int d^2 q_{1\perp} x g(x, \mu^2) D_{h/g}(z, \mu^2) F(k_{\perp} - q_{1\perp}) F(q_{1\perp}) \ln \frac{k_{\perp}^2}{\Lambda^2}, \quad (64)$$

$$\begin{aligned} \frac{d\sigma_{gg}^3}{dyd^2p_T} &= \frac{\alpha_s}{\pi^2} N_c S_{\perp} \int_{\tau}^1 \frac{dz}{z^2} \int_{\tau/z}^1 d\xi \int d^2 q_{1\perp} d^2 q_{2\perp} d^2 q_{3\perp} x g(x, \mu^2) D_{h/g}(z, \mu^2) \frac{[1-\xi(1-\xi)]^2}{\xi(1-\xi)_+} \\ &\times \mathcal{T}_{gg}^{(1)}(\xi, q_{1\perp}, q_{2\perp}, q_{3\perp}, k_{\perp}), \end{aligned} \quad (65)$$

$$\begin{aligned} \frac{d\sigma_{gg}^4}{dyd^2p_T} &= -2N_f T_R \frac{\alpha_s}{2\pi} S_{\perp} \int_{\tau}^1 \frac{dz}{z^2} \int_0^1 d\xi' d^2 q_{1\perp} x_p g(x_p, \mu^2) D_{h/g}(z, \mu^2) [\xi'^2 + (1-\xi')^2] \\ &\times F(q_{1\perp}) F(k_{\perp} - q_{1\perp}) \ln \frac{(q_{1\perp} - \xi' k_{\perp})^2}{k_{\perp}^2}, \end{aligned} \quad (66)$$

$$\frac{d\sigma_{gg}^5}{dyd^2p_T} = -4N_c \frac{\alpha_s}{2\pi} S_\perp \int_\tau^1 \frac{dz}{z^2} \int_0^1 d\xi' d^2q_{1\perp} d^2q_{2\perp} x_p g(x_p, \mu^2) D_{h/g}(z, \mu^2) \left[\frac{\xi'}{(1-\xi')_+} + \frac{1}{2}\xi'(1-\xi') \right] F(q_{1\perp})F(q_{2\perp})F(k_\perp - q_{1\perp}) \ln \frac{(q_{1\perp} + q_{2\perp} - \xi'k_\perp)^2}{k_\perp^2}, \quad (67)$$

$$\begin{aligned} \frac{d\sigma_{gg}^6}{dyd^2p_T} &= \frac{2\alpha_s}{\pi^2} N_c S_\perp \int_\tau^1 \frac{dz}{z^2} \int d^2q_{1\perp} \int d^2q_{2\perp} x_p g(x_p, \mu^2) D_{h/q}(z, \mu^2) \frac{1}{q_{2\perp}^2} \ln \frac{k_\perp^2}{q_{2\perp}^2} F(k_\perp - q_{1\perp}) \\ &\quad \times [F(q_{1\perp} + q_{2\perp}) - \theta(k_\perp^2 - q_{2\perp}^2)F(q_{1\perp})] \\ &+ \frac{\alpha_s}{\pi} N_c S_\perp \int_\tau^1 \frac{dz}{z^2} \int d^2q_{1\perp} \int d^2q_{2\perp} x_p g(x_p, \mu^2) D_{h/q}(z, \mu^2) F(q_{1\perp})F(q_{2\perp})F(k_\perp - q_{2\perp}) \\ &\quad \times \ln^2 \frac{k_\perp^2}{(q_{1\perp} + q_{2\perp} - k_\perp)^2} \\ &- \frac{2\alpha_s}{\pi^2} N_c S_\perp \int_\tau^1 \frac{dz}{z^2} \int d^2q_{1\perp} \int d^2q_{2\perp} \int d^2q_{3\perp} x_p g(x_p, \mu^2) D_{h/q}(z, \mu^2) F(q_{1\perp})F(q_{2\perp})F(q_{3\perp}) \\ &\quad \times \frac{(k_\perp - q_{1\perp} + q_{3\perp}) \cdot (k_\perp - q_{2\perp} + q_{3\perp})}{(k_\perp - q_{1\perp} + q_{3\perp})^2 (k_\perp - q_{2\perp} + q_{3\perp})^2} \ln \frac{k_\perp^2}{(k_\perp - q_{1\perp} + q_{3\perp})^2}, \end{aligned} \quad (68)$$

where $\mathcal{P}_{gg}(\xi) = 2 \left[\frac{\xi}{(1-\xi)_+} + \frac{1-\xi}{\xi} + \xi(1-\xi) \right] + \left(\frac{11}{6} - \frac{2N_f T_R}{3N_c} \right) \delta(1-\xi)$ and

$$\begin{aligned} \mathcal{T}_{gg}^{(1)}(\xi, q_{1\perp}, q_{2\perp}, q_{3\perp}, k_\perp) &= \frac{1}{\xi^2} \frac{[(1-\xi)q_{1\perp} + q_{3\perp} - \xi q_{2\perp}]^2}{(q_{1\perp} + q_{3\perp} - k_\perp)^2 (q_{1\perp} + q_{2\perp} - k_\perp/\xi)^2} F(q_{1\perp})F(q_{2\perp})F(q_{3\perp}) \\ &\quad - \frac{1}{(q_{1\perp} + q_{3\perp} - k_\perp)^2} \frac{\Lambda^2}{\Lambda^2 + (q_{1\perp} + q_{3\perp} - k_\perp)^2} F(k_\perp - q_{3\perp})F(q_{2\perp})F(q_{3\perp}) \\ &\quad - \frac{1}{\xi^2} \frac{1}{(q_{1\perp} + q_{2\perp} - k_\perp/\xi)^2} \frac{\Lambda^2}{\Lambda^2 + (q_{1\perp} + q_{2\perp} - k_\perp/\xi)^2} F(k_\perp/\xi - q_{2\perp})F(q_{2\perp})F(q_{3\perp}). \end{aligned} \quad (69)$$

Similar to the case for $q \rightarrow q$ channel, the Λ -dependence in σ_{gg}^1 , σ_{gg}^2 and σ_{gg}^3 cancels when they are summed. We obtain the $\ln \frac{\Lambda^2}{\mu^2}$ logarithm in σ_{gg}^1 associated with the collinear divergence and the single Sudakov logarithm in terms of $\ln \frac{k_\perp^2}{\Lambda^2}$ in σ_{gg}^2 . The resummation of these logarithms will be presented in the next section.

Furthermore, we can extract the Sudakov double logarithm from σ_{gg}^6 . We have numerically checked that the ratio of $L_g \equiv L_{g1} + L_{g2} + L_{g3}$ to $L_q \equiv L_{q1} + L_{q2} + L_{q3}$ is about 2 at large k_\perp limit. Therefore, we identify the coefficient of the double logarithm as $\frac{\alpha_s}{2\pi} N_c$, which is twice as large as that in the $q \rightarrow q$ channel at the large N_c limit. Similar to the quark case, according to the counting rule, the corresponding coefficient for the $g \rightarrow g$ channel double logarithm is $2 \times \frac{\alpha_s N_c}{4\pi}$, since both initial state and final state gluon emissions contribute. Therefore, the obtained coefficient also agrees with the counting rule in Refs. [81, 82]. By decomposing the theta function the same way discussed in the last subsection, we have

$$\frac{d\sigma_{gg}^6}{dyd^2p_T} = \frac{d\sigma_{gg}^{6a}}{dyd^2p_T} + \frac{d\sigma_{gg}^{6b}}{dyd^2p_T}, \quad (70)$$

where

$$\begin{aligned} \frac{d\sigma_{gg}^{6a}}{dyd^2p_T} &= -\frac{\alpha_s}{2\pi} N_c S_\perp \int_\tau^1 \frac{dz}{z^2} x_p g(x_p, \mu^2) D_{h/q}(z, \mu^2) \ln^2 \frac{k_\perp^2}{\Lambda^2} \int d^2q_{1\perp} F(k_\perp - q_{1\perp})F(q_{1\perp}), \\ \frac{d\sigma_{gg}^{6b}}{dyd^2p_T} &= \frac{2\alpha_s}{\pi^2} N_c S_\perp \int_\tau^1 \frac{dz}{z^2} \int d^2q_{1\perp} \int d^2q_{2\perp} x_p g(x_p, \mu^2) D_{h/q}(z, \mu^2) \frac{1}{q_{2\perp}^2} \ln \frac{k_\perp^2}{q_{2\perp}^2} F(k_\perp - q_{1\perp}) \\ &\quad \times [F(q_{1\perp} + q_{2\perp}) - \theta(\Lambda^2 - q_{2\perp}^2)F(q_{1\perp})] \\ &- \frac{\alpha_s}{2\pi} N_c S_\perp \int_\tau^1 \frac{dz}{z^2} x_p g(x_p, \mu^2) D_{h/q}(z, \mu^2) \ln^2 \frac{k_\perp^2}{\Lambda^2} \int d^2q_{1\perp} F(k_\perp - q_{1\perp})F(q_{1\perp}) \\ &+ \frac{\alpha_s}{\pi} N_c S_\perp \int_\tau^1 \frac{dz}{z^2} \int d^2q_{1\perp} \int d^2q_{2\perp} x_p g(x_p, \mu^2) D_{h/q}(z, \mu^2) F(q_{1\perp})F(q_{2\perp})F(k_\perp - q_{2\perp}) \\ &\quad \times \ln^2 \frac{k_\perp^2}{(q_{1\perp} + q_{2\perp} - k_\perp)^2} \end{aligned} \quad (71)$$

$$\begin{aligned}
& -\frac{2\alpha_s}{\pi^2} N_c S_\perp \int_\tau^1 \frac{dz}{z^2} \int d^2 q_{1\perp} \int d^2 q_{2\perp} \int d^2 q_{3\perp} x_p g(x_p, \mu^2) D_{h/q}(z, \mu^2) F(q_{1\perp}) F(q_{2\perp}) F(q_{3\perp}) \\
& \times \frac{(k_\perp - q_{1\perp} + q_{3\perp}) \cdot (k_\perp - q_{2\perp} + q_{3\perp})}{(k_\perp - q_{1\perp} + q_{3\perp})^2 (k_\perp - q_{2\perp} + q_{3\perp})^2} \ln \frac{k_\perp^2}{(k_\perp - q_{1\perp} + q_{3\perp})^2}.
\end{aligned} \tag{72}$$

σ_{gg}^{6a} will be resummed in the Sudakov resummation and σ_{gg}^{6b} contributes to the finite NLO corrections.

C. $q \rightarrow g$ channel

For the $q \rightarrow g$ channel, there is no LO contribution. We have cross-section in the coordinate space as

$$\frac{d\sigma_{gq}}{dyd^2p_T} = \frac{d\sigma_{gq}^{\text{NLO}}}{dyd^2p_T} = \sum_{i=a}^c \frac{d\sigma_{gq}^i}{dyd^2p_T}, \tag{73}$$

where,

$$\begin{aligned}
\frac{d\sigma_{gq}^a}{dyd^2p_T} &= \frac{\alpha_s}{2\pi} S_\perp C_F \int_\tau^1 \frac{dz}{z^2} \int_{\tau/z}^1 d\xi x q(x, \mu^2) D_{h/g}(z, \mu^2) \int \frac{d^2 r_\perp}{(2\pi)^2} e^{-i\frac{1}{\xi} k_\perp \cdot r_\perp} S^{(2)}(r_\perp) \\
&\times \frac{1}{\xi^2} \mathcal{P}_{gq}(\xi) \ln \frac{c_0^2}{r_\perp^2 \mu^2},
\end{aligned} \tag{74}$$

$$\begin{aligned}
\frac{d\sigma_{gq}^b}{dyd^2p_T} &= \frac{\alpha_s}{2\pi} S_\perp C_F \int_\tau^1 \frac{dz}{z^2} \int_{\tau/z}^1 d\xi x q(x, \mu^2) D_{h/g}(z, \mu^2) \int \frac{d^2 r_\perp}{(2\pi)^2} e^{-ik_\perp \cdot r_\perp} S^{(2)}(r_\perp) S^{(2)}(r_\perp) \\
&\times \mathcal{P}_{gq}(\xi) \ln \frac{c_0^2}{r_\perp^2 \mu^2},
\end{aligned} \tag{75}$$

$$\begin{aligned}
\frac{d\sigma_{gq}^c}{dyd^2p_T} &= 8\pi S_\perp C_F \frac{\alpha_s}{2\pi} \int_\tau^1 \frac{dz}{z^2} \int_{\tau/z}^1 d\xi x q(x, \mu^2) D_{h/g}(z, \mu^2) \int \frac{d^2 u_\perp d^2 v_\perp}{(2\pi)^4} e^{-i\frac{1}{\xi} k_\perp \cdot (u_\perp - v_\perp)} e^{-ik_\perp \cdot v_\perp} \\
&\times S^{(2)}(u_\perp) S^{(2)}(v_\perp) \mathcal{P}_{gq}(\xi) \frac{1}{\xi} \frac{(u_\perp - v_\perp) \cdot v_\perp}{(u_\perp - v_\perp)^2 v_\perp^2},
\end{aligned} \tag{76}$$

where $\mathcal{P}_{gq}(\xi) = \frac{1}{\xi} [1 + (1 - \xi)^2]$.

After the Fourier transform, we obtain

$$\frac{d\sigma_{gq}}{dyd^2p_T} = \frac{d\sigma_{gq}^{\text{NLO}}}{dyd^2p_T} = \sum_{i=1}^3 \frac{d\sigma_{gq}^i}{dyd^2p_T}, \tag{77}$$

where

$$\frac{d\sigma_{gq}^1}{dyd^2p_T} = \frac{\alpha_s}{2\pi} C_F S_\perp \int_\tau^1 \frac{dz}{z^2} \int_{\tau/z}^1 d\xi \int d^2 q_{1\perp} x q(x, \mu^2) D_{h/g}(z, \mu^2) \mathcal{P}_{gq}(\xi) \ln \frac{\Lambda^2}{\mu^2} F(q_{1\perp}) F(k_\perp - q_{1\perp}), \tag{78}$$

$$\frac{d\sigma_{gq}^2}{dyd^2p_T} = \frac{\alpha_s}{2\pi} C_F S_\perp \int_\tau^1 \frac{dz}{z^2} \int_{\tau/z}^1 d\xi x q(x, \mu^2) D_{h/g}(z, \mu^2) \mathcal{P}_{gq}(\xi) \ln \frac{\Lambda^2}{\mu^2} \frac{1}{\xi^2} F(k_\perp/\xi), \tag{79}$$

$$\frac{d\sigma_{gq}^3}{dyd^2p_T} = \frac{\alpha_s}{2\pi^2} C_F S_\perp \int_\tau^1 \frac{dz}{z^2} \int_{\tau/z}^1 d\xi \int d^2 q_{1\perp} \int d^2 q_{2\perp} x q(x, \mu^2) D_{h/g}(z, \mu^2) \mathcal{P}_{gq}(\xi) \mathcal{T}_{gq}^{(1)}(\xi, q_{1\perp}, q_{2\perp}, k_\perp), \tag{80}$$

with

$$\begin{aligned}
\mathcal{T}_{gq}^{(1)}(\xi, q_{1\perp}, q_{2\perp}, k_\perp) &= \left(\frac{k_\perp - q_{1\perp} - q_{2\perp}}{(k_\perp - q_{1\perp} - q_{2\perp})^2} - \frac{k_\perp - \xi q_{2\perp}}{(k_\perp - \xi q_{2\perp})^2} \right)^2 F(q_{1\perp}) F(q_{2\perp}) \\
&\quad - \frac{\Lambda^2}{\Lambda^2 + (k_\perp - q_{1\perp} - q_{2\perp})^2} \frac{1}{(k_\perp - q_{1\perp} - q_{2\perp})^2} F(q_{2\perp}) F(k_\perp - q_{2\perp}) \\
&\quad - \frac{\Lambda^2}{\Lambda^2 + (k_\perp/\xi - q_{2\perp})^2} \frac{1}{(k_\perp - \xi q_{2\perp})^2} F(q_{1\perp}) F(k_\perp/\xi).
\end{aligned} \tag{81}$$

For this channel, we obtain the $\ln \frac{\Lambda^2}{\mu^2}$ logarithm which is associated with the collinear divergence in σ_{gq}^1 and σ_{gq}^2 . The Sudakov double logarithm ($\ln^2 \frac{k_\perp^2}{\Lambda^2}$) and single logarithm ($\ln \frac{k_\perp^2}{\Lambda^2}$) do not appear in the off-diagonal channels.

D. $g \rightarrow q$ channel

To complete the calculation for all the channels, we should also compute the $g \rightarrow q\bar{q}$ channel. The cross-section of the $g \rightarrow q$ channel in the coordinate space is

$$\frac{d\sigma_{gg}}{dyd^2p_T} = \sum_{i=a}^c \frac{d\sigma_{gg}^i}{dyd^2p_T}, \quad (82)$$

where

$$\begin{aligned} \frac{d\sigma_{gg}^a}{dyd^2p_T} &= \frac{\alpha_s}{2\pi} S_\perp T_R \int_\tau^1 \frac{dz}{z^2} \int_{\tau/z}^1 d\xi xg(x, \mu^2) D_{h/q}(z, \mu^2) \int \frac{d^2r_\perp}{(2\pi)^2} e^{-ik_\perp \cdot r_\perp} S^{(2)}(r_\perp) \\ &\quad \times \mathcal{P}_{qg}(\xi) \left[\ln \frac{c_0^2}{r_\perp^2 \mu^2} - 1 \right], \end{aligned} \quad (83)$$

$$\begin{aligned} \frac{d\sigma_{gg}^b}{dyd^2p_T} &= \frac{\alpha_s}{2\pi} S_\perp T_R \int_\tau^1 \frac{dz}{z^2} \int_{\tau/z}^1 d\xi xg(x, \mu^2) D_{h/q}(z, \mu^2) \int \frac{d^2r_\perp}{(2\pi)^2} e^{-i\frac{1}{\xi} k_\perp \cdot r_\perp} S^{(2)}(r_\perp) S^{(2)}(r_\perp) \\ &\quad \times \frac{1}{\xi^2} \mathcal{P}_{qg}(\xi) \left[\ln \frac{c_0^2}{r_\perp^2 \mu^2} - 1 \right], \end{aligned} \quad (84)$$

$$\begin{aligned} \frac{d\sigma_{gg}^c}{dyd^2p_T} &= 8\pi S_\perp T_R \frac{\alpha_s}{2\pi} \int_\tau^1 \frac{dz}{z^2} \int_{\tau/z}^1 d\xi xg(x, \mu^2) D_{h/q}(z, \mu^2) \int \frac{d^2u_\perp d^2v_\perp}{(2\pi)^4} e^{-ik_\perp \cdot (u_\perp - v_\perp) - i\frac{1}{\xi} k_\perp \cdot v_\perp} \\ &\quad \times \frac{1}{\xi} \mathcal{P}_{qg}(\xi) S^{(2)}(u_\perp) S^{(2)}(v_\perp) \frac{(u_\perp - v_\perp) \cdot v_\perp}{(u_\perp - v_\perp)^2 v_\perp^2}. \end{aligned} \quad (85)$$

Here $\mathcal{P}_{qg}(\xi) = \xi^2 + (1 - \xi)^2$. The cross-section in the momentum space reads

$$\frac{d\sigma_{gg}}{dyd^2p_T} = \sum_{i=1}^5 \frac{d\sigma_{gg}^i}{dyd^2p_T}, \quad (86)$$

with

$$\frac{d\sigma_{gg}^1}{dyd^2p_T} = \frac{\alpha_s}{4\pi} S_\perp \int_\tau^1 \frac{dz}{z^2} \int_{\tau/z}^1 d\xi xg(x, \mu^2) D_{h/q}(z, \mu^2) \mathcal{P}_{qg}(\xi) \ln \frac{\Lambda^2}{\mu^2} F(k_\perp), \quad (87)$$

$$\frac{d\sigma_{gg}^2}{dyd^2p_T} = \frac{\alpha_s}{4\pi} S_\perp \int_\tau^1 \frac{dz}{z^2} \int_{\tau/z}^1 d\xi \int d^2q_{1\perp} xg(x, \mu^2) D_{h/q}(z, \mu^2) \frac{1}{\xi^2} \mathcal{P}_{qg}(\xi) \ln \frac{\Lambda^2}{\mu^2} F(q_{1\perp}) F(k_\perp/\xi - q_{1\perp}), \quad (88)$$

$$\frac{d\sigma_{gg}^3}{dyd^2p_T} = -\frac{\alpha_s}{4\pi} S_\perp \int_\tau^1 \frac{dz}{z^2} \int_{\tau/z}^1 d\xi xg(x, \mu^2) D_{h/q}(z, \mu^2) \mathcal{P}_{qg}(\xi) F(k_\perp), \quad (89)$$

$$\frac{d\sigma_{gg}^4}{dyd^2p_T} = -\frac{\alpha_s}{4\pi} S_\perp \int_\tau^1 \frac{dz}{z^2} \int_{\tau/z}^1 d\xi \int d^2q_{1\perp} xg(x, \mu^2) D_{h/q}(z, \mu^2) \frac{1}{\xi^2} \mathcal{P}_{qg}(\xi) F(q_{1\perp}) F(k_\perp/\xi - q_{1\perp}), \quad (90)$$

$$\frac{d\sigma_{gg}^5}{dyd^2p_T} = \frac{\alpha_s}{4\pi^2} S_\perp \int_\tau^1 \frac{dz}{z^2} \int_{\tau/z}^1 d\xi \int d^2q_{1\perp} \int d^2q_{2\perp} xg(x, \mu^2) D_{h/q}(z, \mu^2) \mathcal{P}_{qg}(\xi) \mathcal{T}_{qg}^{(1)}(\xi, q_{1\perp}, q_{2\perp}, k_\perp), \quad (91)$$

where

$$\begin{aligned} \mathcal{T}_{qg}^{(1)}(\xi, q_{1\perp}, q_{2\perp}, k_\perp) &= \left(\frac{k_\perp - \xi q_{1\perp} - \xi q_{2\perp}}{(k_\perp - \xi q_{1\perp} - \xi q_{2\perp})^2} - \frac{k_\perp - q_{2\perp}}{(k_\perp - q_{2\perp})^2} \right)^2 F(q_{1\perp}) F(q_{2\perp}) \\ &\quad - \frac{1}{(k_\perp - \xi q_{1\perp} - \xi q_{2\perp})^2} \frac{\Lambda^2}{\Lambda^2 + (k_\perp/\xi - q_{1\perp} - q_{2\perp})^2} F(q_{2\perp}) F(k_\perp/\xi - q_{2\perp}) \\ &\quad - \frac{1}{(k_\perp - q_{2\perp})^2} \frac{\Lambda^2}{\Lambda^2 + (k_\perp - q_{2\perp})^2} F(q_{1\perp}) F(k_\perp). \end{aligned} \quad (92)$$

Again, we obtain the $\ln \frac{\Lambda^2}{\mu^2}$ logarithm in σ_{gg}^1 and σ_{gg}^2 which will be resummed making use of the DGLAP evolution equation. The soft logarithms do not contribute in the off-diagonal channels.

II. KINEMATICS NEAR THE THRESHOLD

In this section, we discuss the kinematics of the inclusive hadron production in forward pA collisions and illustrate the kinematic region where the threshold resummation becomes important. The longitudinal momentum fraction of the produced hadron τ , which is defined as $\tau = \frac{p_T}{\sqrt{s}}e^y$, is the key physical quantity. It can also be written as $\tau = xz\xi$, where x is the momentum fraction carried by the projectile parton, z is the momentum fraction carried by the final state hadron and ξ is the momentum fraction in the partonic splitting. We show the plots of τ as a function of y and p_T at the RHIC and LHC energies in Fig. 6.

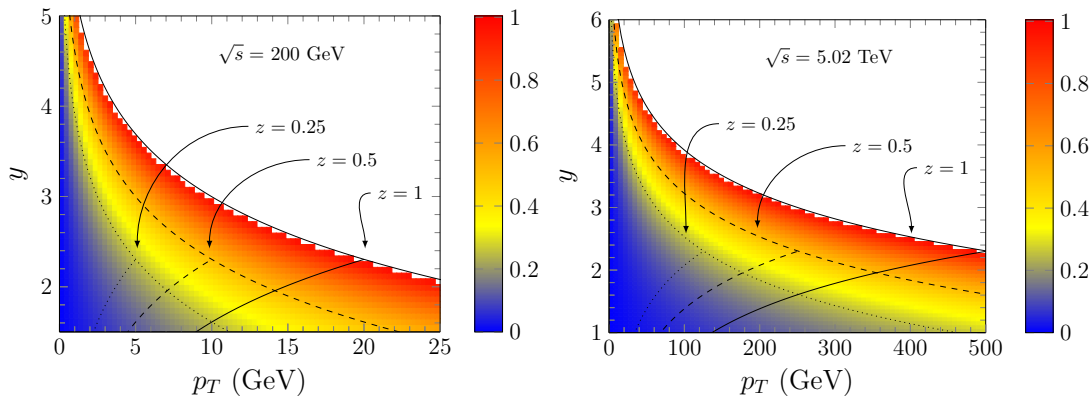


FIG. 6. The plots of τ as a function of y and p_T at two different collision energies (\sqrt{s}). Various values of τ are represented by different colors as shown above. The rapidity y is defined in the center of the mass frame of the two colliding hadrons.

These two plots illustrate the allowed ranges of p_T at fixed rapidity y at both RHIC and the LHC energies. The upper-most solid line in Fig. 6 represents the boundary determined by the kinematic threshold, which is given by $\tau = \frac{p_T}{\sqrt{s}}e^y = 1$ and $z = 1$. The region above this boundary is forbidden by kinematics and it implies that the rapidity or p_T of the produced hadron can not be exceedingly large. When τ is near 1, x , z and ξ are all forced to be near 1, namely the kinematic threshold. The region in red and yellow in Fig. 6 indicates where the threshold resummation is expected to be important.

Meanwhile, the dilute-dense factorization used in the NLO hadron production calculation assumes that the small- x gluon in the nuclear target is dense enough and the CGC formalism can apply. Since the small- x gluon distribution and the dipole scattering amplitude usually start from the initial condition at $x_g = 0.01$ and evolve to smaller x regime, in order to justify the small- x assumptions used in the CGC formalism, we usually need to require $x_g = \frac{p_T}{z\sqrt{s}}e^{-y} \leq 0.01$ with x_g being the momentum fraction of the target gluon. The lower-most solid line is corresponding to the boundary given by $x_g \leq 0.01$ beyond which the dilute-dense factorization no longer applies. It is interesting to note that these two boundaries always intersect at $y_0 = \frac{1}{2} \ln 100 = 2.3$. This implies that for rapidities $y \geq y_0$, the gluon inside the target hadron is always located in the small- x regime. Furthermore, in the regime where $0 < y < y_0$, the CGC calculation should only be applied to the low p_T region. Additional numerical results are presented in the end and they also indicate that the CGC calculation is expected to break down in the high p_T region when the rapidity y is not forward enough.

It is worth noting that these two boundaries moves to the left at smaller value of z when the kinematic constraint requires $x_p \equiv \frac{p_T}{z\sqrt{s}}e^y = \xi x \leq 1$. The dashed and dotted lines represent the resulting boundaries at $z = 0.5$ and $z = 0.25$, respectively. In these cases, x and ξ can approach 1 with fixed values of z . Clearly, due to the initial state soft gluon radiation, both the Sudakov resummation and the collinear threshold resummation with respect to the PDF must be taken into account even when z is not large. Similarly, one can imagine that the Sudakov resummation and the collinear threshold resummation with respect to the FF become important when ξ and z are kept large while x is far away from 1.

Throughout this paper except the discussion in Sec. XC, we set the small- x gluon distribution to be 0 when x_g is larger than 0.01. This prescription, referred as the “fixed boundary condition”, effectively removes all the contribution from the kinematic regime where dilute-dense factorization does not apply. In Sec. XC, we also present another prescription which freezes $\mathcal{F}^{x_g}(k_\perp)$ at $x_g = 0.01$. The numerical results show little difference between these two prescriptions at small- p_T . While the visible difference between these two prescriptions can be found for the large p_T events measured in the middle rapidity region, we expect that this kinematic region is no longer within the applicable regime of the CGC formalism and the dilute-dense factorization.

III. THE RESUMMATION OF THE COLLINEAR LOGARITHMS

As mentioned previously in the main text, there are two types of threshold logarithms. The first type is proportional to the logarithm $\alpha_s \ln \Lambda^2/\mu^2$ and the corresponding partonic splitting function as shown in the above-mentioned NLO corrections (see σ_{qq}^1 , σ_{gg}^1 , σ_{gq}^1 and σ_{qg}^1), and it is associated with the collinear branching of partons. The second type is proportional to either $\alpha_s \ln k_\perp^2/\Lambda^2$ or $\alpha_s \ln^2 k_\perp^2/\Lambda^2$, and this type originates from the soft emission of gluons near the kinematic threshold. We first address the issue of the resummation of the collinear part in this section, and then take care of the soft logarithms via the Sudakov factor in the next section.

A. Resummation of the collinear logarithms via the DGLAP evolution

Following the same idea proposed in Ref. [62], we can resum the collinear part of the threshold logarithms [88–90] with the help of the DGLAP evolution, by setting the factorization scale μ to be Λ . To deal with the first term of σ_{qq}^1 , the first term of σ_{gg}^1 , σ_{gq}^1 and σ_{qg}^1 , we apply the following replacement

$$\begin{bmatrix} q(x_p, \mu) \\ g(x_p, \mu) \end{bmatrix} + \frac{\alpha_s}{2\pi} \ln \frac{\Lambda^2}{\mu^2} \int_{x_p}^1 \frac{d\xi}{\xi} \begin{bmatrix} C_F \mathcal{P}_{qq}(\xi) & T_R \mathcal{P}_{qg}(\xi) \\ C_F \mathcal{P}_{gq}(\xi) & N_C \mathcal{P}_{gg}(\xi) \end{bmatrix} \begin{bmatrix} q(x_p/\xi, \mu) \\ g(x_p/\xi, \mu) \end{bmatrix} \Rightarrow \begin{bmatrix} q(x_p, \Lambda) \\ g(x_p, \Lambda) \end{bmatrix}. \quad (93)$$

Upon the above replacement, the threshold logarithm $\ln \frac{\Lambda^2}{\mu^2}$ combined with the corresponding splitting function effectively evolves the factorization scale of the PDFs in the LO cross-section from μ^2 back to Λ^2 .

The same procedure also can be applied to the FF part. To see this more clearly, we need to rewrite σ_{qq}^{LO} and the second term of σ_{qq}^1 as

$$\begin{aligned} \frac{d\sigma_{qq}^{\text{LO}}}{dy d^2 p_T} &= S_\perp \int_\tau^1 \frac{dz}{z^2} x_p q(x_p, \mu^2) D_{h/q}(z, \mu^2) F(k_\perp) \Big|_{x_p=\frac{\tau}{z}, k_\perp=\frac{p_T}{z}}, \\ \frac{d\sigma_{qq}^{1'}}{dy d^2 p_T} &= \frac{\alpha_s}{2\pi} C_F S_\perp \int d\xi \int \frac{dz'}{z'^2} \theta(z' - \tau) \theta(1 - z') \theta(\xi - \frac{\tau}{z'}) \theta(1 - \xi) \\ &\quad \times x q(x, \mu^2) D_{h/q}(z', \mu^2) \mathcal{P}_{qq}(\xi) \ln \frac{\Lambda^2}{\mu^2} \frac{1}{\xi^2} F\left(\frac{k_\perp}{\xi}\right) \Big|_{x=\frac{\tau}{z'\xi}, k_\perp=\frac{p_T}{z'}}, \\ &= \frac{\alpha_s}{2\pi} C_F S_\perp \int_\tau^1 \frac{dz}{z^2} x q(x, \mu^2) F\left(\frac{p_T}{z}\right) \ln \frac{\Lambda^2}{\mu^2} \int_z^1 \frac{d\xi}{\xi} D_{h/q}\left(\frac{z}{\xi}, \mu^2\right) \mathcal{P}_{qq}(\xi) \Big|_{x=\frac{\tau}{z}, z=z'\xi}. \end{aligned} \quad (94)$$

The first line of Eq. (95) is exactly the same as the second term of Eq. (38), albeit in a slightly different form. From the first line of Eq. (95) to the second line, we changed the variable z to $z'\xi$. It is then apparent that we can resum the second term of σ_{qq}^1 , the second term of σ_{gg}^1 , σ_{gq}^2 and σ_{qg}^2 through the DGLAP evolution of the FFs through the following replacement

$$\begin{bmatrix} D_{h/q}(z, \mu) \\ D_{h/g}(z, \mu) \end{bmatrix} + \frac{\alpha_s}{2\pi} \ln \frac{\Lambda^2}{\mu^2} \int_z^1 \frac{d\xi}{\xi} \begin{bmatrix} C_F \mathcal{P}_{qq}(\xi) & C_F \mathcal{P}_{gq}(\xi) \\ T_R \mathcal{P}_{qg}(\xi) & N_C \mathcal{P}_{gg}(\xi) \end{bmatrix} \begin{bmatrix} D_{h/q}(z/\xi, \mu) \\ D_{h/g}(z/\xi, \mu) \end{bmatrix} \Rightarrow \begin{bmatrix} D_{h/q}(z, \Lambda) \\ D_{h/g}(z, \Lambda) \end{bmatrix}. \quad (96)$$

To conclude, we have taken care of the resummation of the collinear threshold logarithms in the following NLO correction terms σ_{qq}^1 , σ_{gg}^1 , σ_{gq}^1 , σ_{qg}^1 , σ_{gg}^2 , σ_{gq}^2 and σ_{qg}^2 by setting the factorization scales in σ_{qq}^{LO} and σ_{gg}^{LO} to be Λ^2 . Since Λ^2 is usually smaller than μ^2 , we refer to this approach as the reverse-evolution method in this paper.

B. An alternative formulation of the threshold resummation

Alternatively, there is another analytical approach to resum the above mentioned collinear logarithms ($\alpha_s \ln \frac{\mu^2}{\Lambda^2}$) in the threshold limit. This approach is similar to the renormalization-group method first developed in Refs. [89, 90] for DIS within the SCET framework. Our strategy is laid out as follows. First, we transform the terms which contain large logarithms of $\ln \frac{\mu^2}{\Lambda^2}$ into the Mellin space. Second, we resum the corresponding large logarithms in the Mellin space in the large- N limit. In the end, we perform the inverse Mellin transform back to the momentum space.

As a matter of fact, the analytical results obtained in this subsection are consistent with those in the SCET approach. Furthermore, we have checked that this alternative approach numerically also agrees well with the resummation method mentioned in the above subsection.

1. Mellin Transform

Let us use the $q \rightarrow q$ channel as an example to demonstrate how to perform Mellin transform and carry out resummation in the Mellin space. The derivation for the $g \rightarrow g$ channel is similar. Due to the existence of the endpoint singularity in the splitting functions \mathcal{P}_{qq} and \mathcal{P}_{gg} when $\xi \rightarrow 1$, the Mellin transform integral is dominated by the endpoint for sufficiently large N . In contrast, the off-diagonal splitting functions contain no plus-functions or δ functions. Therefore, the threshold effects from the off-diagonal channels are much smaller than those in the diagonal channels.

The Mellin transform and the inverse Mellin transform are usually defined as

$$f(N) = \int_0^1 dx x^{N-1} f(x), \quad (97)$$

$$f(x) = \frac{1}{2\pi i} \int_{\mathcal{C}} dN x^{-N} f(N), \quad (98)$$

where \mathcal{C} stands for the proper contour which puts all the poles to its left.

Following the same strategy developed in the last subsection, we resum the collinear logarithms associated with PDFs and FFs separately. For the first term of σ_{qq}^1 , we carry out the Mellin transform as follows

$$\int_0^1 dx_p x_p^{N-1} \int_{x_p}^1 \frac{d\xi}{\xi} q\left(\frac{x_p}{\xi}\right) \mathcal{P}_{qq}(\xi) = \int_0^1 d\xi \xi^{N-1} \mathcal{P}_{qq}(\xi) \int_0^1 dx x^{N-1} q(x) = \mathcal{P}_{qq}(N) q(N), \quad (99)$$

where $q(N) \equiv \int_0^1 dx x^{N-1} q(x)$ and $\mathcal{P}_{qq}(N) \equiv \int_0^1 d\xi \xi^{N-1} \mathcal{P}_{qq}(\xi)$. Similarly, for the second term in σ_{qq}^1 , we obtain

$$\int_0^1 dz z^{N-1} \int_z^1 \frac{d\xi}{\xi} D_{h/q}\left(\frac{z}{\xi}\right) \mathcal{P}_{qq}(\xi) = \mathcal{P}_{qq}(N) D_{h/q}(N), \quad (100)$$

with $D_{h/q}(N) \equiv \int_0^1 dz z^{N-1} D_{h/q}(z)$. Furthermore, we can evaluate $\mathcal{P}_{qq}(N)$ and find

$$\mathcal{P}_{qq}(N) = -2\gamma_E - 2\psi(N) + \frac{3}{2} - \frac{1}{N} - \frac{1}{N+1} = -2\gamma_E - 2\ln N + \frac{3}{2} + \mathcal{O}\left(\frac{1}{N}\right), \quad (101)$$

where $\psi(N) = \ln N + \mathcal{O}\left(\frac{1}{N}\right)$ is the polygamma function. We have taken the large- N limit in the last step.

In the threshold limit, the resummation of the collinear logarithm in the σ_{qq}^1 term in the Mellin space results in an exponential [83–90]. It is worth mentioning that the corresponding contribution from the off-diagonal channels is suppressed in the large- N limit. The resummed quark PDFs and FFs in the Mellin space can be cast into

$$q^{\text{res}}(N) = q(N) \exp\left[-\frac{\alpha_s}{\pi} C_F \ln \frac{\Lambda^2}{\mu^2} \left(\gamma_E - \frac{3}{4} + \ln N\right)\right], \quad (102)$$

$$D_{h/q}^{\text{res}}(N) = D_{h/q}(N) \exp\left[-\frac{\alpha_s}{\pi} C_F \ln \frac{\Lambda^2}{\mu^2} \left(\gamma_E - \frac{3}{4} + \ln N\right)\right]. \quad (103)$$

Then we perform the inverse Mellin transform with respect to $q^{\text{res}}(N)$ and get

$$\begin{aligned} q^{\text{res}}(x_p, \Lambda^2, \mu^2) &= \int_{\mathcal{C}} \frac{dN}{2\pi i} x_p^{-N} q(N) \exp\left[-\frac{\alpha_s}{\pi} C_F \ln \frac{\Lambda^2}{\mu^2} \left(\gamma_E - \frac{3}{4} + \ln N\right)\right] \\ &= \exp\left[-\frac{\alpha_s}{\pi} C_F \ln \frac{\Lambda^2}{\mu^2} \left(\gamma_E - \frac{3}{4}\right)\right] \int_0^1 \frac{dx}{x} q(x, \mu^2) \int_{\mathcal{C}} \frac{dN}{2\pi i} \left(\frac{x}{x_p}\right)^N \exp\left[-\frac{\alpha_s}{\pi} C_F \ln \frac{\Lambda^2}{\mu^2} \ln N\right]. \end{aligned} \quad (104)$$

Using the following identity

$$\int_{\mathcal{C}} \frac{dN}{2\pi i} \left(\frac{x}{x_p}\right)^N e^{-\gamma_{\Lambda, \mu}^q \ln N} = \frac{\theta(x - x_p)}{\Gamma(\gamma_{\Lambda, \mu}^q)} \left(\ln \frac{x}{x_p}\right)^{\gamma_{\Lambda, \mu}^q - 1}, \quad \text{Re}\left[\gamma_{\Lambda, \mu}^q\right] > 0, \quad (105)$$

with $\gamma_{\Lambda, \mu}^q = \frac{\alpha_s}{\pi} C_F \ln \frac{\Lambda^2}{\mu^2}$, we reach the resummed expression for the quark distribution

$$q^{\text{res}}(x_p, \Lambda^2, \mu^2) = \frac{e^{-\gamma_{\Lambda, \mu}^q (\gamma_E - \frac{3}{4})}}{\Gamma(\gamma_{\Lambda, \mu}^q)} \int_{x_p}^1 \frac{dx}{x} q(x, \mu^2) \left(\ln \frac{x}{x_p}\right)^{\gamma_{\Lambda, \mu}^q - 1}, \quad \text{Re}\left[\gamma_{\Lambda, \mu}^q\right] > 0. \quad (106)$$

Similarly, for the collinear threshold logarithm associated with the quark FF, we have

$$D_{h/q}^{\text{res}}(z, \Lambda^2, \mu^2) = \frac{e^{-\gamma_{\Lambda, \mu}^q(\gamma_E - \frac{3}{4})}}{\Gamma(\gamma_{\Lambda, \mu}^q)} \int_z^1 \frac{dz'}{z'} D_{h/q}(z', \mu^2) \left(\ln \frac{z'}{z} \right)^{\gamma_{\Lambda, \mu}^q - 1}, \quad \text{Re} \left[\gamma_{\Lambda, \mu}^q \right] > 0, \quad (107)$$

In the running coupling case, the anomalous dimension $\gamma_{\Lambda, \mu}^q$ reads

$$\gamma_{\Lambda, \mu}^q = C_F \int_{\mu^2}^{\Lambda^2} \frac{d\mu'^2}{\mu'^2} \frac{\alpha_s(\mu'^2)}{\pi}. \quad (108)$$

For the $g \rightarrow g$ channel, the color factor and the splitting function are different from those in the $q \rightarrow q$ channel. The Mellin transform of $\mathcal{P}_{gg}(\xi)$ is given by

$$\mathcal{P}_{gg}(N) \equiv \int_0^1 d\xi \xi^{N-1} \mathcal{P}_{gg}(\xi) = -2 \left[\gamma_E + \psi(N) - \beta_0 - \frac{2}{N(N^2 - 1)} + \frac{1}{N + 2} \right] = -2 [\gamma_E - \beta_0 + \ln N] + \mathcal{O}\left(\frac{1}{N}\right), \quad (109)$$

where $\beta_0 = \frac{11}{12} - \frac{n_f}{6N_c}$ and we have taken large- N limit in the last step. Therefore, for the gluon case, we obtain the following expressions for the resummed gluon PDF and FF

$$g^{\text{res}}(x_p, \Lambda^2, \mu^2) = \frac{e^{-\gamma_{\Lambda, \mu}^g(\gamma_E - \beta_0)}}{\Gamma(\gamma_{\Lambda, \mu}^g)} \int_{x_p}^1 \frac{dx}{x} g(x, \mu^2) \left(\ln \frac{x}{x_p} \right)^{\gamma_{\Lambda, \mu}^g - 1}, \quad \text{Re} \left[\gamma_{\Lambda, \mu}^g \right] > 0, \quad (110)$$

$$D_{h/g}^{\text{res}}(z, \Lambda^2, \mu^2) = \frac{e^{-\gamma_{\Lambda, \mu}^g(\gamma_E - \beta_0)}}{\Gamma(\gamma_{\Lambda, \mu}^g)} \int_z^1 \frac{dz'}{z'} D_{h/g}(z', \mu^2) \left(\ln \frac{z'}{z} \right)^{\gamma_{\Lambda, \mu}^g - 1}, \quad \text{Re} \left[\gamma_{\Lambda, \mu}^g \right] > 0, \quad (111)$$

where the gluon channel anomalous dimension reads

$$\gamma_{\Lambda, \mu}^g = N_c \int_{\mu^2}^{\Lambda^2} \frac{d\mu'^2}{\mu'^2} \frac{\alpha_s(\mu'^2)}{\pi}. \quad (112)$$

2. The forward threshold jet function

Analogous to the jet function defined in Refs. [89, 90], we can also define the so-called forward threshold jet functions $\Delta^q(\Lambda^2, \mu^2, \omega)$ and $\Delta^g(\Lambda^2, \mu^2, \omega)$ in the quark and gluon channels, respectively. These two functions can be written as

$$\Delta^q(\Lambda^2, \mu^2, \omega) = \frac{e^{-\gamma_{\Lambda, \mu}^q(\gamma_E - \frac{3}{4})}}{\Gamma(\gamma_{\Lambda, \mu}^q)} \omega^{\gamma_{\Lambda, \mu}^q - 1}, \quad \text{Re} \left[\gamma_{\Lambda, \mu}^q \right] > 0, \quad (113)$$

$$\Delta^g(\Lambda^2, \mu^2, \omega) = \frac{e^{-\gamma_{\Lambda, \mu}^g(\gamma_E - \beta_0)}}{\Gamma(\gamma_{\Lambda, \mu}^g)} \omega^{\gamma_{\Lambda, \mu}^g - 1}, \quad \text{Re} \left[\gamma_{\Lambda, \mu}^g \right] > 0, \quad (114)$$

with $\omega \equiv \ln \frac{1}{\xi}$. Here the splitting fraction of the longitudinal momentum ξ is $\frac{x_p}{x}$ for the initial state gluon emission and it should be identified as $\frac{z}{z'}$ in the case of final state gluon emission. The resummed PDFs and FFs derived in the last section can then be written as

$$q^{\text{res}}(x_p, \Lambda^2, \mu^2) = \int_{x_p}^1 \frac{dx}{x} q(x, \mu^2) \Delta^q(\Lambda^2, \mu^2, \omega = \ln \frac{x}{x_p}), \quad (115)$$

$$g^{\text{res}}(x_p, \Lambda^2, \mu^2) = \int_{x_p}^1 \frac{dx}{x} g(x, \mu^2) \Delta^g(\Lambda^2, \mu^2, \omega = \ln \frac{x}{x_p}), \quad (116)$$

$$D_{h/q}^{\text{res}}(z, \Lambda^2, \mu^2) = \int_z^1 \frac{dz'}{z'} D_{h/q}(z', \mu^2) \Delta^q(\Lambda^2, \mu^2, \omega = \ln \frac{z}{z'}), \quad (117)$$

$$D_{h/g}^{\text{res}}(z, \Lambda^2, \mu^2) = \int_z^1 \frac{dz'}{z'} D_{h/g}(z', \mu^2) \Delta^g(\Lambda^2, \mu^2, \omega = \ln \frac{z}{z'}). \quad (118)$$

To connect and compare with the renormalization group approach in Refs. [89, 90], we differentiate Eqs. (113-114) with respect to $\ln \mu^2$ and find

$$\frac{d\Delta^q(\Lambda^2, \mu^2, \omega)}{d \ln \mu^2} = -\frac{\alpha_s C_F}{\pi} \left[-\gamma_E + \frac{3}{4} - \psi(\gamma_{\Lambda, \mu}^q) + \ln \omega \right] \Delta^q(\Lambda^2, \mu^2, \omega), \quad (119)$$

$$\frac{d\Delta^g(\Lambda^2, \mu^2, \omega)}{d \ln \mu^2} = -\frac{\alpha_s N_c}{\pi} \left[-\gamma_E + \beta_0 - \psi(\gamma_{\Lambda, \mu}^g) + \ln \omega \right] \Delta^g(\Lambda^2, \mu^2, \omega). \quad (120)$$

Due to the scale dependence in the anomalous dimensions, the flow directions of the renormalization group equation for the μ and Λ scales are opposite to each other. Employing the identity of the digamma function $\psi(\gamma) = -\gamma_E + \int_0^1 du \frac{1-u\gamma^{-1}}{1-u}$, we can show that the collinear jet threshold functions Δ^q and Δ^g defined above satisfy the following integro-differential equations

$$\frac{d\Delta^q(\Lambda^2, \mu^2, \omega)}{d \ln \mu^2} = -\frac{\alpha_s C_F}{\pi} \left[\ln \omega + \frac{3}{4} \right] \Delta^q(\Lambda^2, \mu^2, \omega) + \frac{\alpha_s C_F}{\pi} \int_0^\omega d\omega' \frac{\Delta^q(\Lambda^2, \mu^2, \omega) - \Delta^q(\Lambda^2, \mu^2, \omega')}{\omega - \omega'}, \quad (121)$$

$$\frac{d\Delta^g(\Lambda^2, \mu^2, \omega)}{d \ln \mu^2} = -\frac{\alpha_s N_c}{\pi} [\ln \omega + \beta_0] \Delta^g(\Lambda^2, \mu^2, \omega) + \frac{\alpha_s N_c}{\pi} \int_0^\omega d\omega' \frac{\Delta^g(\Lambda^2, \mu^2, \omega) - \Delta^g(\Lambda^2, \mu^2, \omega')}{\omega - \omega'}, \quad (122)$$

respectively. In deriving the above result, we have used $\Delta^{q/g}(\Lambda^2, \mu^2, \omega) \propto \omega^{\gamma_{\Lambda, \mu}^{q/g}-1}$ together with the identity

$$\int_0^1 du u^{\gamma_{\Lambda, \mu}^{q/g}-1} \Delta^{q/g}(\Lambda^2, \mu^2, \omega) = \int_0^\omega \frac{d\omega'}{\omega} \Delta^{q/g}(\Lambda^2, \mu^2, \omega'). \quad (123)$$

In the threshold limit which gives rise to the approximation $\ln \frac{1}{\xi} |_{\xi \rightarrow 1} \approx 1 - \xi$, the above evolution equation for the jet function $\Delta^q(\Lambda^2, \mu^2, \omega)$ looks rather similar to that developed in Refs. [89, 90] within the SCET framework. The only difference lies in the absence of the Sudakov double logarithm ($-\frac{\alpha_s C_F}{2\pi} L^2$) and the single logarithm ($\frac{3}{2} \frac{\alpha_s C_F}{\pi} L$) with $L = \ln k_\perp^2 / \Lambda^2$. To simplify the theoretical derivations presented in this paper, we choose to first resum the collinear logarithms using the renormalization group equations given by Eqs. (121-122). Then, we deal with the resummation of the single and double soft logarithms separately through the Sudakov factor in Sec. IV. The bottom line is that the threshold implemented in our calculation is consistent with the systematic renormalization group equation approach discussed in Refs. [89, 90].

3. Analytic Continuation

The resummed results obtained above are well-defined in the $\text{Re}[\gamma_{\Lambda, \mu}^{q/g}] > 0$ region. However, they become singular at $\xi = 1$ (or equivalently speaking, $x = x_p$ or $z = z'$) when $\text{Re}[\gamma_{\Lambda, \mu}^{q/g}] \leq 0$. This is simply due to the fact that Eq. (105) requires $\text{Re}[\gamma_{\Lambda, \mu}^{q/g}] > 0$ in order to close the integral contour to the left. Similar to the analytic continuation of the gamma function¹, the identity shown in Eq. (105) can be extended to the entire complex plane. For example, we can analytically continue the resummed results to the region where $-1 < \text{Re}[\gamma_{\Lambda, \mu}^{q/g}] \leq 0$ in the complex plane by reconsidering the following inverse Mellin transform

$$\begin{aligned} & \int_0^1 \frac{dx}{x} q(x, \mu^2) \int_C \frac{dN}{2\pi i} \left(\frac{x}{x_p} \right)^N e^{-\gamma_{\Lambda, \mu}^q \ln N} \\ &= \int_0^1 \frac{dx}{x} [q(x, \mu^2) - q(x_p, \mu^2)] \int_C \frac{dN}{2\pi i} \left(\frac{x}{x_p} \right)^N e^{-\gamma_{\Lambda, \mu}^q \ln N} + \int_0^1 \frac{dx}{x} q(x_p, \mu^2) \int_C \frac{dN}{2\pi i} \left(\frac{x}{x_p} \right)^N e^{-\gamma_{\Lambda, \mu}^q \ln N} \\ &= \int_{x_p}^1 \frac{dx}{x} [q(x, \mu^2) - q(x_p, \mu^2)] \frac{1}{\Gamma(\gamma_{\Lambda, \mu}^q)} \left(\ln \frac{x}{x_p} \right)^{\gamma_{\Lambda, \mu}^q - 1} + q(x_p, \mu^2) \frac{1}{\Gamma(\gamma_{\Lambda, \mu}^q + 1)} \left(\ln \frac{1}{x_p} \right)^{\gamma_{\Lambda, \mu}^q}. \end{aligned} \quad (124)$$

¹ To understand this point better, we briefly recall the analytic continuation of the gamma function $\Gamma(z)$. Conventionally, $\Gamma(z)$ is defined via the integral, $\Gamma(z) = \int_0^\infty dx x^{z-1} e^{-x}$, when $\text{Re}[z] > 0$. This integral is divergent at $\text{Re}[z] \leq 0$ and therefore $\Gamma(z)$ is not properly defined with this expression in this region. The relation

$\Gamma(z) = \frac{1}{z} \Gamma(z+1)$ can be employed to uniquely extend the gamma function to the $-1 < \text{Re}[z] \leq 0$ region. Furthermore, using the above relation repeatedly, we can further extend $\Gamma(z)$ to the entire negative half plane except zero and negative integers.

It is then clear that the applicable range of the resummed results is extended and now it includes the $-1 < \text{Re}[\gamma_{\Lambda,\mu}^{q/g}] \leq 0$ region. To extend to the smaller $\text{Re}[\gamma_{\Lambda,\mu}^q]$ region, we can repeat the same strategy and consider the following subtractions

$$\begin{aligned}
& \int_0^1 \frac{dx}{x} q(x, \mu^2) \int_{\mathcal{C}} \frac{dN}{2\pi i} \left(\frac{x}{x_p} \right)^N e^{-\gamma_{\Lambda,\mu}^q \ln N} \\
&= \int_0^1 \frac{dx}{x} \left[q(x, \mu^2) - q(x_p, \mu^2) - x_p q'(x_p) \ln \frac{x}{x_p} \right] \int_{\mathcal{C}} \frac{dN}{2\pi i} \left(\frac{x}{x_p} \right)^N e^{-\gamma_{\Lambda,\mu}^q \ln N} \\
&\quad + \int_0^1 \frac{dx}{x} \left[q(x_p, \mu^2) + x_p q'(x_p) \ln \frac{x}{x_p} \right] \int_{\mathcal{C}} \frac{dN}{2\pi i} \left(\frac{x}{x_p} \right)^N e^{-\gamma_{\Lambda,\mu}^q \ln N} \\
&= \int_{x_p}^1 \frac{dx}{x} \left[q(x, \mu^2) - q(x_p, \mu^2) - x_p q'(x_p, \mu^2) \ln \frac{x}{x_p} \right] \frac{1}{\Gamma(\gamma_{\Lambda,\mu}^q)} \left(\ln \frac{x}{x_p} \right)^{\gamma_{\Lambda,\mu}^q - 1} \\
&\quad + q(x_p, \mu^2) \frac{1}{\Gamma(\gamma_{\Lambda,\mu}^q + 1)} \left(\ln \frac{1}{x_p} \right)^{\gamma_{\Lambda,\mu}^q} + x_p q'(x_p, \mu^2) \frac{\gamma_{\Lambda,\mu}^q}{\Gamma(\gamma_{\Lambda,\mu}^q + 2)} \left(\ln \frac{1}{x_p} \right)^{\gamma_{\Lambda,\mu}^q + 1}, \tag{125}
\end{aligned}$$

where $q'(x_p, \mu^2) \equiv \frac{dq(x, \mu^2)}{dx}|_{x=x_p}$. The above subtraction method extends the validation range of our results to $\text{Re}[\gamma_{\Lambda,\mu}^q] > -2$. In principle, we can repeat the same trick and cover the entire complex plane. In practice, it is quite challenging to numerically evaluate higher order derivatives of PDFs or FFs for the regime with $\text{Re}[\gamma_{\Lambda,\mu}^q] < -2$. Conventionally, one can introduce the star distribution [87, 89, 90] and rewrite the resummed PDFs and FFs as

$$q^{\text{res}}(x_p, \Lambda^2, \mu^2) = \frac{e^{-\gamma_{\Lambda,\mu}^q (\gamma_E - \frac{3}{4})}}{\Gamma(\gamma_{\Lambda,\mu}^q)} \int_{x_p}^1 \frac{dx}{x} q(x, \mu^2) \left(\ln \frac{x}{x_p} \right)_*^{\gamma_{\Lambda,\mu}^q - 1}, \tag{126}$$

$$g^{\text{res}}(x_p, \Lambda^2, \mu^2) = \frac{e^{-\gamma_{\Lambda,\mu}^g (\gamma_E - \beta_0)}}{\Gamma(\gamma_{\Lambda,\mu}^g)} \int_{x_p}^1 \frac{dx}{x} g(x, \mu^2) \left(\ln \frac{x}{x_p} \right)_*^{\gamma_{\Lambda,\mu}^g - 1}, \tag{127}$$

$$D_{h/q}^{\text{res}}(z, \Lambda^2, \mu^2) = \frac{e^{-\gamma_{\Lambda,\mu}^q (\gamma_E - \frac{3}{4})}}{\Gamma(\gamma_{\Lambda,\mu}^q)} \int_z^1 \frac{dz'}{z'} D_{h/q}(z', \mu^2) \left(\ln \frac{z'}{z} \right)_*^{\gamma_{\Lambda,\mu}^q - 1}, \tag{128}$$

$$D_{h/g}^{\text{res}}(z, \Lambda^2, \mu^2) = \frac{e^{-\gamma_{\Lambda,\mu}^g (\gamma_E - \beta_0)}}{\Gamma(\gamma_{\Lambda,\mu}^g)} \int_z^1 \frac{dz'}{z'} D_{h/g}(z', \mu^2) \left(\ln \frac{z'}{z} \right)_*^{\gamma_{\Lambda,\mu}^g - 1}, \tag{129}$$

where the star distribution represents the analytical expression obtained from the analytic continuation and it is properly defined in the full $\gamma_{\Lambda,\mu}^{q/g}$ complex plane.

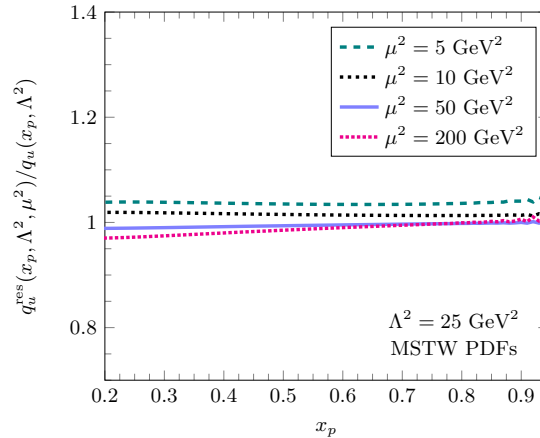


FIG. 7. The ratios of $q_u^{\text{res}}(x_p, \Lambda^2, \mu^2)$ to $q_u(x_p, \Lambda^2)$ as a function of x_p with various values of μ^2 .

With the above analytic continuation technique, we can finally compute the resummed PDFs and FFs numerically for a broad range of μ^2 . To compare this renormalization group equation approach with the reverse-evolution approach

developed in the last subsection, we show the ratio of the up quark distributions in Fig. 7. Here the up quark distributions $q_u^{\text{res}}(x_p, \Lambda^2, \mu^2)$ and $q_u(x_p, \Lambda^2)$ are computed from the renormalization group approach and the reverse DGLAP approach, respectively. As shown in Fig. 7, the ratio is close to 1 in the intermediate and large x_p regions and it indicates that the numerical difference between these two approaches is small.

The reverse-evolution approach developed in Sec. III A does not rely on the large- N and $\xi \rightarrow 1$ approximations, which are vital in the renormalization group equation approach discussed in this subsection. Furthermore, it automatically takes care of the off-diagonal channels. Therefore, we employ the first approach in our numerical evaluations. Nonetheless, the fact that the ratio of $q_u^{\text{res}}(x_p, \Lambda^2, \mu^2)$ and $q_u(x_p, \Lambda^2)$ is rather close to 1 for various values of μ^2 suggests these two approaches are numerically equivalent.

IV. THE RESUMMATION OF THE SOFT LOGARITHMS

Let us discuss the resummation of the soft part of the threshold logarithms via the Sudakov factor in this section. Soft logarithms only appear in the $q \rightarrow q$ and $g \rightarrow g$ channels. Conventionally, these double and single logarithms can be resummed through the Sudakov factors. For the $q \rightarrow q$ channel, we have the following logarithms from the σ_{qq}^{5a} and σ_{qq}^2 terms,

$$-\frac{\alpha_s}{2\pi} C_F \ln^2 \frac{k_\perp^2}{\Lambda^2} + 3 \frac{\alpha_s}{2\pi} C_F \ln \frac{k_\perp^2}{\Lambda^2}. \quad (130)$$

The first term is the double logarithm term and the second one is the single logarithm term derived with the fixed strong coupling. As the common practice, we need to convert the above expression from the fixed coupling one to the running coupling one in phenomenology. Therefore, in the threshold resummation, we employ the following Sudakov factor

$$S_{\text{Sud}}^{qq} = C_F \int_{\Lambda^2}^{k_\perp^2} \frac{d\mu^2}{\mu^2} \frac{\alpha_s(\mu^2)}{\pi} \ln \frac{k_\perp^2}{\mu^2} - 3C_F \int_{\Lambda^2}^{k_\perp^2} \frac{d\mu^2}{\mu^2} \frac{\alpha_s(\mu^2)}{2\pi}. \quad (131)$$

The resummation of soft logarithms becomes an exponential of the Sudakov factor. The extraction of the double logarithms is quite challenging in the running coupling case. Alternatively, we first extract those soft logarithms with the fixed coupling and then compute the mismatch term to take into account the difference. The difference between the running coupling Sudakov factor and the fixed coupling NLO correction is cast into the following matching term,

$$S_{\text{Sud}}^{qq} - C_F \frac{\alpha_s}{2\pi} \left(\ln^2 \frac{k_\perp^2}{\Lambda^2} - 3 \ln \frac{k_\perp^2}{\Lambda^2} \right). \quad (132)$$

The discussion for the $g \rightarrow g$ channel also follows suit. At the end of the day, the resummed formula reads

$$\begin{aligned} \frac{d\sigma_{\text{resummed}}}{dyd^2p_T} = & S_\perp \int_\tau^1 \frac{dz}{z^2} x_p q(x_p, \Lambda^2) D_{h/q}(z, \Lambda^2) F(k_\perp) e^{-S_{\text{Sud}}^{qq}} \\ & + S_\perp \int_\tau^1 \frac{dz}{z^2} x_p g(x_p, \Lambda^2) D_{h/g}(z, \Lambda^2) \int d^2q_{1\perp} F(q_{1\perp}) F(k_\perp - q_{1\perp}) e^{-S_{\text{Sud}}^{gg}}, \end{aligned} \quad (133)$$

where S_{Sud}^{qq} and S_{Sud}^{gg} are Sudakov factors for $q \rightarrow q$ and $g \rightarrow g$ channels which are given by

$$S_{\text{Sud}}^{qq} = C_F \int_{\Lambda^2}^{k_\perp^2} \frac{d\mu^2}{\mu^2} \frac{\alpha_s(\mu^2)}{\pi} \ln \frac{k_\perp^2}{\mu^2} - 3C_F \int_{\Lambda^2}^{k_\perp^2} \frac{d\mu^2}{\mu^2} \frac{\alpha_s(\mu^2)}{2\pi}, \quad (134)$$

$$S_{\text{Sud}}^{gg} = N_c \int_{\Lambda^2}^{k_\perp^2} \frac{d\mu^2}{\mu^2} \frac{\alpha_s(\mu^2)}{\pi} \ln \frac{k_\perp^2}{\mu^2} - \frac{11N_c - 2n_f}{3} \int_{\Lambda^2}^{k_\perp^2} \frac{d\mu^2}{\mu^2} \frac{\alpha_s(\mu^2)}{2\pi}. \quad (135)$$

The Sudakov factor follows the counting rule which is given in Refs. [81, 82]. As discussed in the last section, the factorization scale in Eq. (133) is set to be Λ as a result of the resummation of collinear logarithms.

Thus, the Sudakov matching term, which is treated as part of the NLO correction, is given by

$$\begin{aligned} \frac{d\sigma_{\text{Sud matching}}}{dyd^2p_T} = & S_\perp \int_\tau^1 \frac{dz}{z^2} x_p q(x_p, \mu^2) D_{h/q}(z, \mu^2) F(k_\perp) \left\{ S_{\text{Sud}}^{qq} - \left[C_F \frac{\alpha_s}{2\pi} \left(\ln^2 \frac{k_\perp^2}{\Lambda^2} - 3 \ln \frac{k_\perp^2}{\Lambda^2} \right) \right] \right\} \\ & + S_\perp \int_\tau^1 \frac{dz}{z^2} x_p g(x_p, \mu^2) D_{h/g}(z, \mu^2) \int d^2q_{1\perp} F(q_{1\perp}) F(k_\perp - q_{1\perp}) \\ & \times \left\{ S_{\text{Sud}}^{gg} - \left[N_c \frac{\alpha_s}{2\pi} \left(\ln^2 \frac{k_\perp^2}{\Lambda^2} - 4\beta_0 \ln \frac{k_\perp^2}{\Lambda^2} \right) \right] \right\}. \end{aligned} \quad (136)$$

V. SUMMARY OF THE FULL THRESHOLD RESUMMED RESULTS

To make the resummed results more accessible to the interested readers, we provide a thorough summary of the full NLO cross-section after the threshold resummation in the large N_c limit, which have been numerically evaluated and referred to as the ‘‘Resummed’’ results in the plots throughout the paper.

First, the resummation of the collinear logarithms in σ_{qq}^1 , σ_{gg}^1 , σ_{gq}^1 , σ_{qq}^2 , σ_{gg}^2 and σ_{gq}^2 terms sets the factorization scales in σ_{qq}^{LO} and σ_{gg}^{LO} to be Λ^2 . Second, the resummation of the soft logarithms in σ_{qq}^{5a} , σ_{qq}^2 , σ_{gg}^{6a} and σ_{gg}^2 terms yields the exponential expression of the Sudakov factor. The rest of the NLO corrections together with the matching terms do not contain apparent large logarithms and they are numerically small. Therefore, we treat them as the new NLO hard factors after the subtraction of logarithms. The resummation improved NLO cross-section is then given by

$$\frac{d\sigma}{dyd^2p_T} = \frac{d\sigma_{\text{resummed}}}{dyd^2p_T} + \frac{d\sigma_{\text{NLO matching}}}{dyd^2p_T} + \frac{d\sigma_{\text{Sud matching}}}{dyd^2p_T}, \quad (137)$$

where

$$\begin{aligned} \frac{d\sigma_{\text{resummed}}}{dyd^2p_T} &= S_{\perp} \int_{\tau}^1 \frac{dz}{z^2} x_p q(x_p, \Lambda^2) D_{h/q}(z, \Lambda^2) F(k_{\perp}) e^{-S_{\text{Sud}}^{qq}} \\ &\quad + S_{\perp} \int_{\tau}^1 \frac{dz}{z^2} x_p g(x_p, \Lambda^2) D_{h/g}(z, \Lambda^2) \int d^2q_{1\perp} F(q_{1\perp}) F(k_{\perp} - q_{1\perp}) e^{-S_{\text{Sud}}^{gg}}, \end{aligned} \quad (138)$$

$$\begin{aligned} \frac{d\sigma_{\text{Sud matching}}}{dyd^2p_T} &= S_{\perp} \int_{\tau}^1 \frac{dz}{z^2} x_p q(x_p, \mu^2) D_{h/q}(z, \mu^2) F(k_{\perp}) \left\{ S_{\text{Sud}}^{qq} - \left[C_F \frac{\alpha_s}{2\pi} \left(\ln^2 \frac{k_{\perp}^2}{\Lambda^2} - 3 \ln \frac{k_{\perp}^2}{\Lambda^2} \right) \right] \right\} \\ &\quad + S_{\perp} \int_{\tau}^1 \frac{dz}{z^2} x_p g(x_p, \mu^2) D_{h/g}(z, \mu^2) \int d^2q_{1\perp} F(q_{1\perp}) F(k_{\perp} - q_{1\perp}) \\ &\quad \times \left\{ S_{\text{Sud}}^{gg} - \left[N_c \frac{\alpha_s}{2\pi} \left(\ln^2 \frac{k_{\perp}^2}{\Lambda^2} - 4\beta_0 \ln \frac{k_{\perp}^2}{\Lambda^2} \right) \right] \right\}, \end{aligned} \quad (139)$$

$$\frac{d\sigma_{\text{NLO matching}}}{dyd^2p_T} = \sum_{i=3}^4 \frac{d\sigma_{qq}^i}{dyd^2p_T} + \frac{d\sigma_{qq}^{5b}}{dyd^2p_T} + \sum_{i=3}^5 \frac{d\sigma_{gg}^i}{dyd^2p_T} + \frac{d\sigma_{gg}^{6b}}{dyd^2p_T} + \frac{d\sigma_{gq}^3}{dyd^2p_T} + \frac{d\sigma_{gq}^2}{dyd^2p_T} + \sum_{i=4}^5 \frac{d\sigma_{gq}^i}{dyd^2p_T}. \quad (140)$$

The Sudakov factors are

$$S_{\text{Sud}}^{qq} = C_F \int_{\Lambda^2}^{k_{\perp}^2} \frac{d\mu^2}{\mu^2} \frac{\alpha_s(\mu^2)}{\pi} \ln \frac{k_{\perp}^2}{\mu^2} - 3C_F \int_{\Lambda^2}^{k_{\perp}^2} \frac{d\mu^2}{\mu^2} \frac{\alpha_s(\mu^2)}{2\pi}, \quad (141)$$

$$S_{\text{Sud}}^{gg} = N_c \int_{\Lambda^2}^{k_{\perp}^2} \frac{d\mu^2}{\mu^2} \frac{\alpha_s(\mu^2)}{\pi} \ln \frac{k_{\perp}^2}{\mu^2} - \frac{11N_c - 2n_f}{3} \int_{\Lambda^2}^{k_{\perp}^2} \frac{d\mu^2}{\mu^2} \frac{\alpha_s(\mu^2)}{2\pi}. \quad (142)$$

For the reader’s convenience, we list all the updated NLO matching terms in the following

$$\frac{d\sigma_{qq}^3}{dyd^2p_T} = \frac{\alpha_s}{2\pi^2} C_F S_{\perp} \int_{\tau}^1 \frac{dz}{z^2} \int_{\tau/z}^1 d\xi \int d^2q_{1\perp} d^2q_{2\perp} x q(x, \mu^2) D_{h/q}(z, \mu^2) \frac{1 + \xi^2}{(1 - \xi)_+} \mathcal{T}_{qq}^{(1)}(\xi, q_{1\perp}, q_{2\perp}, k_{\perp}), \quad (143)$$

$$\frac{d\sigma_{qq}^4}{dyd^2p_T} = -\frac{\alpha_s}{\pi} C_F S_{\perp} \int_{\tau}^1 \frac{dz}{z^2} \int_0^1 d\xi' \int d^2q_{1\perp} x_p q(x_p, \mu^2) D_{h/q}(z, \mu^2) \frac{1 + \xi'^2}{(1 - \xi')_+} \ln \frac{(q_{1\perp} - \xi' k_{\perp})^2}{k_{\perp}^2} F(q_{1\perp}) F(k_{\perp}), \quad (144)$$

$$\begin{aligned} \frac{d\sigma_{qq}^{5b}}{dyd^2p_T} &= \frac{2\alpha_s}{\pi^2} C_F S_{\perp} \int_{\tau}^1 \frac{dz}{z^2} \int d^2q_{1\perp} x_p q(x_p, \mu^2) D_{h/q}(z, \mu^2) \frac{1}{q_{1\perp}^2} \ln \frac{k_{\perp}^2}{q_{1\perp}^2} [F(k_{\perp} - q_{1\perp}) - \theta(\Lambda^2 - q_{1\perp}^2) F(k_{\perp})] \\ &\quad - \frac{\alpha_s}{2\pi} C_F S_{\perp} \int_{\tau}^1 \frac{dz}{z^2} x_p q(x_p, \mu^2) D_{h/q}(z, \mu^2) F(k_{\perp}) \ln^2 \frac{k_{\perp}^2}{\Lambda^2} \\ &\quad + \frac{\alpha_s}{\pi} C_F S_{\perp} \int_{\tau}^1 \frac{dz}{z^2} \int d^2q_{1\perp} x_p q(x_p, \mu^2) D_{h/q}(z, \mu^2) F(q_{1\perp}) F(k_{\perp}) \ln^2 \frac{k_{\perp}^2}{(k_{\perp} - q_{1\perp})^2} \\ &\quad - \frac{2\alpha_s}{\pi^2} C_F S_{\perp} \int_{\tau}^1 \frac{dz}{z^2} \int d^2q_{1\perp} \int d^2q_{2\perp} x_p q(x_p, \mu^2) D_{h/q}(z, \mu^2) F(q_{1\perp}) F(q_{2\perp}) \ln \frac{k_{\perp}^2}{(k_{\perp} - q_{1\perp})^2} \\ &\quad \times \frac{(k_{\perp} - q_{1\perp}) \cdot (k_{\perp} - q_{2\perp})}{(k_{\perp} - q_{1\perp})^2 (k_{\perp} - q_{2\perp})^2}, \end{aligned} \quad (145)$$

$$\begin{aligned} \frac{d\sigma_{gg}^3}{dyd^2p_T} &= \frac{\alpha_s}{\pi^2} N_c S_\perp \int_\tau^1 \frac{dz}{z^2} \int_{\tau/z}^1 d\xi \int d^2q_{1\perp} d^2q_{2\perp} d^2q_{3\perp} xg(x, \mu^2) D_{h/g}(z, \mu^2) \frac{[1 - \xi(1 - \xi)]^2}{\xi(1 - \xi)_+} \\ &\quad \times \mathcal{T}_{gg}^{(1)}(\xi, q_{1\perp}, q_{2\perp}, q_{3\perp}, k_\perp), \end{aligned} \quad (146)$$

$$\begin{aligned} \frac{d\sigma_{gg}^4}{dyd^2p_T} &= -2N_f T_R \frac{\alpha_s}{2\pi} S_\perp \int_\tau^1 \frac{dz}{z^2} \int_0^1 d\xi' d^2q_{1\perp} x_p g(x_p, \mu^2) D_{h/g}(z, \mu^2) [\xi'^2 + (1 - \xi')^2] \\ &\quad \times F(q_{1\perp}) F(k_\perp - q_{1\perp}) \ln \frac{(q_{1\perp} - \xi' k_\perp)^2}{k_\perp^2}, \end{aligned} \quad (147)$$

$$\begin{aligned} \frac{d\sigma_{gg}^5}{dyd^2p_T} &= -4N_c \frac{\alpha_s}{2\pi} S_\perp \int_\tau^1 \frac{dz}{z^2} \int_0^1 d\xi' d^2q_{1\perp} d^2q_{2\perp} x_p g(x_p, \mu^2) D_{h/g}(z, \mu^2) \left[\frac{\xi'}{(1 - \xi')_+} + \frac{1}{2} \xi'(1 - \xi') \right] \\ &\quad F(q_{1\perp}) F(q_{2\perp}) F(k_\perp - q_{1\perp}) \ln \frac{(q_{1\perp} + q_{2\perp} - \xi' k_\perp)^2}{k_\perp^2}, \end{aligned} \quad (148)$$

$$\begin{aligned} \frac{d\sigma_{gg}^{6b}}{dyd^2p_T} &= \frac{2\alpha_s}{\pi^2} N_c S_\perp \int_\tau^1 \frac{dz}{z^2} \int d^2q_{1\perp} \int d^2q_{2\perp} x_p g(x_p, \mu^2) D_{h/q}(z, \mu^2) \frac{1}{q_{2\perp}^2} \ln \frac{k_\perp^2}{q_{2\perp}^2} F(k_\perp - q_{1\perp}) \\ &\quad \times [F(q_{1\perp} + q_{2\perp}) - \theta(\Lambda^2 - q_{2\perp}^2) F(q_{1\perp})] \\ &\quad - \frac{\alpha_s}{2\pi} N_c S_\perp \int_\tau^1 \frac{dz}{z^2} x_p g(x_p, \mu^2) D_{h/q}(z, \mu^2) \ln^2 \frac{k_\perp^2}{\Lambda^2} \int d^2q_{1\perp} F(k_\perp - q_{1\perp}) F(q_{1\perp}) \\ &\quad + \frac{\alpha_s}{\pi} N_c S_\perp \int_\tau^1 \frac{dz}{z^2} \int d^2q_{1\perp} \int d^2q_{2\perp} x_p g(x_p, \mu^2) D_{h/q}(z, \mu^2) F(q_{1\perp}) F(q_{2\perp}) F(k_\perp - q_{2\perp}) \\ &\quad \times \ln^2 \frac{k_\perp^2}{(q_{1\perp} + q_{2\perp} - k_\perp)^2} \\ &\quad - \frac{2\alpha_s}{\pi^2} N_c S_\perp \int_\tau^1 \frac{dz}{z^2} \int d^2q_{1\perp} \int d^2q_{2\perp} \int d^2q_{3\perp} x_p g(x_p, \mu^2) D_{h/q}(z, \mu^2) F(q_{1\perp}) F(q_{2\perp}) F(q_{3\perp}) \\ &\quad \times \frac{(k_\perp - q_{1\perp} + q_{3\perp}) \cdot (k_\perp - q_{2\perp} + q_{3\perp})}{(k_\perp - q_{1\perp} + q_{3\perp})^2 (k_\perp - q_{2\perp} + q_{3\perp})^2} \ln \frac{k_\perp^2}{(k_\perp - q_{1\perp} + q_{3\perp})^2}, \end{aligned} \quad (149)$$

$$\frac{d\sigma_{gg}^3}{dyd^2p_T} = \frac{\alpha_s}{2\pi^2} C_F S_\perp \int_\tau^1 \frac{dz}{z^2} \int_{\tau/z}^1 d\xi \int d^2q_{1\perp} \int d^2q_{2\perp} xq(x, \mu^2) D_{h/g}(z, \mu^2) \mathcal{P}_{gq}(\xi) \mathcal{T}_{gq}^{(1)}(\xi, q_{1\perp}, q_{2\perp}, k_\perp), \quad (150)$$

$$\frac{d\sigma_{gg}^2}{dyd^2p_T} = -\frac{\alpha_s}{4\pi} S_\perp \int_\tau^1 \frac{dz}{z^2} \int_{\tau/z}^1 d\xi \int d^2q_{1\perp} xg(x, \mu^2) D_{h/q}(z, \mu^2) \frac{1}{\xi^2} \mathcal{P}_{qg}(\xi) F(q_{1\perp}) F(k_\perp/\xi - q_{1\perp}), \quad (151)$$

$$\frac{d\sigma_{gg}^4}{dyd^2p_T} = -\frac{\alpha_s}{4\pi} S_\perp \int_\tau^1 \frac{dz}{z^2} \int_{\tau/z}^1 d\xi xg(x, \mu^2) D_{h/q}(z, \mu^2) \mathcal{P}_{qg}(\xi) F(k_\perp), \quad (152)$$

$$\frac{d\sigma_{gg}^5}{dyd^2p_T} = \frac{\alpha_s}{4\pi^2} S_\perp \int_\tau^1 \frac{dz}{z^2} \int_{\tau/z}^1 d\xi \int d^2q_{1\perp} \int d^2q_{2\perp} xg(x, \mu^2) D_{h/q}(z, \mu^2) \mathcal{P}_{qg}(\xi) \mathcal{T}_{qg}^{(1)}(\xi, q_{1\perp}, q_{2\perp}, k_\perp), \quad (153)$$

where we have defined

$$\begin{aligned} \mathcal{T}_{qg}^{(1)}(\xi, q_{1\perp}, q_{2\perp}, k_\perp) &= \frac{(q_{2\perp} - q_{1\perp}/\xi)^2}{(k_\perp + q_{1\perp})^2 (k_\perp/\xi + q_{2\perp})^2} F(q_{1\perp}) F(q_{2\perp}) \\ &\quad - \frac{1}{(k_\perp + q_{1\perp})^2} \frac{\Lambda^2}{\Lambda^2 + (k_\perp + q_{1\perp})^2} F(q_{2\perp}) F(k_\perp) \\ &\quad - \frac{1}{(k_\perp + \xi q_{2\perp})^2} \frac{\Lambda^2}{\Lambda^2 + (k_\perp/\xi + q_{2\perp})^2} F(k_\perp/\xi) F(q_{1\perp}), \end{aligned} \quad (154)$$

$$\begin{aligned} \mathcal{T}_{gg}^{(1)}(\xi, q_{1\perp}, q_{2\perp}, q_{3\perp}, k_\perp) &= \frac{1}{\xi^2} \frac{[(1 - \xi)q_{1\perp} + q_{3\perp} - \xi q_{2\perp}]^2}{(q_{1\perp} + q_{3\perp} - k_\perp)^2 (q_{1\perp} + q_{2\perp} - k_\perp/\xi)^2} F(q_{1\perp}) F(q_{2\perp}) F(q_{3\perp}) \\ &\quad - \frac{1}{(q_{1\perp} + q_{3\perp} - k_\perp)^2} \frac{\Lambda^2}{\Lambda^2 + (q_{1\perp} + q_{3\perp} - k_\perp)^2} F(k_\perp - q_{3\perp}) F(q_{2\perp}) F(q_{3\perp}) \\ &\quad - \frac{1}{\xi^2} \frac{1}{(q_{1\perp} + q_{2\perp} - k_\perp/\xi)^2} \frac{\Lambda^2}{\Lambda^2 + (q_{1\perp} + q_{2\perp} - k_\perp/\xi)^2} F(k_\perp/\xi - q_{2\perp}) F(q_{2\perp}) F(q_{3\perp}), \end{aligned} \quad (155)$$

$$\begin{aligned}
\mathcal{T}_{gq}^{(1)}(\xi, q_{1\perp}, q_{2\perp}, k_{\perp}) &= \left(\frac{k_{\perp} - q_{1\perp} - q_{2\perp}}{(k_{\perp} - q_{1\perp} - q_{2\perp})^2} - \frac{k_{\perp} - \xi q_{2\perp}}{(k_{\perp} - \xi q_{2\perp})^2} \right)^2 F(q_{1\perp})F(q_{2\perp}) \\
&\quad - \frac{\Lambda^2}{\Lambda^2 + (k_{\perp} - q_{1\perp} - q_{2\perp})^2} \frac{1}{(k_{\perp} - q_{1\perp} - q_{2\perp})^2} F(q_{2\perp})F(k_{\perp} - q_{2\perp}) \\
&\quad - \frac{\Lambda^2}{\Lambda^2 + (k_{\perp}/\xi - q_{2\perp})^2} \frac{1}{(k_{\perp} - \xi q_{2\perp})^2} F(q_{1\perp})F(k_{\perp}/\xi), \tag{156}
\end{aligned}$$

$$\begin{aligned}
\mathcal{T}_{qg}^{(1)}(\xi, q_{1\perp}, q_{2\perp}, k_{\perp}) &= \left(\frac{k_{\perp} - \xi q_{1\perp} - \xi q_{2\perp}}{(k_{\perp} - \xi q_{1\perp} - \xi q_{2\perp})^2} - \frac{k_{\perp} - q_{2\perp}}{(k_{\perp} - q_{2\perp})^2} \right)^2 F(q_{1\perp})F(q_{2\perp}) \\
&\quad - \frac{1}{(k_{\perp} - \xi q_{1\perp} - \xi q_{2\perp})^2} \frac{\Lambda^2}{\Lambda^2 + (k_{\perp}/\xi - q_{1\perp} - q_{2\perp})^2} F(q_{2\perp})F(k_{\perp}/\xi - q_{2\perp}) \\
&\quad - \frac{1}{(k_{\perp} - q_{2\perp})^2} \frac{\Lambda^2}{\Lambda^2 + (k_{\perp} - q_{2\perp})^2} F(q_{1\perp})F(k_{\perp}). \tag{157}
\end{aligned}$$

It is important to note that the factorization scale in σ_{resummed} now becomes Λ due to the resummation of the threshold collinear logarithms, while that in $\sigma_{\text{NLO matching}}$ remains as μ . This replacement of the factorization scale is akin to the common practice (setting μ to μ_b) in the transverse momentum-dependent distribution factorization[92].

VI. NATURAL CHOICES OF THE AUXILIARY SCALE

Here we illustrate how to determine the proper value of semi-hard scale Λ in our numerical calculations, since this scale plays an important role in numerical results. In the case of fixed coupling, we first use an intuitive method and find $\Lambda^2 \sim (1 - \xi)k_{\perp}^2$ when the threshold logarithms become important. In addition, by using the saddle point approximation, we find that the semi-hard scale Λ can be determined by dominant scale determined by the saddle point of the resummed formula in both the fixed and running couple scenarios.

A. An Intuitive Derivation with the Fixed coupling

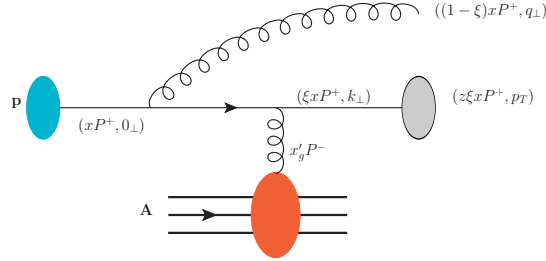


FIG. 8. The kinematics of the real gluon emission.

To illustrate the physical interpretation of the semi-hard scale Λ^2 , it is instructive to consider the real emission of gluons as shown in Fig. 8. Following the discussion outlined in Ref. [45], we use the light-cone perturbation theory and define $p^+ = \frac{p^0 + p^3}{\sqrt{2}}$ and $p^- = \frac{p^0 - p^3}{\sqrt{2}}$. According to the momentum conservation before and after the splitting, we get the following kinematic constraint for the radiated gluon in the $\xi \rightarrow 1$ limit

$$q^- = \frac{q_{\perp}^2}{2(1-\xi)x_p P^+} \leq P^- \quad \Rightarrow \quad \xi \leq 1 - \frac{x_g q_{\perp}^2}{k_{\perp}^2}. \tag{158}$$

Then the upper limit of the divergent integral of $d\xi$ should be modified as following

$$\int_0^{1 - \frac{x_g q_{\perp}^2}{k_{\perp}^2}} \frac{d\xi}{1-\xi} = \ln \frac{k_{\perp}^2}{q_{\perp}^2} + \ln \frac{1}{x_g}. \tag{159}$$

It is important to note that these two logarithms arise two physical regions. First, in the region $0 < \xi < 1 - \frac{q_\perp^2}{k_\perp^2}$ with finite longitudinal momentum q^- , one gets Sudakov logarithm $\ln \frac{k_\perp^2}{q_\perp^2}$ corresponding to real gluon emission. On the other hand, $q^- \rightarrow \infty$ in the region $1 - \frac{q_\perp^2}{k_\perp^2} < \xi < 1 - \frac{q_\perp^2}{k_\perp^2} x_g$, then one gets $\ln \frac{1}{x_g}$ which corresponds to part of the small- x evolution. For virtual gluon, there is no such requirement.

If we introduce the semi-hard scale Λ^2 to represent the typical transverse momentum associated with the Sudakov real gluon emission, then we can find that the real and virtual contributions would cancel each other in the region $q_\perp^2 \leq \Lambda^2$. When the saturation momentum is not large, this scale is estimated to be $(1 - \xi)k_\perp^2 \sim (1 - \tau)k_\perp^2$ since the real gluon emission requires $\xi < 1 - \frac{q_\perp^2}{k_\perp^2}$. On the other hand, when the saturation effect is dominant, we expect that the real and virtual contributions cancel up to the saturation momentum Q_s^2 . With these overall considerations, we choose this semi-hard scale Λ^2 to be

$$\Lambda_{\text{fixed}}^2 \simeq \max [(1 - \tau)k_\perp^2, Q_s^2] \gg \Lambda_{\text{QCD}}^2, \quad (160)$$

where the subscript ‘‘fixed’’ indicates that this expression for the auxiliary scale is derived with fixed coupling. The auxiliary scale Λ^2 in our calculation is similar to the intermediate scale μ_i^2 in SCET [89, 90]. In the region $\Lambda^2 < q_\perp^2 < k_\perp^2$, the remaining virtual contribution is found to be

$$- \int_{\Lambda^2}^{k_\perp^2} \frac{dq_\perp^2}{q_\perp^2} \ln \frac{k_\perp^2}{q_\perp^2} \Rightarrow -\frac{1}{2} \ln^2 \frac{k_\perp^2}{\Lambda^2}, \quad (161)$$

which can be identified as the Sudakov double logarithmic contribution. The above intuitive discussion of the scale choice is based on the separation of the kinematic region, and a more rigorous derivation using the saddle point approximation is provided in the next subsection. It is important to note that the Λ^2 scale can also be determined from the scale $\mu_r^2 \equiv c_0^2/r_\perp^2$ with r_\perp being the typical scale in the coordinate space. There are two competing mechanisms: the threshold soft gluon emission and the saturation effects when we try to locate the region where the dominant contribution arises. In addition, for convenience, we use a fixed estimated value of Λ^2 in the numerical evaluation for a given kinematic region.

B. Saddle Point Approximation

In addition to the above intuitive derivation, we can analytically study the choice of Λ^2 via the saddle point approximation. The saddle point approximation method, also known as the method of steepest descent, allows one to locate the region where the most important contribution arises in the resummed results and therefore identify the natural choice of Λ^2 . Similar ideas have also been used in Refs. [91–93].

To determine the value of the auxiliary scale Λ^2 in the resummed expression in Eq. (137), let us first consider the corresponding results for the $q \rightarrow q$ channel in the coordinate space

$$\begin{aligned} \frac{d\sigma_{\text{resummed}}^{qq}}{dyd^2p_T} = & S_\perp \int_\tau^1 \frac{dz}{z^2} \int \frac{d^2r_\perp}{(2\pi)^2} e^{-ik_\perp \cdot r_\perp} S^{(2)}(r_\perp) e^{-S_{\text{Sud}}^{qq}} \int_{x_p}^1 \frac{dx}{x} q(x, \mu) \frac{e^{(3/4 - \gamma_E)\gamma_{\mu_r, \mu}^q}}{\Gamma(\gamma_{\mu_r, \mu}^q)} \left[\ln \frac{x}{x_p} \right]_*^{\gamma_{\mu_r, \mu}^q - 1} \\ & \times \int_z^1 \frac{dz'}{z'} D_{h/q}(z') \frac{e^{(3/4 - \gamma_E)\gamma_{\mu_r, \mu}^q}}{\Gamma(\gamma_{\mu_r, \mu}^q)} \left[\ln \frac{z'}{z} \right]_*^{\gamma_{\mu_r, \mu}^q - 1}, \end{aligned} \quad (162)$$

with $\mu_r = c_0/r_\perp$, $c_0 = 2e^{-\gamma_E}$ and $\gamma_{\mu_r, \mu}^q = C_F \int_{\mu^2}^{\mu_r^2} \frac{d\mu'^2}{\mu'^2} \frac{\alpha_s(\mu'^2)}{\pi}$. The Sudakov factor S_{Sud}^{qq} in the coordinate space is

$$S_{\text{Sud}}^{qq} = C_F \int_{c_0^2/r_\perp^2}^{k_\perp^2} \frac{d\mu^2}{\mu^2} \frac{\alpha_s(\mu^2)}{\pi} \ln \frac{k_\perp^2}{\mu^2} - 3C_F \int_{c_0^2/r_\perp^2}^{k_\perp^2} \frac{d\mu^2}{\mu^2} \frac{\alpha_s(\mu^2)}{2\pi}. \quad (163)$$

The saddle point of the above r_\perp integral depends on both the strength of the saturation effect (given by the dipole amplitude $S^{(2)}(r_\perp)$) and the threshold resummation. To identify the corresponding saddle point of each contribution, it is convenient to rewrite above formula in terms of the convolution of the dipole gluon distribution and the threshold Sudakov factor in the momentum space as follows

$$\frac{d\sigma_{\text{resummed}}^{qq}}{dyd^2p_T} = S_\perp \int_\tau^1 \frac{dz}{z^2} \int_{x_p}^1 \frac{dx}{x} q(x, \mu) \int_z^1 \frac{dz'}{z'} D_{h/q}(z') \int d^2q_\perp F(k_\perp - q_\perp) G_{\text{th}}(q_\perp), \quad (164)$$

where $F(k_\perp - q_\perp)$ is the Fourier transform of $S^{(2)}(r_\perp)$ and

$$G_{\text{th}}(q_\perp) \equiv \int \frac{d^2 r_\perp}{(2\pi)^2} e^{-iq_\perp \cdot r_\perp} e^{-S_{\text{Sud}}^{qq}} \frac{e^{(3/4-\gamma_E)\gamma_{\mu_r, \mu}^q}}{\Gamma(\gamma_{\mu_r, \mu}^q)} \left[\ln \frac{x}{x_p} \right]_*^{\gamma_{\mu_r, \mu}^q - 1} \frac{e^{(3/4-\gamma_E)\gamma_{\mu_r, \mu}^q}}{\Gamma(\gamma_{\mu_r, \mu}^q)} \left[\ln \frac{z'}{z} \right]_*^{\gamma_{\mu_r, \mu}^q - 1}. \quad (165)$$

When k_\perp is large, the dominant contribution of Eq. (164) comes from the regions near the vicinity of $q_\perp \sim 0$ or $q_\perp \sim k_\perp$. To proceed, let us first consider the saddle point of the r_\perp integral in Eq. (165) at $q_\perp \sim 0$ as follows

$$\int_0^\infty dr_\perp^2 \exp[-S_{\text{Sud}}^{qq}] \frac{e^{2(3/4-\gamma_E)\gamma_{\mu_r, \mu}^q}}{\Gamma(\gamma_{\mu_r, \mu}^q)\Gamma(\gamma_{\mu_r, \mu}^q)} \left[\ln \frac{1}{\xi} \ln \frac{1}{\xi'} \right]_*^{\gamma_{\mu_r, \mu}^q - 1}, \quad (166)$$

where $1/\xi = x/x_p$ and $1/\xi' = z'/z$. In order to apply the saddle point approximation, we first switch the integration variable from r_\perp^2 to $\ln(r_\perp^2 \Lambda_{\text{QCD}}^2)$ so that the integration range becomes $[-\infty, +\infty]$. Second, the phase factor $e^{-iq_\perp \cdot r_\perp}$ or the Bessel function $J_0(|q_\perp||r_\perp|)$ has been removed at the $q_\perp \sim 0$ limit. Then the above integral can be cast into the following integral

$$\int_{-\infty}^{+\infty} d \ln(r_\perp^2 \Lambda_{\text{QCD}}^2) \exp[E(r_\perp)], \quad (167)$$

where the exponent is defined as

$$E(r_\perp) = \ln(r_\perp^2 \Lambda_{\text{QCD}}^2) - S_{\text{Sud}}^{qq} + 2 \left(\frac{3}{4} - \gamma_E \right) \gamma_{\mu_r, \mu}^q - 2 \ln \Gamma(\gamma_{\mu_r, \mu}^q) + \gamma_{\mu_r, \mu}^q \ln[(1-\xi)(1-\xi')]. \quad (168)$$

Here, we take the limit that $\ln \frac{1}{\xi} \approx 1 - \xi$ and $\ln \frac{1}{\xi'} \approx 1 - \xi'$ when ξ and ξ' are both close to 1. This means that both the initial state and the final state radiations are near threshold. The phase space for such scenario is quite limited. In most cases, only either the initial state radiation or the final state radiation is near threshold. Therefore, only one of ξ and ξ' is close to 1 and the other is far away from 1. Then, the term $\ln[(1-\xi)(1-\xi')]$ in the above equation should be replaced by $\ln(1-\xi)$ or $\ln(1-\xi')$ accordingly. Also, we approximately write $\ln \Gamma(x) \approx -\gamma_E x$ when x is of the order of 1. In the case of the fixed strong coupling, the saddle point r_{sp} is determined by

$$\left. \frac{dE(r_\perp)}{dr_\perp} \right|_{r_\perp=r_{\text{sp}}}^{\text{fixed } \alpha_s} = 0 \quad \Rightarrow \quad 1 - \frac{\alpha_s C_F}{\pi} \ln \frac{k_\perp^2 (1-\xi) r_{\text{sp}}^2}{c_0^2} = 0. \quad (169)$$

Solving the above equation yields the position of the saddle point, which reads

$$\mu_{\text{sp}}^2 \equiv \frac{c_0^2}{r_{\text{sp}}^2} = k_\perp^2 (1-\xi) \exp \left[-\frac{\pi}{\alpha_s C_F} \right]. \quad (170)$$

This indicates that the nature choice of Λ^2 is roughly $k_\perp^2 (1-\xi)$. This result parametrically agrees with the choice of the semi-hard scale Λ^2 discussed in our previous intuitive derivation and the intermediate scale μ_i suggested in Refs. [89, 90].

Similarly, we consider the case for the running coupling and write down the $E(r_\perp)$ function explicitly as follows,

$$E(r_\perp) = \ln(r_\perp^2 \Lambda_{\text{QCD}}^2) + \frac{C_F}{N_c \beta_0} \ln \frac{k_\perp^2}{\Lambda_{\text{QCD}}^2} \ln \ln \frac{c_0^2}{r_\perp^2 \Lambda_{\text{QCD}}^2} + \frac{C_F}{N_c \beta_0} \ln \frac{k_\perp^2 r_\perp^2}{c_0^2} + \frac{C_F}{N_c \beta_0} \left[\ln \ln \frac{c_0^2}{r_\perp^2 \Lambda_{\text{QCD}}^2} \right] \ln(1-\xi) + \dots, \quad (171)$$

where $\beta_0 = \frac{11}{12} - \frac{n_f}{6N_c}$. Here, we have only kept the r_\perp -dependent terms. Then we find the saddle point as

$$\mu_{\text{sp}}^2 \equiv \frac{c_0^2}{r_{\text{sp}}^2} = \Lambda_{\text{QCD}}^2 \left[\frac{k_\perp^2 (1-\xi)}{\Lambda_{\text{QCD}}^2} \right]^{\frac{C_F}{C_F + N_c \beta_0}}. \quad (172)$$

This result is in line with the saddle point found in Ref. [92] in the so-called CSS formalism. In particular, if we replace $k_\perp^2 (1-\xi)(1-\xi')$ with Q^2 and set $C_F = 4/3$, $N_c = 3$ and $n_f = 5$, we can exactly reproduce the result in Ref. [92] and find $\frac{1}{\mu_{\text{sp}}} = \frac{1}{\Lambda_{\text{QCD}}} \left[\frac{Q}{\Lambda_{\text{QCD}}} \right]^{-0.41}$.

Next, let us study $F(k_\perp - q_\perp)$ in the second region where $q_\perp \sim k_\perp$, and find the saddle point in the r_\perp integral involving the dipole gluon distribution. In this case with $q_\perp \sim k_\perp$, the phase factor $e^{-i(k_\perp - q_\perp) \cdot r_\perp}$ or the Bessel function $J_0(|k_\perp - q_\perp||r_\perp|)$ can set to 1. The integral of interest becomes

$$\int_0^\infty dr_\perp^2 S^{(2)}(r_\perp) = \int_0^\infty dr_\perp^2 \exp\left[-\frac{1}{4}Q_s^2 r_\perp^2\right] = \int_{-\infty}^{+\infty} d \ln(r_\perp^2 \Lambda_{\text{QCD}}^2) \exp\left[\ln(r_\perp^2 \Lambda_{\text{QCD}}^2) - \frac{1}{4}Q_s^2 r_\perp^2\right], \quad (173)$$

where $S^{(2)}(r_\perp)$ is approximately equal to $\exp[-\frac{1}{4}Q_s^2 r_\perp^2]$ as suggested in the GBW model for the dipole scattering amplitude with Q_s the saturation momentum. It is clear that the saddle point of this integral locates at $\frac{1}{r_{\text{sp}}^2} = \frac{Q_s^2}{4}$. In the low momentum region where $q_\perp \sim k_\perp$, the GBW model usually provides a good description of the transverse momentum distribution for $F(k_\perp - q_\perp)$, while it does not have the power law tail in the high q_\perp region.

To summarize, the semi-hard auxiliary scale Λ^2 in Eq. (137) is determined by the dominant region of r_\perp -integral in Eq. (162). Physically speaking, there are two competing mechanisms which controls the r_\perp integral in Eq. (162). When the final state jet transverse momentum k_\perp mainly comes from the dipole gluon distribution, we find that the semi-hard scale is given by Eq. (172). On the other hand, when the saturation effect is strong, we can see that the typical semi-hard scale should be of the order Q_s^2 . Near the kinematic threshold when k_\perp is large, we need to minimize the typical r_\perp in Eq. (162) to avoid strong cancellation caused by the oscillation phase factor. Thus, the dominant contribution to the whole integral in Eq. (162) comes from the larger scale of these two, or equivalently speaking, the smaller r_{sp} . Therefore, we arrive at the following quantitative prescription for the choice of Λ^2

$$\Lambda^2 \approx \max\left\{\Lambda_{\text{QCD}}^2 \left[\frac{k_\perp^2(1-\xi)}{\Lambda_{\text{QCD}}^2}\right]^{\frac{C_F}{C_F+N_c\beta_0}}, Q_s^2\right\}. \quad (174)$$

To get the result for the $g \rightarrow g$ channel, we only need to replace the color factor C_F with N_c .

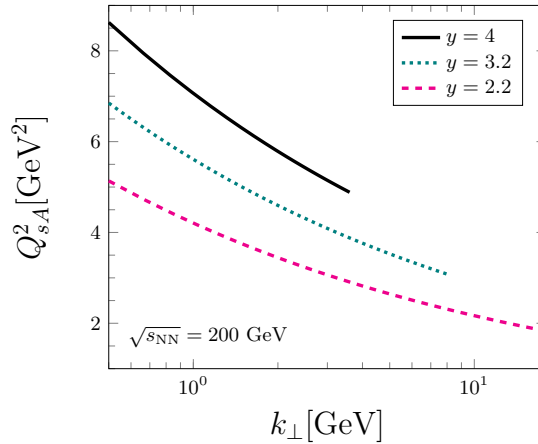


FIG. 9. Saturation momentum square $Q_{sA}^2 = 5Q_{sp}^2(x_g)$ as a function of k_\perp at different rapidities in the GBW model.

It is time to use Eq. (174) to estimate the natural choices of the auxiliary scale Λ^2 in various kinematic regions. At the RHIC energy, one can take the typical $k_\perp \sim 10$ GeV. Assuming $1 - \xi \sim 0.5$, the saddle point of the first region is $\mu_{\text{sp}}^2 \sim 0.7$ GeV² for the $q \rightarrow q$ channel. To obtain the above numbers, we have used $n_f = 4$ and $\Lambda_{\text{QCD}} = 0.15$ GeV. For the $g \rightarrow g$ channel, the value becomes 2 GeV², which is not large either. In the large- x region, the cross-section is dominated by the quark channel since the quark density is much larger than the gluon density. Therefore, the scale Λ^2 at the RHIC energy is mainly determined by the saturation momentum in dAu collisions. In our numerical evaluation, we employ the GBW model to estimate the saturation momentum, which is given by[96]

$$Q_{sp}^2(x_g) = Q_0^2 \left(\frac{x_0}{x_g}\right)^\lambda, \quad (175)$$

where $x_g = \frac{k_\perp}{\sqrt{s_{\text{NN}}}} e^{-y}$, $x_0 = 3.04 \times 10^{-4}$, $\lambda = 0.288$ and $Q_0^2 = 1$ GeV². For the gold nucleus target, we use $Q_{sA}^2(x_g) = 5Q_{sp}^2(x_g)$ and show the saturation momentum as a function of k_\perp at different rapidities in Fig. 9. The corresponding saturation momentum for the proton target in pp collisions is only 1/5 of the values shown in Fig. 9.

The semi-hard scale, Λ^2 , needs to be much larger than Λ_{QCD}^2 . Therefore, we choose it to be a few times smaller than that in dAu collisions but still larger than 1 GeV^2 . We show the values of Λ^2 used to compute the cross-sections at the RHIC energy in Table I.

TABLE I. Values of Λ^2 in calculating the cross-sections at $\sqrt{s_{\text{NN}}} = 200 \text{ GeV}$ at RHIC.

Rapidity	$y = 2.2$		$y = 3.2$		$y = 4$	
Collisional systems	dAu	pp	dAu	pp	dAu	pp
$\Lambda^2 \text{ (GeV}^2\text{)}$	$2 \sim 4$	~ 1	$3 \sim 7$	~ 2	$5 \sim 9$	~ 3

At the LHC energy, the typical k_{\perp} is usually very large. Taking $k_{\perp} \sim 100 \text{ GeV}$ and $1 - \xi \sim 0.5$, we find $\Lambda^2 \sim 4 \text{ GeV}^2$ for $q \rightarrow q$ channel and $\Lambda^2 \sim 30 \text{ GeV}^2$ for $g \rightarrow g$ channel. Since the $g \rightarrow g$ channel becomes more important at the LHC energy, we choose Λ^2 to be 20 GeV^2 at $\sqrt{s} = 5.02 \text{ TeV}$ and set Λ^2 to be 40 GeV^2 at $\sqrt{s} = 13 \text{ TeV}$.

In principle, we expect that the dependence on the auxiliary scale is mild except for case in the threshold region where the resummed result gets enhanced by the threshold resummation. In Fig. 10, the Λ^2 -dependence of the resummed cross-sections at different collisional energies are presented. In general, the Λ^2 -dependence is strong when the threshold resummation is important (i.e., when p_T is closer to the kinematic threshold). Furthermore, at given p_T , the resummed cross-section increases with decreasing Λ^2 due to increased threshold logarithms. These effects are manifest at the RHIC energy as shown in the left panel of Fig. 10. At the RHIC energy, we see clearly that the Λ^2 -dependence becomes stronger at larger p_T . Taking into account that the maximum p_T allowed by the kinematics is just around 8 GeV at $y = 3.2$, the threshold resummation is actually vital at large p_T . At low p_T , the resummed cross-section is less sensitive to the value of Λ^2 . At the LHC energy, the p_T regions that we are interested in are actually still far away from the kinematic threshold. Therefore, as shown in the right panel of Fig. 10, the Λ^2 dependence in the resummed cross-section is rather mild.

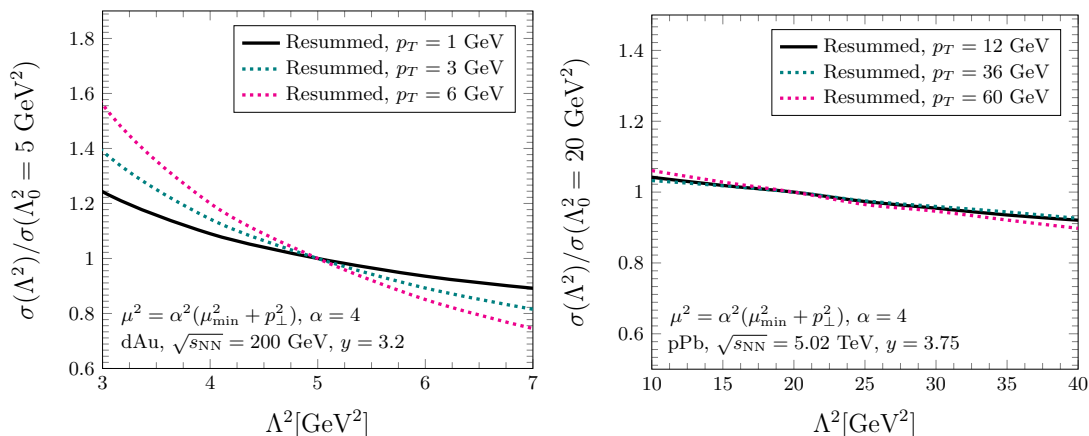


FIG. 10. The ratios of the resummed cross-section to the reference cross-section at certain value of Λ_0^2 as a function of Λ^2 at $\sqrt{s_{\text{NN}}} = 200 \text{ GeV}$ (the left plot) and $\sqrt{s_{\text{NN}}} = 5.02 \text{ TeV}$ (the right plot). At the RHIC energy, we choose $\Lambda_0^2 = 5 \text{ GeV}^2$, while we set $\Lambda_0^2 = 20 \text{ GeV}^2$ at the LHC.

VII. DIPOLE SCATTERING AMPLITUDE AND SMALL- x GLUON DISTRIBUTION

In the above derivation, the dipole gluon distribution $F(\eta, k_{\perp})$ is defined as the Fourier transform of the dipole scattering amplitude $S_{x_g}^{(2)}(r_{\perp})$ in the fundamental representation, where $\eta = \ln \frac{x_0}{x_g}$ is the rapidity range of the small- x evolution with $x_0 = 0.01$. Conventionally, we evolve the dipole scattering amplitude with initial condition starting from $x_g = x_0 = 0.01$ in the CGC formalism. This means that we usually assume that the CGC formalism starts to apply when $x_g < x_0$. The dimension of $F(\eta, k_{\perp})$ is GeV^{-2} . It is related to $\mathcal{F}^{x_g}(k_{\perp})$ by $F(\eta, k_{\perp}) = \mathcal{F}^{x_g}(k_{\perp})/S_{\perp}$. In principle, $F(\eta, k_{\perp})$ and $S_{x_g}^{(2)}(r_{\perp})$ implicitly depend on x_g . In the previous sections, we have suppressed the x_g or η dependence for simplicity. In our numerical implementation, we define $S_{x_g}^{(2)}(r_{\perp}) = 1 - N(\eta, r_{\perp})$. Here $N(\eta, r_{\perp})$ is the

solution to the rcBK evolution equation [100–107], which is given by

$$\frac{dN(\eta, r_\perp)}{d\eta} = \int d^2 r_{1\perp} \mathcal{K}_{\text{BK}}(r_\perp, r_{1\perp}, r_{2\perp}) [N(\eta, r_{1\perp}) + N(\eta, r_{2\perp}) - N(\eta, r_\perp) - N(\eta, r_{1\perp})N(\eta, r_{2\perp})], \quad (176)$$

where $r_{2\perp} \equiv r_\perp - r_{1\perp}$. We employ the approach proposed in Ref. [103] to take into account the running coupling corrections. The BK evolution kernel, \mathcal{K}_{BK} , is then given by

$$\mathcal{K}_{\text{BK}}(r_\perp, r_{1\perp}, r_{2\perp}) = \frac{\alpha_s(r_\perp) N_c}{2\pi^2} \left[\frac{r_\perp^2}{r_{1\perp}^2 r_{2\perp}^2} + \frac{\alpha_s(r_{1\perp}) - \alpha_s(r_{2\perp})}{\alpha_s(r_{2\perp})} \frac{1}{r_{1\perp}^2} + \frac{\alpha_s(r_{2\perp}) - \alpha_s(r_{1\perp})}{\alpha_s(r_{1\perp})} \frac{1}{r_{2\perp}^2} \right], \quad (177)$$

where

$$\alpha_s(r_\perp) = \frac{4\pi}{(11 - \frac{2}{3}n_f) \ln \frac{4}{a_0^2 r_\perp^2}}, \quad (178)$$

with $a_0 = 0.2$ GeV, $n_f = 3$, $r_*^2 = \frac{r_\perp^2}{1+r_\perp^2/r_{\text{max}}^2}$ and $r_{\text{max}} = 5$ GeV⁻¹. This method is similar to the b_* -prescription in the well-known Collins-Soper-Sterman (CSS) formalism and it has also been implemented in Ref. [109]. It ensures a smooth transition from the perturbative region to the infrared regime and freezes the strong coupling constant in the long distance limit. The numerical solution of the rcBK equation with this prescription for $\alpha_s(r_\perp)$ is quite close to that with the conventional method where α_s is frozen at a certain value. We set r_{max} to be 5 GeV⁻¹, so that $\alpha_s(r_\perp \rightarrow \infty) = 1$, which is in line with Ref. [100].

The above rcBK evolution equation can be solved numerically with a given initial condition. In our calculation, we employ the initial condition given by the modified McLerran-Venugopalan model [100, 108]

$$N(\eta = 0, r_\perp) = 1 - \exp \left[-\frac{1}{4} (r_\perp^2 Q_{s0}^2)^\gamma \ln \left(e + \frac{1}{|r_\perp| \Lambda_{\text{BK}}} \right) \right], \quad (179)$$

where $\gamma = 1.118$ and $\Lambda_{\text{BK}} = 0.24$ GeV. Here Λ_{BK} is used to regulate the infrared physics, and it is usually interpreted as the QCD scale Λ_{QCD} . As one of the two parameters in the modified MV model for the initial condition, we use the value [108] $\Lambda_{\text{BK}} = 0.24$ GeV close to Λ_{QCD} which determines the one-loop running coupling in calculating the NLO hard factors. This initial condition is identical to the one used in Ref. [100] and it is extracted from the global analysis to the HERA data. Following Ref. [100], we use $Q_{sp0}^2 = 0.16$ GeV² for a proton target and set $Q_{sA0}^2 = 5Q_{sp0}^2$ for a gold/lead nucleus target for the initial condition, and then solve the above rcBK evolution equation numerically.

The Fourier transform of the sample solutions are shown in Fig. 11, and they agree with previous numerical results well. In the high k_\perp regime, it is quite challenging to obtain a smooth curve for $F(\eta, k_\perp)$. This is due to the rapid oscillation of the Bessel function when k_\perp is large and insufficient numerical accuracies. In general, this kind of oscillatory behavior can be mitigated with more computing resources. Nevertheless, in fact, we know that the high k_\perp

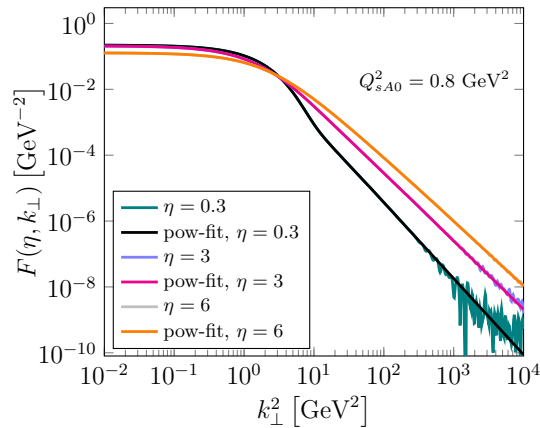


FIG. 11. The numerical Fourier transform of $S_{x_g}^{(2)}(r_\perp)$ compared with the power-law fit in the high k_\perp region. The oscillating curves indicate that the direct numerical Fourier transform is inaccurate at high k_\perp and they are the artifacts of limited sampling. The power-law fit method is used to capture the key feature of $F(\eta, k_\perp)$ in the high k_\perp region and remove the non-physical oscillation.

tail of $F(\eta, k_\perp)$ behaves like a power law. Therefore, in practice, we perform the power-law fit to the numerical result of $F(\eta, k_\perp)$ in the high k_\perp region and smoothly connect to the numerical solution at low k_\perp . The use of the gluon distribution $F(\eta, k_\perp)$ with the power-law fit can significantly improve the numerical accuracy with limited computing resources.

VIII. ESTIMATING THEORETICAL UNCERTAINTIES

It is straightforward to find that the μ^2 and Λ^2 dependences in our calculation exactly vanish at the one-loop order. The residual scale dependences come in terms of higher order corrections in our calculation are due to the truncation of the perturbative expansion of the hard factor. The exact all order results, if they are available, are expected to be independent of the factorization scale and the auxiliary scale. Since we only manage to explicitly obtain the NLO hard factor and we truncate the perturbative expansion of the hard factor at the α_s order, there are still some residual dependence on these two scales in our resummed formalism. Nevertheless, it is the common practice in QCD calculations to use the residual dependence to estimate the unknown higher order corrections. In this paper, we estimate the uncertainty in the theoretical calculation by varying the factorization scale μ^2 from $4(\mu_{\min}^2 + p_T^2)$ to $16(\mu_{\min}^2 + p_T^2)$ and changing Λ^2 within estimated ranges. Although the uncertainties of PDFs and FFs from the global analysis may also contribute, they are not included in our analysis.

While estimating the theoretical uncertainties for differential cross-sections is straightforward, the case for the nuclear modification factor R_{pA} is a bit tricky. R_{pA} is defined as $R_{pA} = \frac{1}{A}\sigma_{pA}/\sigma_{pp}$, which involves the ratio of the pA and pp cross-sections. Experimentally, the measurements of these two cross-sections are independent. On the other hand, in our calculation, they are computed from the same NLO cross-section in the CGC formalism with different initial conditions for the target k_\perp dependent small- x gluon distribution. Therefore, there is some certain level of correlation between theoretical uncertainties of σ_{pA} and σ_{pp} when we vary scales.

We use $\delta\sigma_{pA}$ and $\delta\sigma_{pp}$ to represent the theoretical uncertainties of σ_{pA} and σ_{pp} correspondingly. To estimate the theoretical uncertainty of R_{pA} , which is denoted as δR , we need to introduce the correlation between σ_{pA} and σ_{pp} which is denoted as $\mathcal{C}(\sigma_{pA}, \sigma_{pp})$. The uncertainty of R_{pA} is then given by

$$\frac{\delta R}{R_{pA}} = \sqrt{\left(\frac{\delta\sigma_{pA}}{\sigma_{pA}}\right)^2 + \left(\frac{\delta\sigma_{pp}}{\sigma_{pp}}\right)^2 - 2\mathcal{C}(\sigma_{pA}, \sigma_{pp})\frac{\delta\sigma_{pA}}{\sigma_{pA}}\frac{\delta\sigma_{pp}}{\sigma_{pp}}}. \quad (180)$$

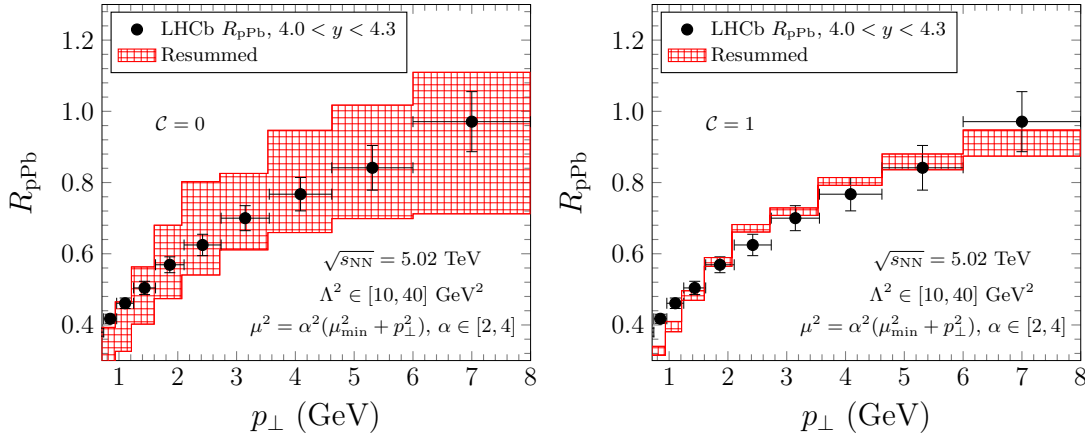


FIG. 12. Estimates of the theoretical uncertainty for R_{pPb} in two extreme scenarios compared with the LHCb data [28].

Let us consider two extreme scenarios: (1) σ_{pA} and σ_{pp} are uncorrelated; (2) σ_{pA} and σ_{pp} are completely correlated. $\mathcal{C}(\sigma_{pA}, \sigma_{pp}) = 0$ in the first scenario while $\mathcal{C}(\sigma_{pA}, \sigma_{pp}) = 1$ in the latter. We present our estimates of the theoretical uncertainty for R_{pPb} in these two extreme scenarios compared with the LHCb data in Fig. 12. Clearly, if σ_{pA} and σ_{pp} are uncorrelated, the uncertainties in these two accumulates. This leads to sizable uncertainties in the final results, as shown in the left panel of Fig. 12. However, if σ_{pA} and σ_{pp} are completely correlated, the uncertainties largely cancel. Therefore, the uncertainty band in the right panel of Fig. 12 is excessively narrow. The actual scenario should be somewhere in-between. In our numerical evaluation, the theoretical uncertainties of R_{pPb} are estimated from the ratios of upper bands of σ_{pA} and σ_{pp} and those of the lower bands. This simple prescription gives error bands close

to the second scenario with the perfect correlation ($\mathcal{C}(\sigma_{pA}, \sigma_{pp}) = 1$). This result can be viewed as the sign that there exists a strong correlation between σ_{pA} and σ_{pp} in our numerical calculations.

IX. RELATING THE NUMERICAL RESULTS TO THE EXPERIMENTAL DATA

In this section, we discuss in detail how to relate our numerical results to experimental measurements, and provide a systematical description of all relevant data with the chosen initial condition and a uniform set of parameters.

Let us first briefly summarize the numerical implementation of threshold resummation for the inclusive hadron production in forward pp/pA collisions. We perform the numerical calculations in the momentum space, since the evaluation in the coordinate space is quite demanding on computation resources and it may result in sizable uncertainties. The LO and one-loop cross-sections are given in Sec. I, and the resummed cross-section is given in Sec. V. We employ the one-loop running coupling for the strong coupling α_s , which is given by

$$\alpha_s(\mu^2) = \frac{4\pi}{\left(11 - \frac{2n_f}{3}\right) \ln \frac{\mu^2}{\Lambda_{\text{QCD}}^2}}, \quad (181)$$

where the number of active flavor $n_f = 4$ and $\Lambda_{\text{QCD}} = 0.15$ GeV. With this set of parameters, we set the one-loop running coupling at the Z pole to be $\alpha_s(\mu = M_Z = 91.2\text{GeV}) = 0.118$. The dipole scattering amplitude, $S^{(2)}(r_\perp)$, is obtained by solving the rcBK evolution equation with the initial condition provided by Ref. [100]. The dipole gluon distribution $F(k_\perp)$ is the Fourier transform of $S^{(2)}(r_\perp)$. For more details, we refer the reader to Sec. VII. Additionally, We utilise the NLO MSTW PDFs [94] and NLO DEHSS FFs [95] in our numerical evaluation.

On the theoretical calculation side, we execute the numerical implementation mentioned above and numerically calculate the differential cross-section of π^0 production divided by the overlapping transverse area S_\perp of the collision, which reads

$$\frac{1}{S_\perp} \frac{1}{2\pi p_T} \frac{d^2\sigma^{pA \rightarrow \pi X}}{dy dp_T}. \quad (182)$$

On the experimental side, the BRAHMS [19], ALICE [25] and ATLAS [26] collaborations measure the hadron yield, which is related to the differential cross-section as follows

$$\frac{1}{2\pi p_T} \frac{d^2 N^{pA \rightarrow hX}}{dy dp_T} = \frac{1}{\sigma_{\text{inel}}} \frac{1}{2\pi p_T} \frac{d^2 \sigma^{pA \rightarrow hX}}{dy dp_T}, \quad (183)$$

where h represents various kinds of hadrons measured in different experiments and σ_{inel} represents the total inelastic cross-section. Therefore, our results need to be multiplied by a factor of $\frac{\sigma^h}{\sigma^\pi} \frac{S_\perp}{\sigma_{\text{inel}}}$ to compare with these data, where σ^h/σ^π is the rescale factor converting the π cross-section calculated in our code to the measured hadron h yields in experiments. We use $\sigma_{\text{inel}} = 2400$ mb in dAu collisions at $\sqrt{s_{\text{NN}}} = 200$ GeV [19] and $\sigma_{\text{inel}} = 2100$ mb in pPb collisions which is measured with at least one charged hadron locating in the range of $2.5 \leq y \leq 4.5$ at the LHC energy [28]. In the pA/dA collisions, we approximately set S_\perp as the transverse area of the target nucleus, since the size of the nucleus is much larger than that of the proton/deuteron. Therefore, we utilize $S_\perp = 1770$ mb in dAu collisions [45] and $S_\perp = 1830$ mb in pPb collisions. For the ratio σ^h/σ^π , we summarize the parameters used in our numerical evaluations in Table II.

TABLE II. List of input values of parameters used in our numerical evaluations.

Experiment	BRAHMS	STAR	ATLAS/ALICE	LHCb
Hadron h	h^-	π^0	h^\pm	prompt h^\pm
σ^h/σ^π	1.3	1	2.2	2.2×0.85

Meanwhile, the STAR [20] and LHCb [27, 28] collaborations directly publish the differential cross-section in the following form

$$\frac{1}{2\pi p_T} \frac{d^2\sigma^{pA \rightarrow hX}}{dy dp_T}. \quad (184)$$

Therefore, only a factor of $\frac{\sigma^h}{\sigma^\pi} S_\perp$ is multiplied to our numerical result before it is compared with these experimental data. To account for the fraction of the prompt charged particles measured by the LHCb collaboration [27], we multiply a factor of 0.85 to the total cross section for charged hadrons as given in the end of Table II.

The connection between theoretical calculations and experimental measurements that we adopt remains the same for pp collisions. However, the overlapping transverse area S_{\perp} needs to be recalibrated in pp collisions, since the approximation which assumes that the size of the target (proton) is much larger than that of the proton projectile is no longer valid. In our calculation, the transverse area S_{\perp}^{pp} becomes a parameter fitted from the data. Typically, its value is expected to vary from πR_p^2 to $4\pi R_p^2$ with R_p being the proton radius. By using $S_{\perp}^{pp} = 2\pi(0.9 \text{ fm})^2 = 51 \text{ mb}$ in our numerical evaluation, we find that we can describe the experimental data measured in pp collisions. Furthermore, this value of S_{\perp}^{pp} is close to $\sigma_{\text{inel}} = 41 \text{ mb}$ measured by the BRAHMS collaboration in pp collisions [19].

X. ADDITIONAL NUMERICAL RESULTS

In the end, we numerically evaluate the ‘‘LO’’, ‘‘one-loop’’, and the ‘‘resummed’’ NLO cross-sections in the large N_c limit and compare these theoretical curves with RHIC and the LHC data in the plots presented in the main text and additional ones shown below. We set $C_F = N_c/2 = 3/2$ in our numerical calculation due to the large N_c limit. It is worth-noting that the large N_c approximation is essential since it allows one to significantly simplify both the analytic and numerical calculations.

As shown above, the threshold resummation helps us systematically take all order threshold logarithms into account and thus restore predictive power for the one-loop CGC calculations. After including the threshold resummation with the proper choice of the initial condition and scales, the NLO CGC calculation can describe the data from RHIC and the LHC across a wide range of p_T regions and collisional energies as shown above in the main text. In contrast to the LO and one-loop results, the resummed NLO result allows us to make more robust and reliable predictions.

At the last section of the supplemental material, we provide a lot of additional numerical results and compare the LO, one-loop, and resummed NLO CGC calculations with the rest of all the available data measured in pA (dAu) and pp collisions at RHIC and the LHC. As the closing remark, we discuss the applicable regions of the CGC formalism and point out that the small- x calculation may be only valid in the low- p_T region if the rapidity y of the measured hadron is not sufficiently large.

In our numerical evaluation, we always choose the so-called ‘‘fixed boundary condition’’ which sets $\mathcal{F}^{x_g}(k_{\perp})$ to 0 when $x_g > 0.01$ and restricts our calculation in the dilute-dense framework. As a comparison in Sec. X C, we also present the ‘‘frozen boundary condition’’ which freezes $\mathcal{F}^{x_g}(k_{\perp})$ at $x_g = 0.01$ and demonstrate that these two prescriptions lead to little difference numerically in the small- p_T region. One expect that the results from these two prescriptions become distinguishable at high p_T for hadron productions with $y < 2.3$. This can be another sign that our NLO CGC should no longer apply.

A. Supplementary Numerical Results for Forward Hadron Productions in pA Collisions

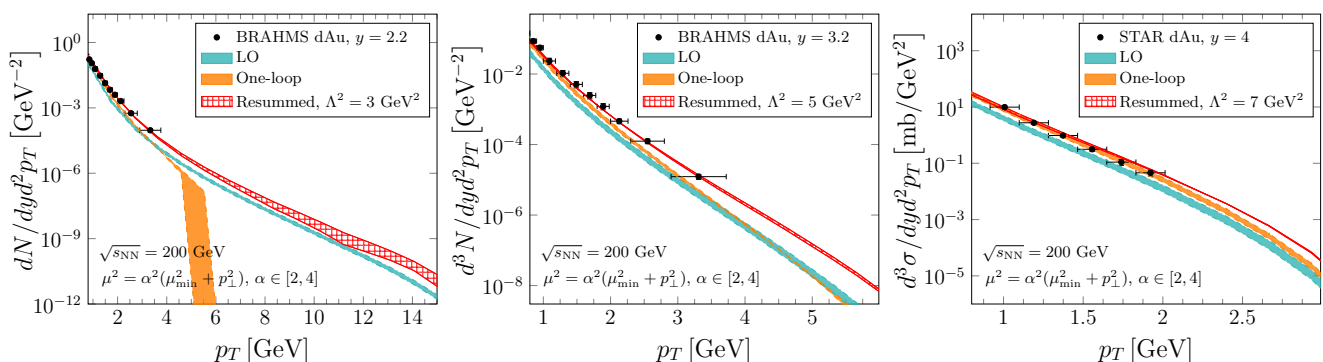


FIG. 13. Comparisons of the RHIC dAu data [19, 20] measured by the BRAHMS and STAR collaborations with the CGC calculations at fixed values of the auxiliary scale Λ . The error bands are obtained by varying the factorization scale μ^2 .

As discussed briefly earlier in the main text, the inclusive hadron production in forward pA collisions is an ideal process to probe the onset of the gluon saturation phenomenon. In the dilute-dense factorization, the LO calculation is simple and intuitive. However, it contains a rather strong dependence on the choice of the factorization scale μ , and thus it alone can not reliably describe all the experimental data. The comparison between the LO results (represented by teal bands) and experimental data are shown in Fig. 13 and Fig 14.

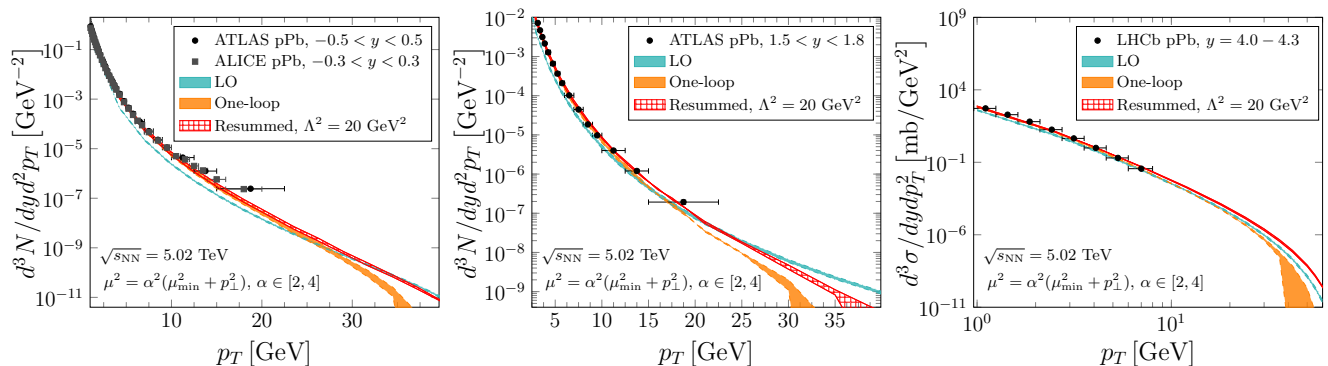


FIG. 14. Comparisons of the LHC pPb data [25, 26, 28] measured by the ALICE, ATLAS and LHCb collaborations with the CGC calculations with fixed Λ scales.

The NLO corrections significantly reduces the μ dependence. The numerical calculations at the one-loop order have already been carried out in the previous works [40, 45]. The major issue of the one-loop cross-section is that it turns negative at high- p_T near the threshold region. This negative cross-section issue, as illustrated by the orange bands in the left plot of Fig. 13 for RHIC energy and plots in Fig 14 for the LHC energy at 5TeV, has attracted a lot of attentions in the community. It becomes manifest that the one-loop cross section consistently turns negative at sufficiently large p_T in the forward rapidity region near the threshold. According to our numerical results, the threshold logarithmic terms are negligible at low p_T , whereas they become the dominant contribution in the high p_T region with $p_T \gg Q_s$. At RHIC, since the saturation momentum increases and the kinematic limit of p_T decreases with increasing rapidity y , the issue of negative one-loop results becomes less severe in the more forward region. For the rapidity bin around $y = 4$, the negativity does not appear due to the lack of phase space for p_T . As laid out above, one can systematically resolve this issue through the implementation of the threshold resummation.

In Fig. 13, we show the comparison between our numerical results and experimental data measured by the BRAHMS and STAR collaborations for dAu collisions at RHIC in three rapidity bins around $y = 2.2, 3.2$ and 4. The resummed calculation has two parameters: the factorization scale μ and the semi-hard auxiliary scale Λ . The proper and natural choice of the Λ scale is discussed in Sec. VIB, and the numerical values in different kinematic regions are shown in Table I. The central values in Table I are used in the numerical evaluation. To estimate the theoretical uncertainties at NLO order, we vary the factorization scale μ^2 from $4(\mu_{\min}^2 + p_T^2)$ to $16(\mu_{\min}^2 + p_T^2)$ with $\mu_{\min} = 2$ GeV. Remarkably, the resummed calculation not only fixes the negative problem but also improves the quality of the description of the experimental data.

In Fig. 14, we present the numerical results for pPb collisions at the LHC measured by the ALICE, ATLAS and LHCb collaborations in three rapidity bins near $y = 0, 1.65$ and 4.15. In the first two middle rapidity regions, our framework can only be applied in the small- p_T region. At high- p_T , our numerical results start to deviate from the experimental data since the so-called dilute-dense factorization framework breaks down. More detailed discussions of the applicable windows of our calculation are provided in Sec. XC. Nonetheless, our numerical results yield robust predictions and agree with the experimental data well in the middle rapidity and low- p_T region and in the forward rapidity regime for the entire p_T range.

B. Numerical Results for Forward Hadron Productions in pp Collisions

In principle, the dilute-dense factorization employed in this paper only requires that the gluon density in the target hadron is much higher than the parton density in the projectile. For pp collisions, as long as the rapidity y is sufficiently large (roughly 2), this requirement can be met. However, as briefly mentioned above, our calculation may not be directly applied to the forward hadron productions pp collisions since we have also assumed that the size of the target hadron (nucleus) is much larger than that of the projectile proton. This simplification allows us to neglect the impact parameter (b_\perp) dependence in the dipole scattering amplitude $S^{(2)}(r_\perp)$ and integrate over the impact parameter b_\perp freely. This integral results in an overall normalization S_\perp . In pA collisions, S_\perp is approximately the transverse area of the target nucleus. Nevertheless, in pp collisions, S_\perp is supposed to be the overlapping transverse area in which the inelastic pp collision occurs and it is close to the total inelastic cross-section, which is estimated to be a couple times of the target proton transverse area πR_p^2 . Therefore, this overall normalization is less constrained in pp collisions.

After setting $S_\perp^{pp} = 2\pi R_p^2$, we find that our resummed numerical results, which are shown in Figs. 15 and 16, can

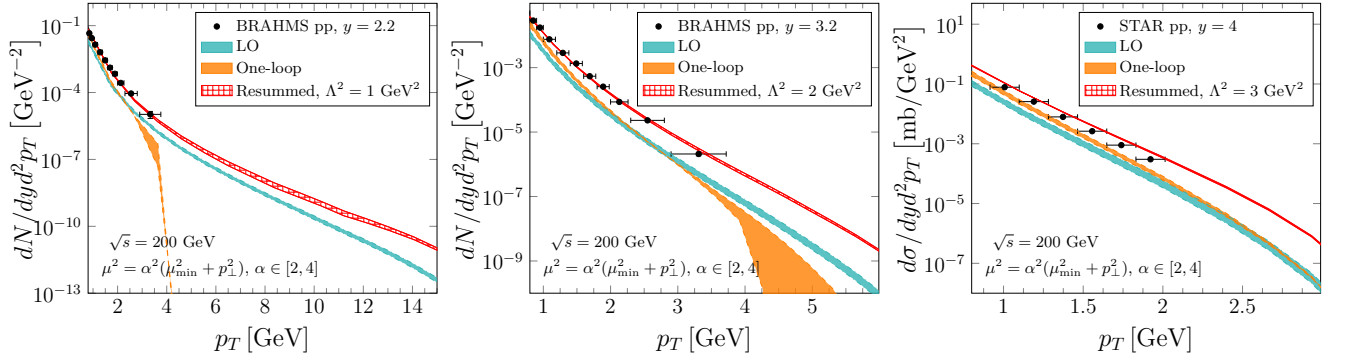


FIG. 15. Comparisons of the RHIC pp data [19, 20] from the BRAHMS and STAR collaborations with our CGC calculations.

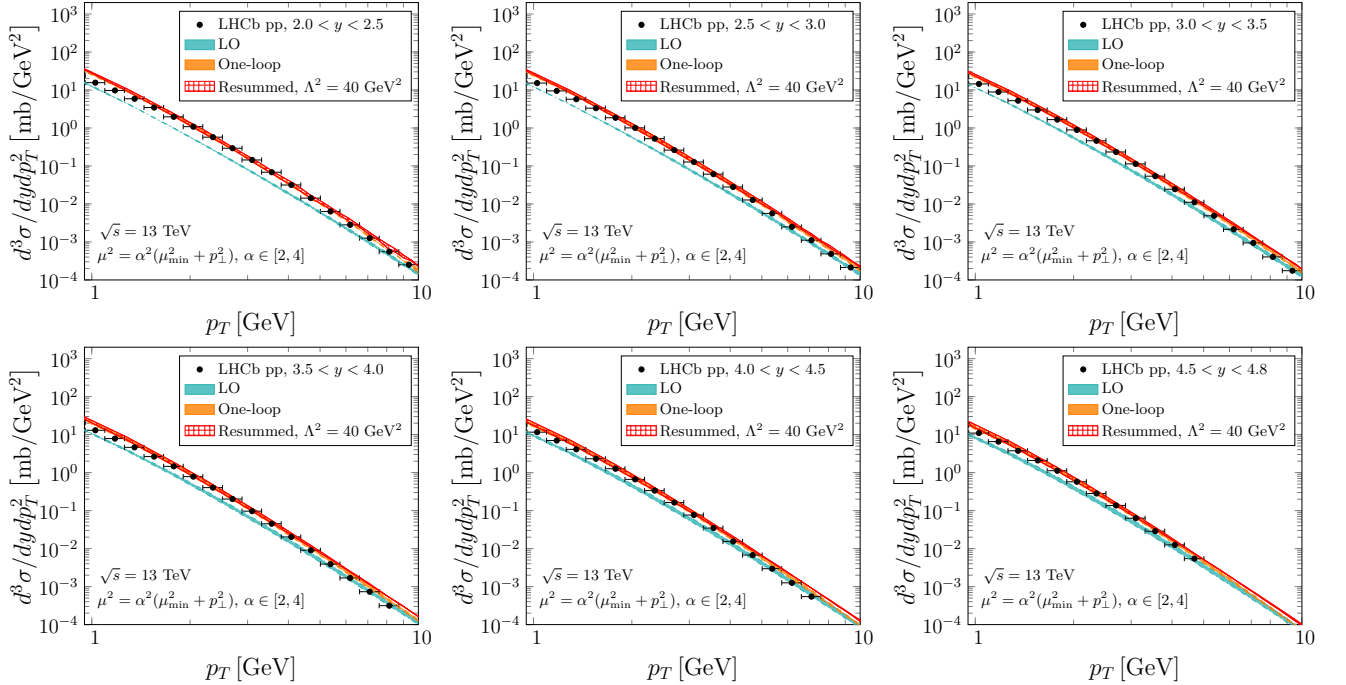


FIG. 16. Comparisons of the LHCb pp data [27] with our CGC calculations at $\sqrt{s} = 13$ TeV.

consistently describe the pp data from RHIC at $\sqrt{s_{NN}} = 200$ GeV and the recent data measured by LHCb collaboration at $\sqrt{s_{NN}} = 13$ TeV for all of the forward rapidity bins.

Furthermore, due to the rather small saturation momenta in the target proton, the issue of the negative cross-section sets in earlier for the one-loop results in the $p_T \gg Q_s$ region as compared to the case in dAu collisions at RHIC. This can be seen in the left and middle plots of Fig. 15. Nevertheless, with proper choice of the auxiliary scale Λ , the resummed results can resolve this issue and restore the predictive power of the CGC NLO calculation in the $p_T \gg Q_s$ region. In comparison, due to the much larger phase space in high energy collisions at the LHC, the negativity issue is much less severe in the observed p_T regions shown in Fig. 16. At the LHC energy, one needs to proceed to a much higher p_T in order to approach the threshold limit, where the negative contributions in the one-loop result start to become dominant.

C. The applicable range of the CGC phenomenology

This subsection is devoted to the discussion on the applicable region of the CGC calculation in forward hadron productions. More specifically, the dilute-dense factorization used in this work requires that the parton density in the nucleus target is much denser than that in the proton projectile. The deep inelastic scattering experimental data

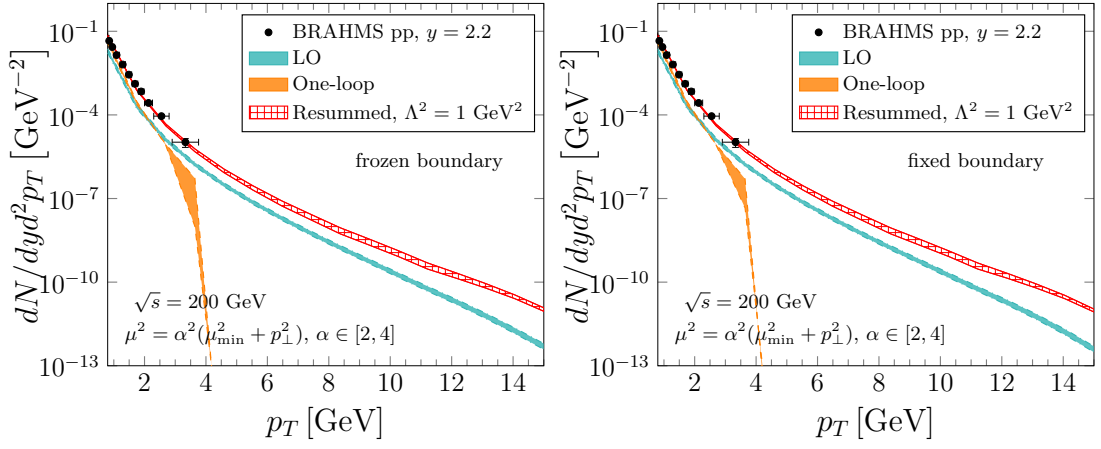


FIG. 17. Comparisons of numerical results with two different boundary conditions at $\sqrt{s} = 200$ GeV in pp collisions[19].

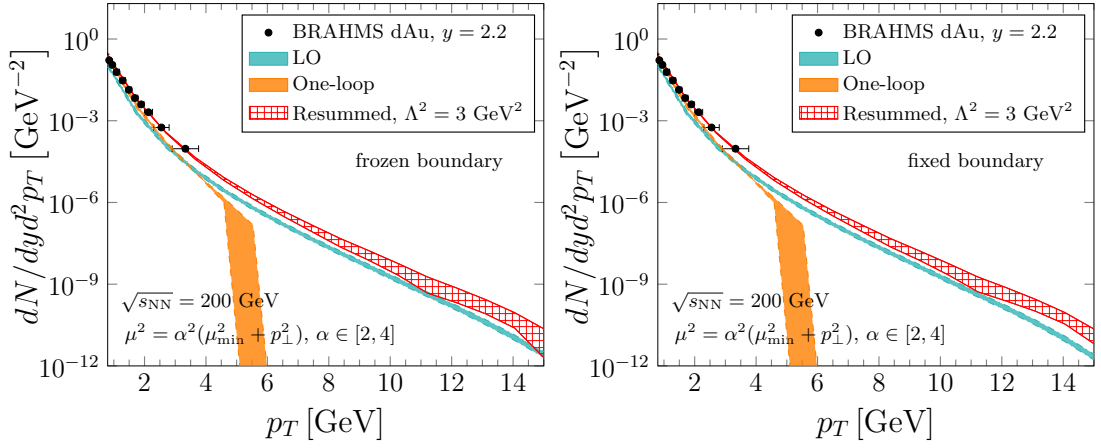


FIG. 18. Comparisons of numerical results with two different boundary conditions at $\sqrt{s_{NN}} = 200$ GeV in dAu collisions [19].

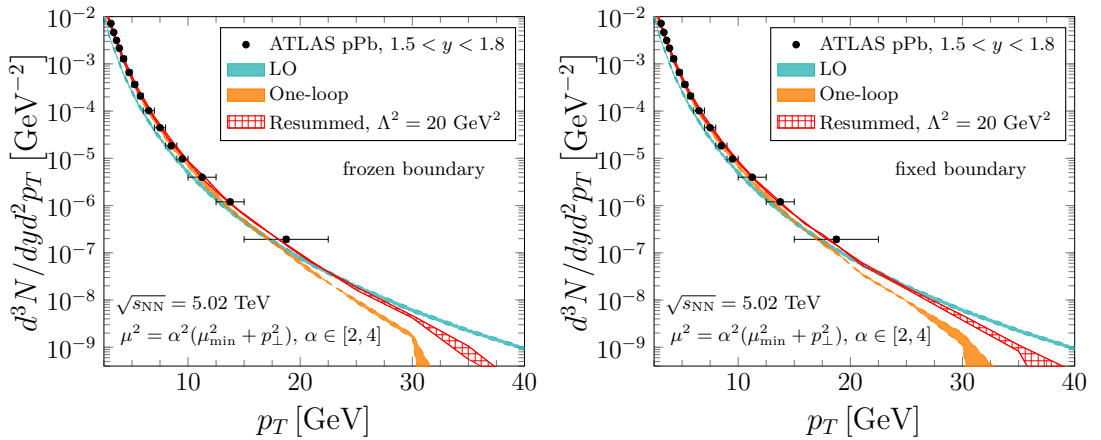


FIG. 19. Comparisons of the theoretical calculations for hadron yields with two boundary conditions at $\sqrt{s_{NN}} = 5.02$ TeV in pPb collisions[26].

at HERA has revealed an intriguing feature of geometrical scaling at $x_B \equiv Q^2/s < 0.01$ [96, 97], which has been

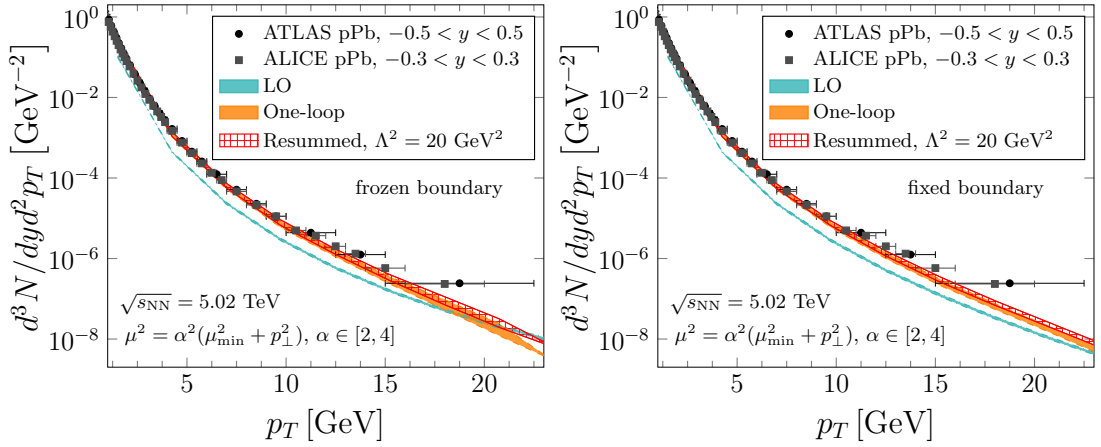


FIG. 20. Comparisons of the theoretical calculations for hadron yields with two boundary conditions at $\sqrt{s_{NN}} = 5.02$ TeV in pPb collisions[25, 26].

reckoned as a compelling evidence for saturation physics. Therefore, we often set the initial condition for the small- x dipole scattering amplitude at $x_g = 0.01$ and evolve it towards lower values of x_g .

For the forward hadron productions in pA collisions, the LO order kinematics give $x_p = \frac{k_\perp}{\sqrt{s}} e^y$ and $x_g = \frac{k_\perp}{\sqrt{s}} e^{-y}$. In our NLO calculation and scheme choice, we subtract exactly the amount of the contribution proportional to $\alpha_s \ln 1/x_g$ into the BK equation and resum this logarithm via the numerical solution of the rcBK equation. This indicates that the dipole scattering amplitude $S^{(2)}(r_\perp)$ is evolved to the same value of x_g when they are used as the small- x input in the LO and NLO cross-sections.

To apply the CGC formalism to the forward hadron production, one needs to require $x_g = x_p e^{-2y} < 0.01$ which implies $y > 1/2 \ln(100x_p)$. Since $x_p < 1$, we find that we can guarantee that x_g is always less than 0.01 for the entire k_\perp (p_T) region if $y \geq \ln 10 \simeq 2.3$. Therefore, after implementing the threshold resummation within the NLO CGC calculation, we should expect that the improved NLO calculation should be able produce satisfactory result as compared with the experimental data across the entire p_T regime for hadron produced in the rapidity $y \geq 2.3$. As we can observe from Fig.6, our resummed results describe the data measured at RHIC and the LHC well and there is no issue of negativity across the whole p_T regions.

If we wish to push the envelope and extend the CGC calculation to the rapidity region $0 < y \leq 2.3$ in pA collision, we have to deal with the fact that there is no prescription for the dipole scattering amplitude beyond the boundary when $x_g > 0.01$. To estimate the impact of the events in the large x_g region, we adopt two prescriptions as follows.

- **Fixed boundary condition:** By adopting this boundary condition, we set the k_\perp dependent gluon distribution to zero when $x_g > 0.01$ since this region is beyond the applicable window of the CGC calculation. This prescription is equivalent to removing all the events with $x_g > 0.01$ in our calculation.
- **Frozen boundary condition:** In this case, to extend the dipole gluon distribution in the large x_g region, we freeze it at $x_g = 0.01$. That is to say, when $x_g > 0.01$, the input dipole scattering amplitude simply retains its value at the initial condition at $x_g = 0.01$.

In the first prescription, by removing all the events with large x_g , we underestimate the gluon distribution in the large- x region. In comparison, with the frozen boundary condition, we overestimate the dipole gluon distribution for the region $x_g > 0.01$. The numerical difference of these two prescriptions starts to show up in the large p_T region as we see in Figs. 17-19, which can be viewed as the sign that the contribution from large x_g regions starts to become important. In the high p_T region of Fig. 20, as compared with the LHC data measured in pPb collisions by both the ATLAS and ALICE collaborations in the middle rapidity region, our results of these two prescriptions both start to deviate from the data when $p_T > 15\text{GeV}$. In this case, we believe that our NLO formalism based on the dilute-dense factorization starts to breakdown, since both the projectile and the target are now rather dilute and the collinear framework certainly becomes the more appropriate theory to describe the high p_T data. Nevertheless, we see that in the low p_T region, these two boundary conditions give consistent descriptions of the data in the low p_T region.